The Development and Applications of Terahertz Quantum Cascade Lasers

Raed Hussain S Alhathlool

Submitted in accordance with the requirements for the degree of

Doctor of Philosophy

The University of Leeds

School of Electronic and Electrical Engineering

January, 2014

The candidate confirms that the work submitted is his own, except where work which has formed part of jointly authored publications has been included. The contribution of the candidate and the other authors to this work has been explicitly indicated below. The candidate confirms that appropriate credit has been given within the thesis where reference has been made to the work of others.

The work in Chapter 4 of the thesis has appeared in publication as follows:

1. A. Valavanis, P. Dean, Y. L. Lim, R. Alhathlool, M. Nikolic, R. Kliese, S. P. Khanna, D. Indjin, S. J. Wilson, A. D. Rakic, E. H. Linfield, and A. G. Davies, Self-Mixing Interferometry With Terahertz Quantum Cascade Lasers. IEEE Sensors Journal, 13(1):pp. 37-43. 2013.
2. P. Dean, A. Valavanis, J. Keeley, K. Bertling, Y. L. Lim, R. Alhathlool, S. Chowdhury, T. Taimre, L. H. Li, D. Indjin, S. J. Wilson, A. D. Rakić, E. H. Linfield, and A. G. Davies, Coherent three-dimensional terahertz imaging through self-mixing in a quantum cascade laser. Applied Physics Letters, 103(18): pp.181112-1-181112-4. 2013.

I was responsible for fabricating the devices, samples preparation and experimental data recording. Data processing/analysis was completed in collaboration with Dr. Paul Dean and Dr. Alexander Valavanis.

The work in Chapter 2 of the thesis has appeared in publication as follows:

1. P. Dean, A. H. Awang, I. Kundu, R. Alhathlool, S. P. Khanna, L.H. Li, A. Burnett, E. H. Linfield, and A. G. Davies, Detection of terahertz frequency radiation via the photothermoelastic response of zincblende crystals. Journal of the Optical Society of America B, 30(12): pp. 3151-3160. 2013.

My role was fabricating and testing the devices used in this publication.

This copy has been supplied on the understanding that it is copyright material and that no quotation from the thesis may be published without proper acknowledgement

© 2014 The University of Leeds and Raed Hussain Saleh Alhathlool

The right of Raed Hussain Saleh Alhathlool to be identified as Author of this work has been asserted by him in accordance with the Copyright, Designs and Patents Act 1988.

Dedication

This thesis is dedicated to my parents, to my wife, Rawan, and to my son, Yazan.

Acknowledgements

I would like to acknowledge and thank my supervisors, Prof. E. H. Linfield, Prof. A. G. Davies, Prof. J. E. Cunningham and Dr. P. Dean for their support, input and guidance during my studies.

I need to acknowledge Dr. L. H. Li and Dr. S. P. Khanna for growing the wafers used in this work. Many thanks for Dr. L. Chen for his help in cleanroom related issues. Assistance in SAW measurements provided by Dr. K. Saeed was greatly appreciated. Special thanks to Dr. A. Burnett and Dr. M. Byrne for their assistance related to the terahertz lab aspects. I am particularly grateful for the cleanroom technical related issues given by Mr. G. Butterworth. I wish also to thank Miss Louise Redmonds and Mrs S. Hobson for their administrative support.

I must thank Prof. E. H. Linfield for the exceptional work of reading this thesis and offering his valuable comments. I am also indebted to Dr. A. J. Laister and Mr N. Hunter for their time spent proof reading this thesis.

My express gratitude is extended to P. Dean for his numerous help and contribution to this work and also for his guidance in the measurement aspect. To Dr. A. Valavanis, I express my gratefulness for the discussion and interpretation of many results presented in this thesis. It was through his expertise that I learned as much about THz QCLs and developed my knowledge in the terahertz field. I was fortunate knowing Alex, and my time here at Leeds would not have been as enjoyable if it wasn’t for him.

I would like also to express my appreciation to my QCLs colleagues: Dr. M. S. M. Ibrahim, Dr. M. Salih, Dr. N. K. Saat, Dr. A. Awang, Mr I. Kundu, Mr S. Chowdhury, Miss J. Zhu and Mr J. Keeley. It was great working with such a nice group of people. I am also very thankful to Dr. A. J. Laister, Dr. O. Hatem, Dr. M. U. Shaukat, Dr. N. Dodoo-Amoo, Dr. D. Mistry, Dr. C. Russell, Mr O. Aldaghri, Mr W. Muchenje, Mr N. Hunter, Mr R. Lee, Mr L. Jin and all my other colleagues and researchers past and present at the IMP.

For financial support throughout the course of my studies, I would like to acknowledge my Scholarship sponsor, Al-Imam University (Riyadh, Saudi Arabia). Thanks are due also to Royal Embassy of Saudi Arabia, Cultural Bureau in London for the Scholarship administrative support.

Here, I would like to take this opportunity to thank Prof. E. H. Linfield for the motivation and enthusiasm he provided and his unconditional support which I am sincerely grateful to and will not forget.

More personally, I would like to thank my parents for their love, endless support and encouragement. My brothers and sisters deserve my wholehearted thanks as well. I am very thankful to my little son, Yazan, for giving me happiness during the last six months of my studies. At the end, to my caring, loving, understanding and supportive wife, Rawan: my deepest gratitude.

Abstract

Terahertz frequency quantum cascade lasers (THz QCLs) are compact, semiconductor sources of coherent THz radiation, and have numerous potential applications in chemical sensing and industrial inspection, as well as security and biomedical imaging. In this thesis, the development of QCLs as sources of THz radiation is explored, together with their application in self-mixing (SM) imaging systems.

The effect of reducing the etch depth of the THz QCL active region was explored, and its influence on QCL performance evaluated. This was aimed of improving the thermal management in QCLs, as well as optimizing the structures for integration with electrical photonic components.

The reliance of THz QCLs on slow and incoherent thermal detectors has limited their practical use in THz systems. This was addressed by using a THz QCL as both the radiation source and an interferometric detector. THz sensing and imaging through SM interferometry in a QCL was demonstrated, in which radiation is reflected from an object back into the QCL cavity, causing changes in the laser properties, depending on the amplitude and phase of the reflection. This allows simple, 'detector-free', sensing of displacement and reflectivity, with high-sensitivity owing to the coherent nature of the detection. The equivalence between SM-perturbations to the THz power and the laser voltage was shown. Owing to the high SM sensitivity, high-resolution stand-off imaging at round-trip distances of up to 21 m through air was demonstrated - the longest range interferometric sensing with a THz QCL to date. Coherent three-dimensional (3D) terahertz imaging through SM in a THz QCL was also performed, in which the surface height was extracted from the phase of the SM signal.

To achieve tunable single mode THz QCL emission, which is highly beneficial for imaging and sensing applications, surface acoustic waves (SAWs) propagation across the sloped etched facets of a QCL mesa was demonstrated. The work also investigated the effect on device performance of SAW propagation over the QCL active region. This demonstration could pave the way for monolithic integration of QCLs into terahertz circuits.

Publications

Journal Publications

1. A. Valavanis, P. Dean, Y. L. Lim, R. Alhathlool, M. Nikolic, R. Kliese, S. P. Khanna, D. Indjin, S. J. Wilson, A. D. Rakic, E. H. Linfield, and A. G. Davies, Self-Mixing Interferometry With Terahertz Quantum Cascade Lasers. IEEE Sensors Journal, 13(1):pp. 37-43. 2013.
2. P. Dean, A. Valavanis, J. Keeley, K. Bertling, Y. L. Lim, R. Alhathlool, S. Chowdhury, T. Taimre, L. H. Li, D. Indjin, S. J. Wilson, A. D. Rakić, E. H. Linfield, and A. G. Davies, Coherent three-dimensional terahertz imaging through self-mixing in a quantum cascade laser. Applied Physics Letters, 103(18): pp.181112-1-181112-4. 2013.
3. P. Dean, A. H. Awang, I. Kundu, R. Alhathlool, S. P. Khanna, L.H. Li, A. Burnett, E. H. Linfield, and A. G. Davies, Detection of terahertz frequency radiation via the photothermoelastic response of zincblende crystals. Journal of the Optical Society of America B, 30(12): pp. 3151-3160. 2013.

Conference Proceedings

1. R. Alhathlool, P. Dean, A. Valavanis, Y. L. Lim, R. Kliese, M. Nikolic, S. P. Khanna, L. H. Li, D. Indjin, J. E. Cunningham, S. J. Wilson, A. D. Rakic, A.G. Davies, and E. H. Linfield, Terahertz sensing and imaging through self-mixing in a quantum cascade laser in: UK Semiconductors 2012. [Invited talk].
2. A. Valavanis, P. Dean, Y. L. Lim, R. Alhathlool, A. D. Burnett, S. Chowdhury, R. Kliese, M. Nikolic, S. P. Khanna, M. Lachab, D. Indjin, S. Wilson, A. D. Rakic, A. G. Davies, and E. H. Linfield, Detection of concealed weapons and characterisation of crystalline powders using terahertz quantum cascade lasers in: UK Semiconductors 2012. [Poster presentation].
3. A. H. Awang, P. Dean, R. Alhathlool, I. Kundu, S. P. Khanna, L. H. Li, E. H. Linfield, and A. G. Davies, Thermo-optic detection of quantum

cascade laser radiation in the range ~2.2−2.9 THz using a ZnTe crystal in: UK Semiconductors 2012. [Talk presentation].

4. P. Dean, A. Valavanis, R. Alhathlool, S. P. Khanna, D. Indjin, E. H. Linfield, A. G. Davies, Y. L. Lim, M. Nikolic, R. Kliese, S. J. Wilson, and A. D. Rakic, Self-Mixing Interferometry with Terahertz Quantum Cascade Lasers in: The 2nd International Symposium on Terahertz Nanoscience (TeraNano 2012). [Invited talk]
5. R. Alhathlool, P. Dean, A. Valavanis, Y. L. Lim, R. Kliese, M. Nikolic, S. P. Khanna, L. H. Li, D. Indjin, J. E. Cunningham, S. J. Wilson, A. D. Rakic, A. G. Davies, and E. H. Linfield, Surface-profiling through self-mixing in a THz quantum cascade laser in: International Quantum Cascade Lasers School & Workshop 2012. [Poster presentation].
6. A. H. Awang, P. Dean, R. Alhathlool, I. Kundu, S. P. Khanna, L. H. Li, E. H. Linfield, and A. G. Davies, Thermo-optic detection of quantum cascade laser radiation in the range ~2.2−2.9 THz using a ZnTe crystal in: International Quantum Cascade Lasers School & Workshop 2012. [Poster presentation].
7. P. Dean, A. H. Awang, R. Alhathlool, I. Kundu, S. P. Khanna, L. H. Li, E. H. Linfield, and A. G. Davies, Thermo-optic detection of quantum cascade laser radiation in the range ∼2.2-2.9THz using a ZnTe crystal in: The 37th International Conference on Infrared, Millimeter, and Terahertz Waves, IRMMW-THz. 2012. [Talk presentation].
8. A. Valavanis, P. Dean, Y. L. Lim, R. Alhathlool, A. D. Burnett, S. Chowdhury, R. Kliese, M. Nikolic, S. P. Khanna, M. Lachab, A. D. Rakic, A. G. Davies, and E. H. Linfield, Feedback interferometry and diffuse reflectance imaging with terahertz quantum cascade lasers in: NATO Advanced Research Workshop on Detection of Explosives and CBRN (Using Terahertz). 2012. [Invited talk]
9. Y. L. Lim, K. Bertling, P. Dean, A. Valavanis, R. Alhathlool, S. P. Khanna, D. Indjin, E. H. Linfield, A. G. Davies, S. J. Wilson, and A. D. Rakic, Self-mixing signals in terahertz lasers in: Conference on Optoelectronic and Microelectronic Materials Devices (COMMAD),pp.105-106. IEEE. 2012. [Talk presentation].

10. J. Keeley, P. Dean, R. Alhathlool, A. Valavanis, L. H. Li, E. H. Linfield, and A. G. Davies, Terahertz interferometry and imaging using self-mixing in a quantum cascade laser in: UK Semiconductors 2013. Institute of Physics. [Poster presentation].

11. P. Dean, A. H. Awang, I. Kundu, R. Alhathlool, S. P. Khanna, L. H. Li, E. H. Linfield, and A. G. Davies, Photothermoelastic response of zincblende crystals to radiation from a THz-frequency quantum cascade laser in: The 38th International Conference on Infrared, Millimeter, and Terahertz Waves, IRMMW-THz, IEEE. 2013. [Poster presentation].

12. P. Dean, T. Taimre, K. Bertling, Y. L. Lim, J. Keeley, A. Valavanis, R. Alhathlool, S. P. Khanna, M. Lachab, D. Indjin, E. H. Linfield, A. G. Davies, and A. D. Rakić, Coherent imaging and sensing using the self-mixing effect in THz quantum cascade lasers in: The 12th International Conference on Intersubband Transitions in Quantum Wells. Princeton University. 2013. [Talk presentation].

13. P. Dean, T. Taimre, K. Bertling, Y. L. Lim, J. Keeley, A. Valavanis, R. Alhathlool, S. P. Khanna, M. Lachab, D. Indjin, E. H. Linfield, A. G. Davies, S. J. Wilson, and A. D. Rakić, Coherent imaging and sensing using the self-mixing effect in terahertz quantum cascade lasers in: International Conference on THz and Mid Infrared Radiation and Applications to Cancer Detection Using Laser Imaging. 2013. [Invited talk]

14. A. D. Rakić, T. Taimre, K. Bertling, Y. L. Lim, P. Dean, J. Keeley, A. Valavanis, R. Alhathlool, S. P. Khanna, M. Lachab, D. Indjin, Z. Ikonic, P. Harrison, E. H. Linfield, and A. G. Davies, Self-mixing effect in THz quantum cascade lasers: Applications in sensing and imaging in: 2013 IEEE 4th International Conference on Photonics (ICP), pp.18-20. IEEE. 2013. [Talk presentation].

Table of contents

Dedication .... **iii**

Acknowledgements .... **iv**

Abstract .... **vi**

Publications .... **vii**

Journal Publications vii

Conference Proceedings vii

Table of contents .... **x**

List of tables .... **xiii**

List of figures .... **xiv**

Chapter 1 Introduction **1**

1.1 Terahertz frequency radiation 1

1.2 Terahertz sources 2

1.3 Inter-sub-band transition 4

1.4 Quantum cascade lasers 6

1.4.1 Theory and basic concepts 9

1.5 Terahertz Quantum Cascade Laser 12

1.5.1 THz QCL different active region designs 13

1.5.1.1 Chirped superlattice design 14

1.5.1.2 Bound-to-continuum design 15

1.5.1.3 Resonant phonon design 15

1.5.1.4 Hybrid design 15

1.5.2 Growth of THz QCL active region 16

1.5.3 THz QCL waveguides 17

1.5.3.1 Semi-insulating surface-plasmon waveguide 18

1.5.3.2 Double metal waveguide 18

1.6 Thesis overview 20

Chapter 2 Fabrication of terahertz quantum cascade laser with single-metal waveguide and characterization setup **21**

2.1 Introduction 21

2.2 Fabrication of THz QCL with single metal waveguide 22

2.2.1 Laser ridge definition 22

2.2.2Bottom ohmic contact and annealing 24
2.2.3Top ohmic contact 25
2.2.4Over-layer deposition 25
2.2.5Substrate thinning 26
2.2.6Backside metallization 27
2.2.7Cleaving facet 27
2.2.8Mounting and wiring the devices 30
2.3 Fabrication of QCLs with angled facets 31
2.4 Fabrication of interdigitated transducer 33
2.4.1Zinc oxide thin film deposition 35
2.5 Fabrication of THz QCL with IDTs 36
2.6 Experimental setup 39
2.7 Summary 43
Chapter 3 Investigation of terahertz quantum cascade laser performance with thin etched active regions 44
3.1 Introduction 44
3.2 Devices parameters 46
3.3 L559 devices characterisation 50
3.3.1L559 - 10 μm etch depth 50
3.3.2L559 - 8.5 μm etch depth 55
3.3.3L559 - 7.5 μm etch depth 57
3.3.4L559 - 6.5 μm etch depth 59
3.3.5L559 - 5 μm etch depth 60
3.3.6L559 - 4.2 μm etch depth 62
3.3.7L559 devices discussion 62
3.4 Devices characterisation for different active region 69
3.5 Conclusion 72
Chapter 4 Self-mixing technique in a terahertz quantum cascade laser 74
4.1 Introduction 74
4.2 Self-mixing theory 77
4.3 Demonstration of SM effect on the terminal voltage of a THz QCL 87
4.4 Equivalence of SM-voltage and SM-power signals 93
4.5 Long stand-off imaging and sensing 97

4.6 Surface-profiling through self-mixing in a THz QCL 100
4.7 Conclusion 104
Chapter 5 Terahertz quantum cascade lasers with surface acoustic waves 105
5.1 Introduction 105
5.2 Theory 108
5.2.1 Surface acoustic waves 108
5.2.2 Interaction of surface acoustic waves with laser active region 111
5.3 Device parameters 114
5.4 IDTs characterisation on bulk GaAs 116
5.4.1 IDTs characterisation on GaAs with different mesa height 119
5.5 IDTs characterisation on GaAs sputtered with ZnO 122
5.6 IDTs with THz QCLs 124
5.7 Conclusion 135
Chapter 6 Conclusion and Future work 137
6.1 Conclusion 137
6.2 Future work 142
List of References 146
List of Abbreviations 154
Appendix A The growth structure 156

List of tables

Table 3-1: The dimension, active region design and designed optical frequency of twenty devices used to investigate the changes to threshold current density, maximum operating temperature and peak power, all as a function of the etched active region thickness. All devices fabricated from wafers grown with a normal 10 μm active region thickness...................... 48

Table 3-2: Performance overviews of two different devices fabricated from L559 with 10 μm etch depth (fully etched). 51

Table 3-3: Performance overviews for three different devices fabricated from L559 with an 8.5 μm etch depth. 56

Table 3-4: Performance overviews for four different devices fabricated from L559 with 7.5 μm etch depth. 57

Table 3-5: Performance overview for two different devices fabricated from L559 with a 6.5 μm etch depth. 59

Table 3-6: Performance overviews for device fabricated from L559 with a 5 μm etch depth. 60

Table 3-7: Performance overview for eight devices with different etch depths from the wafers L281, L645 and L647......................... 69

Table 5-1: Summary of 24 devices fabricated to study the effect of the mesa height and doping on SAW transmission. 119

Table 5-2: Performance overview for exemplar THz QCLs devices integrated with IDTs... 125

List of figures

Figure 1-1: THz gap among the electromagnetic spectrum, figure is reproduced from [2]. 1

Figure 1-2: Schematic illustration of an interband (E_{12}) and an inter-sub-band (e_{12}) transition. 4

Figure 1-3: Active region design of the first QCL, figure is reproduced from reference [18]. 8

Figure 1-4: Photon generation through: (a) a conventional interband semiconductor laser transitions, (b) Multi Intersubband. 8

Figure 1-5: Three level system for THz QCL, figure is reproduced from reference [27] 9

Figure 1-6: Conduction band diagrams for major THz QCL active region designs, (a) CSL, (b) BTC, (c) RP and (d) hybrid/interlaced designs. Only two modules are shown of each design. The upper and lower laser levels are plotted in red and blue respectively. The injector state is labeled as (inj). The minibands are colored in a gray shaded. figure is reproduced from reference [12]. 14

Figure 1-7: A diagram shows the energy gaps of selected semiconductors materials as a function of lattice constant, from [20]. 17

Figure 1-8: Waveguide schematic diagrams for a) single metal, and b) double metal waveguides, figure is reproduced from reference [12] 19

Figure 2-1: Schematic diagrams of the fabrication steps of a single metal QCL. (a) the unprocessed wafer, (b) mesa etching, (c) AuGeNi bottom contact, (d) AuGeNi top contact, (e) Ti/Au overlayer, and finally (f) substrate thinning and back side metallisation. AR is the active region. Figure not to scale. 28

Figure 2-2: Top microscope views of a QCL at different fabrication steps. (a) mesa etching, (b) AuGeNi bottom contact, (c) bottom contact annealing, (d) AuGeNi top contact, and finally (e) Ti/Au overlayer. The mesa width in all figures is 150 µm. 29

Figure 2-3: Two photos of a copper block with two single metal QCLs after mounting and wire bonding. 30

Figure 2-4: Top microscope views of angled facet QCLs. 32

Figure 2-5: (a) Schematic diagram and (b) Scanning electron micrograph (SEM) of a THz QCL cavity formed by wet etching to provide sloped facets with angle Φ ~ 42º. Courtesy of [41]. Figure (a) not to scale. 32

Figure 2-6: (a) Two schematic diagrams and (b) two top microscope views of IDTs fabricated on a SI GaAs chip. Figure (a) not to scale. 34

Figure 2-7: Top views of a GaAs chip containing four set of IDTs, in which one of them is wire bonded to a PCB through several gold pads. 35

Figure 2-8: (a) Two schematic diagrams and (b) top microscope view of a single metal QCL monolithically integrated with IDTs. Figure (a) not to scale. 37

Figure 2-9: (a) Schematic diagram and (b) top view of two IDTs monolithically fabricated with a QCL all mounted onto a copper block and wired to two PCBs. Figure (a) not to scale. 38

Figure 2-10: Schematic diagram shows two mounted QCL devices on a copper block. Electrical connections to the laser cavities also illustrated. Figure not to scale. 41

Figure 2-11: The layout of the Experimental setup used for radiation spectrum characterisation of a QCL. For power (L-I) measurements, the FTIR was excluded and the radiation was directly fed to the bolometer. 42

Figure 3-1: Illustrative diagrams of two THz QCL with different etched thicknesses. The change in thickness was achieved through wet etching, where Ψ is the etch depth. Figure not to scale. The right diagram represents a fully etched (10 µm) device. 49

Figure 3-2: The V-J characteristics of L559 (10 µm etch depth) for 1.50 mm × 150 µm device at different temperatures. 51

Figure 3-3: The L-J characteristics of L559 (10 µm etch depth) for 1.5 mm × 150 µm device at different temperatures. The unsmooth nature of the line is due to experimental limitation. 52

Figure 3-4: Conduction band diagram of 3QW LO-phonon design [51] 53

Figure 3-5: Illustration diagrams correspond to current injection stages in a THz QCL. At (a) the parasitic conduction channel become into alignment with each other, (b) correspond to the threshold and lasing stage and at (c) the conductance of the device decreases dramatically. The LIV plots used in this figure is for illustration only. 54

Figure 3-6: The emission spectra of 3.1 THz of L559 (10 μm etch depth) for 1.5 mm × 150 μm device. The spectra were taken at 16 kV/cm and a heat-sink temperature of 10 K. The spectra are normalized relative to its maximum value for a given device 55

Figure 3-7: The V-J and L-J characteristics of L559 (8.5 μm etch depth) for 2.1 mm × 150 μm device at 4 K. 56

Figure 3-8: The V-J and L-J characteristics of L559 (7.5 μm etch depth) for 1.5 mm × 150 μm device at different temperatures. The unsmooth nature of the line is due to experimental limitation. 58

Figure 3-9: The relationship between J_{th} and duty-cycle at 4 K for the device 1.5 mm × 150 μm × 7.5 μm dimension etch depth. 58

Figure 3-10: The V-J and L-J characteristics of L559 (6.5 μm etch depth) for 1.7 mm × 150 μm device at 4 K. 60

Figure 3-11: The V-J and L-J characteristics of L559 (5 μm etch depth) for 1.55 mm × 150 μm device at different temperatures. 61

Figure 3-12: The V-J characteristics of L559 (5 μm etch depth) for 1.9 mm × 150 μm device at different duty-cycle. 61

Figure 3-13: The V-J relationship for a number of devices from wafer L559 of different cavity length from 10, 8.5, 7.5 and 5 μm etched depth. The dimension of each device (length × width × thickness) is shown in the legend. The unsmooth nature of the line is due to experimental limitation. 63

Figure 3-14: The L-J characteristics comparison of L559 (10 and 7.5 μm thick active region) at 4K and 2 % duty-cycle. The dimension of each device (length × width × thickness) is shown in the legend. 64

Figure 3-15: Schematic diagrams for two devices with different etch depth Ψ. The current path is illustrated by the red arrows. Figure not to scale 65

Figure 3-16: The relationship between J_{th} and heat sink temperature for different thick active region devises. The dimension of each device (length × width × thickness) is shown in the legend. 67

Figure 3-17: Summary three plots to illustrate the effect of changing the etch depth on (a) J_{th}, (b) P_{max} and (c) T_{max} for a number of devices from wafer L559. The length of each device is shown in the figures. 68

Figure 3-18: Comparison V-J and L-J characteristics between one 10 µm and 7.5 µm etch depth devices for the wafers (a) L281 (b) L645 and (c) L647. All measurements were taken at 4 K. The dimension of each device (length × width × thickness) is shown in the legend. 71

Figure 4-1: Three-mirror model and compound cavity model for SM effect in a single mode semiconductor laser, mirrors M_1 and M_2 form the laser cavity, the length of the cavity is L and which has an effective refractive index of μe. The external target, M_{ext}, is located on the optical axis z, at distance L_{ext}. PD is a monitor diode located in the laser package behind the laser cavity to measure power fluctuations within it. 78

Figure 4-2: Calculated waveforms of the function $\cos(\nu\tau_{ext})$ for different values of the C_{fb} parameter. (a) C_{fb} = 0.7; (b) C_{fb} = 3 and (c) C_{fb} = 10 [59]. 84

Figure 4-3: Experimental SM signal waveforms demonstrate the effect of different feedback strength on the shape of the interference signal (a) Signal driving the target; (b) SM output for C_{fb}=0.01; (c) SM output for C_{fb}=0.7; (d) SM output for C_{fb}=3.3, from [64]. 85

Figure 4-4: Root-mean-square SM signal (left axis) and QCL power (right axis) as a function of the QCL driving current. 88

Figure 4-5: The L-I and I-V characteristics of the THz QCL used in this work. Inset: the emission spectrum of the THz QCL at a drive current of 0.9 A [57]. 89

Figure 4-6: Schematic diagram of the experimental apparatus used for measuring target displacement. The QCL is driven by a constant current source and the QCL terminal voltage variations are amplified by an ac-coupled amplifier for acquisition on an oscilloscope. A parabolic mirror collimates the beam and directs it onto the remote target [53]. 91

Figure 4-7: Exemplar electrical SM signals obtained in response to a moving target (the speaker). The distance between the source and the target is of 10.5 m. 92

Figure 4-8: Schematic diagrams of the THz-SM sensor systems to study the equivalence of SM-voltage and SM-power signals. The QCL is driven by a dc current, and perturbations to the voltage are measured using an ac-coupled differential amplifier. A collimated THz beam is reflected by a plate attached to the cone of a subwoofer speaker, which is driven by a sinusoidal voltage. In this system, SM signals are also acquired using a helium cooled bolometer *D* to observe THz emission from the back facet. Ranges of obstructing materials (not shown in the diagram) were placed in the beam between the mirror and the target [53]....... 95

Figure 4-9: Comparisons between SM signals obtained by monitoring electrical and optical perturbations in response to 150 *μ*m 20 Hz speaker motion. (a) Corresponding electrical and optical SM signals (upper and lower graphs, respectively), with varying numbers *N* of PTFE attenuator sheets between the QCL and the target. (b) Decay in SM signal amplitude as a function of the number of attenuators. The solid lines in each case show regressions to an exponential decay [53]....... 96

Figure 4-10: Schematic diagrams of the THz-SM sensor systems to demonstrate long range SM sensing and imaging. The QCL is driven by dc current, and perturbations to the voltage are measured using an ac-coupled differential amplifier. The THz beam is focused onto a sample on a 2-D motorized translation stage S. A set of planar mirrors (not shown) is inserted between the two parabolic mirrors in order to extend the optical path length. The feedback is modulated using an optical chopper C and the modulation-amplitude of the SM voltage signal is acquired using a lock-in amplifier LA [53]....... 98

Figure 4-11: SM images of a scalpel blade at a range of (a) 50 cm and (b) 10.5 m between the QCL and the object. Pixel spacings of 250 *μ*m and 100 *μ*m were used, respectively. The feature at the right-hand side of the bottom image is due to reflections from the sample mount. Different blades were used for the two images. [53]....... 100

Figure 4-12: THz SM image of a PTFE cone with an angle of elevation of 4.6° ± 0.4°, showing concentric fringes arising from the slope of the cone surface [80]. 102

Figure 4-13: a) 2D and b) 3D, THz SM image of a stepped GaAs sample with 50 cm between the sample and the QCL. The top region in each image corresponds to the gold-coated region of the sample. 103

Figure 5-1: Two schematic diagrams with top microscope images showing a THz QCL integrated with SAW transducers. Figure not to scale. 107

Figure 5-2: Demonstration of the IDT operation: (a) an electrical field is applied to the transmitter IDT, (b) a SAW travels across the crystal towards the second IDT and (c) the travelling mechanical wave is collected by the receiver IDT and converted back to an electrical signal. λSAW is SAW wavelength and ν is SAW velocity [88]... 110

Figure 5-3: (a) Illustration demonstrating laser oscillation in a periodic structure. (b) Plot of the amplitudes of left traveling wave (S) and right traveling wave (R) versus distance [97]. 113

Figure 5-4: (a) Two schematic diagrams and (b) two top microscope images of IDTs fabricated on a SI-GaAs chip. Figure (a) not to scale.. 116

Figure 5-5: S parameters configurations measured by a network analyser generating SAWs at 187 MHz (a) S11, (b) S22, (c) S12 and (d) S21. 118

Figure 5-6: (a) Schematic diagram and (b) Scanning electron micrograph (SEM) of IDTs fabricated on a SI-GaAs with mesa of height (t) between the two IDTs. Φ is the mesa sloped angle. Courtesy of [41]. Figure (a) not to scale............... 120

Figure 5-7: Summary of S11 and S22 measurements of the 24 devices tested to study the effect of the mesa height and doping on the performance of SAW transmission...................... 121

Figure 5-8: Summary of S12 and S21 measurements of 24 devices tested to study the effect of the mesa height and doping on the performance of SAW transmission...................... 121

Figure 5-9: S11 and S22 parameters configurations measured by a network analyser of SAW generating at 187 MHz on 200 µm layer of ZnO.. 123

Figure 5-10: S12 and S21 parameters configurations measured by a network analyser of SAW generating at 187 MHz on 200 µm layer of ZnO.. 123

Figure 5-11: Two Schematic diagrams with top microscope images of a THz QCL monolithically integrated with two IDTs. Figure not to scale.. 126

Figure 5-12: Two Schematic diagrams with top microscope images of a THz QCL (with one facet cleaved) monolithically integrated with only one IDT. Figure not to scale. 126

Figure 5-13: S11 parameter measured by a network analyser of a SAW generated at 187 MHz from a single IDT integrated with QCL, the other IDT was removed in order to have cleaved facet for the QCL emission.......... 127

Figure 5-14: Comparison of V-J for sample L645-01 with the IDT being on (black), and off (red).......... 128

Figure 5-15: Comparison of L-J for sample L645-01 with the IDT being on (black), and off (red).......... 129

Figure 5-16: Comparison of frequency spectra for sample L645-01 with the IDT being on (black), and off (red). The QCL was drive with 16.4 V.......... 129

Figure 5-17: Comparison of frequency spectra for sample L645-01 with the IDT being on (black), and off (red). The QCL was drive with 15.4 V.......... 130

Figure 5-18: Comparison of V-J plot for the sample L645-02 with the IDT being off and on at different SAWs frequency. Each measurement was conducted twice (001 denote to the first measurement and 002 to the second measurement).......... 131

Figure 5-19: Comparison of L-J for the sample L645-02 with the IDT being off and on at different SAWs frequency. Each measurement was conducted twice (001 denote to the first measurement and 002 to the second measurement).......... 131

Figure 5-20: Comparison results of frequency spectra for the sample L645-02 with the IDT being off and on at different SAWs frequency. The QCL was run at I_{th} = 2.28 A. Each measurement was conducted twice (001 denote to the first measurement and 002 to the second measurement).......... 132

Figure 5-21: Change in output power of a THz QCL (L645-02) as the SAW frequency is changed between 205 MHz to 245 MHz. QCL was run at four different current in each measurements.......... 133

Chapter 1

Introduction

1.1 Terahertz frequency radiation

Terahertz (THz) frequency, also known as “T-rays”, is a part of the electromagnetic spectrum and is defined to lie between 300 GHz and 10 THz, corresponding to a wavelength range between 30-1000 μm and energy range of 1.25 – 37.5 meV. It fills in between the microwave and the infrared portions of the electromagnetic spectrum (Figure 1-1) [1, 2].

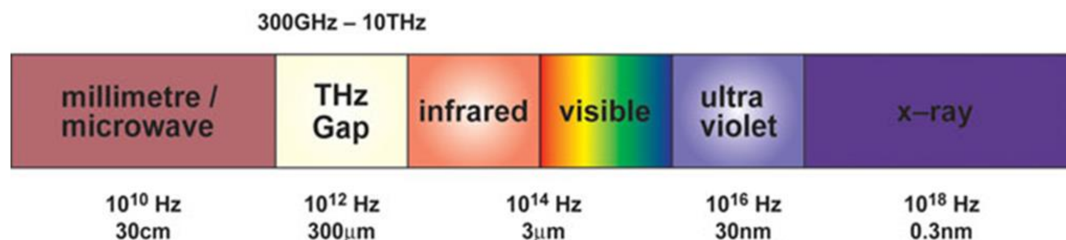

Figure 1-1: THz gap among the electromagnetic spectrum, figure is reproduced from [2].

There are a number of advantages of the THz waves that make it important. To name some, THz frequency is low in energy, which means that it has a non-ionizing behaviour [3]. This Property allows THz radiation to be used safely in biological tissues screening [4]. Also, THz radiation has

the ability to penetrate into many opaque materials, thus making it adequate for imaging in pharmaceutical applications and security screening [3, 5]. Additionally, many materials have their excitations at the THz range, which can be detected by THz probing, thereby giving a “THz finger-print” for such materials [6]. Furthermore, THz radiation has strong interaction with water [7, 8].

Owing to the advantages above, there are great numbers of applications that THz radiation can offer including but not limited to: three dimensional and real time THz imaging [9, 10], spectroscopy of explosive and drugs [11], astronomy, biological and medical imaging sciences, security screening and illicit material detection, communications technology [12, 13] and as local oscillators in heterodyne receivers [14].

1.2 Terahertz sources

Despite the scientific importance of THz spectral range, it has been undeveloped comparing to the bordering microwave and infrared spectral ranges (see Figure 1-1) [15]. This is mainly due to the absence of compact and coherent sources and detectors in this range making an “electronic – photonic gap” or “THz gap”. Recently, the interest in the terahertz spectral range has become significant as a result of the invention of new optoelectronic sources in this range.

There are number of obstructions against generating and detecting THz frequency efficiently using either of electronic and photonic technologies. First, according to Planck‘s radiation law, and over THz

range, no more than a few nano-Watts of power are produced by a thermal blackbody source at room temperature [16]. Also, electronic generation (through the use of Gunn diodes, for example) is restricted by the carrier transit times and a limitation in output power, which rolls off at only few hundred GHz [12]. In addition, owing to the small energy level separations in the THz frequency range, population inversion becomes difficult to achieve for lasers emitting in this domain.

In spite of the obstructions aforementioned, there are few THz sources realised and used by research establishments and industrial applications. Though, they are often limited by their size and cost, consume high power both electric and magnetic, and require a cryogenic cooling environment, therefore limiting their usage [12]. Examples of these sources include, but are not limited to; gas laser (such as pumped methanol lasers), narrow band p-Ge lasers, free electron lasers (FELs) [12], Gunn diode and Schottky diode multipliers [2, 12]. Optical methods can also be implemented in generating THz rays. This can be achieved either by photo-mixing for narrow band THz radiation [17], or by femtosecond optical laser for broad band THz radiation [6]. However, these two sources output low power THz waves (on the order of a few µW) owing to the inefficiency in the optical conversion and the limited speed of the photoconductive element.

In 1994, a novel THz source emerged, called the quantum cascade laser (QCL) [18]. A QCL is a compact, solid-state semiconductor device. QCLs cover the frequency from mid-infrared [18] to the THz region [19].

1.3 Inter-sub-band transition

Traditional semiconductor lasers depend on the principle of the transition between the conduction and valence energy bands, thus one can call them interband lasers. The band gap of the active region of the semiconductor material determines the emission wavelength, resulting from the radiative recombination between electrons (in the conduction band) and holes (in the valence band). Due to the absence of a natural material of less than 40 meV band gap, it is difficult to have a far-infrared (THz) conventional semiconductor laser with the existing material. To solve this problem, artificial layers of materials are used whereby the radiative emission occurs in the conduction band (Intersubband). In this case, which is illustrated in Figure 1-2, the transition take place between the quantized states (subbands) in a heterostructure quantum well [20].

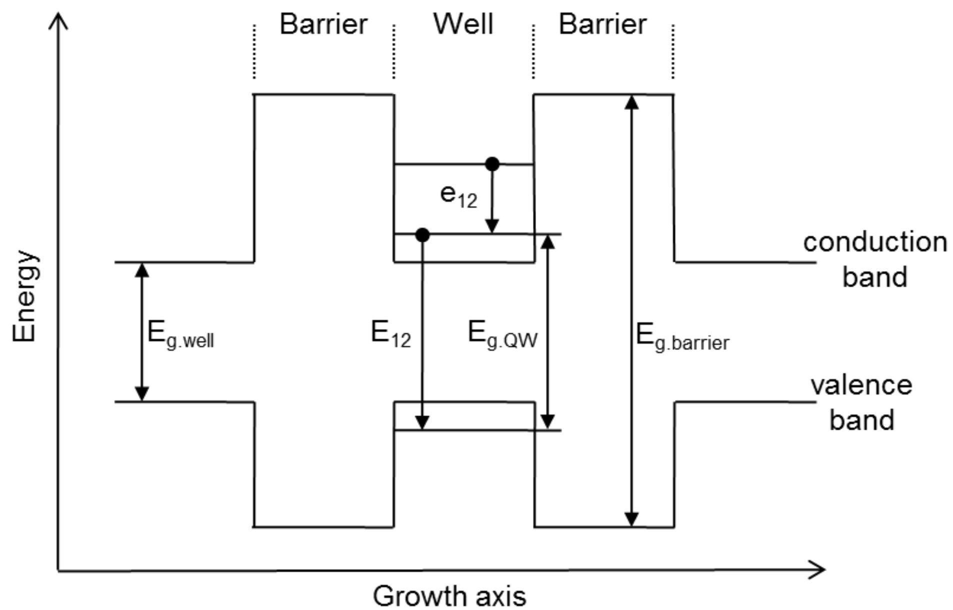

Figure 1-2: Schematic illustration of an interband (E_{12}) and an inter-sub-band (e_{12}) transition.

A heterostructure quantum well is formed by placing a semiconductor layer with a low band gap energy (GaAs, for example) between two semiconductor layers with larger band gap energy (AlGaAs, for example). Owing to the discontinuities of the band edges, caused by the unequal band gap, two phenomena occur. The first is the quantum confinement in the growth direction for the carrier (in this case, electrons). The second is the quantisation of conduction band energy into sub-bands. Therefore, the emission wavelength can be tailored by changing the layer thicknesses [20]. The sub-band energy levels can be obtained from the time-independent Schrödinger equation in the growth direction (z):

$$-\frac{\hbar^2}{2m_e^*}\frac{\partial^2}{\partial z^2}\psi_i(z) + U(z)\psi_i(z) = E_i\psi_i(z), \tag{1-1}$$

where $\hbar^2$ is the reduced Planck‘s constant, m_e^* is the electron effective mass in GaAs, E_i is the energy of the i_{th} bound state, ψ_i is the corresponding wave function, and U is the confinement potential defined by the applied bias and the band structure [20, 21].

In the situation of an infinitely deep well with a width L, the solution of equation (1-1) gives the energy for the particle as:

$$E_n = \frac{\hbar^2}{2m_e^*}\left(\frac{n\pi}{L}\right)^2, n = 1,2,3\, ... \tag{1-2}$$

Therefore, as the width of the well is increased, the allowed number or energies decrease.

Because the well is not infinitely deep, the energy levels are lower than the case with an infinite well, only a finite number of bound states will

be allowed and the electron penetrates into the barrier. In this case, equation (1-1) solution is given by the function [20]:

$$\sin(k_2 L) = 2\sqrt{\frac{E}{U_\circ} - \left(\frac{E}{U_\circ}\right)^2}, \tag{1-3}$$

where $U_\circ$ is the potential barrier height. The term k_2 is given by the equation:

$$(U - E_\circ) = \frac{\hbar^2}{2m} {k_2}^2, \tag{1-4}$$

To create multi- quantum wells (MQW), a series of quantum wells can be grown, separated by barriers. The electrons remain confined inside the wells until the width of the barriers become thin so the electron can penetrate it [22]. Then, mini-bands are created duo to the broadening of the sub-bands and the whole structure, thus, called superlattices.

1.4 Quantum cascade lasers

The basic principle of quantum cascade lasers (QCLs) was initially proposed in 1971 by Rudolf Kazarinov and Robert Suris [23]. But it wasn't until 1994 when the first working QCL was demonstrated by J. Faist (Capasso team) at Bell Research Laboratories [18]. The First QCL emitted in the Mid Infra-Red (MIR) (~ 4.2 μm) at cryogenic temperatures in pulse operation with a few milli-Watts peak power. The active region design consisted of a 3-well undoped active region separated by a superlattice (long chain of coupled quantum wells) graded alloy (see Figure 1-3). The MQW heterostructure used GaInAs/AlInAs materials [18]. Since then, many

improvements have been made to MIR QCLs in term of operating temperature, emitted power, and tuneability [24]. The first QCL operated at room temperature emitted at (8.5 μm) and was reported by Sirtori in 1997 [25].

QCLs are unipolar semiconductor lasers and are based on intersubband transitions, made by electrons, in a MQW heterostructure where the upper and lower laser levels are located in the conduction band (Figure 1-4 b). Thanks to the resonant tunnelling method, one of the advantages of a QCL is that several photons are emitted per single electron injected to the upper laser level in a series of quantum wells in the active region, hence the term “Cascade”, which gives high power performance of the laser (Figure 1-4 b). In contrast to conventional semiconductor lasers, where the wavelength depends on the bandgap of the adopted material (Figure 1-4 a), QCL’s wavelength can be tailored by changing the thickness of the QWs [26, 27].

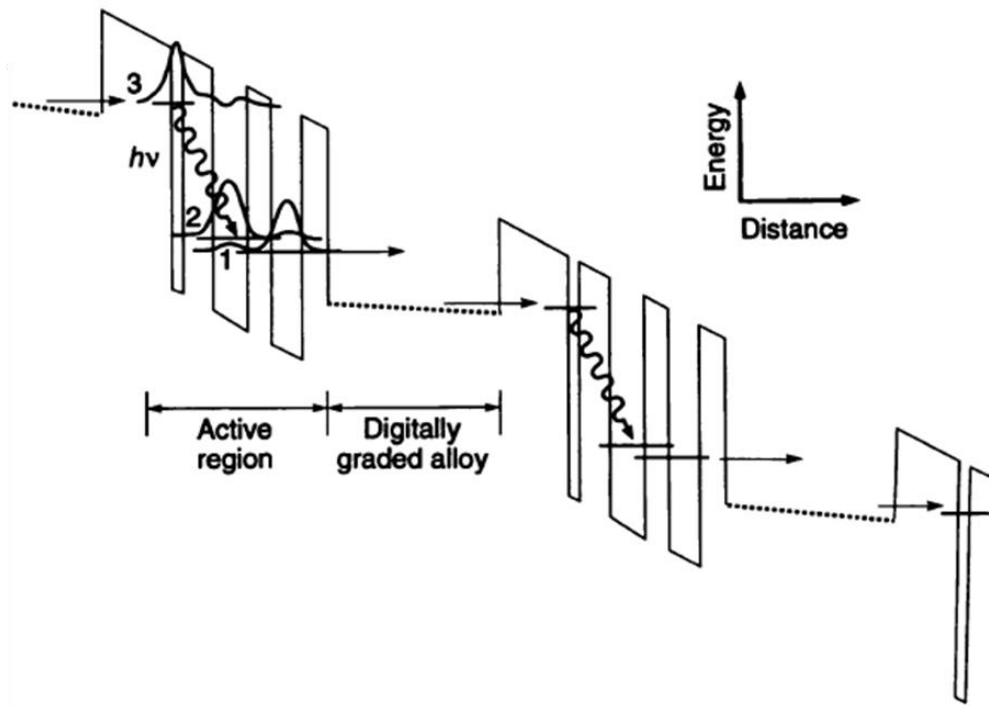

Figure 1-3: Active region design of the first QCL, figure is reproduced from reference [18].

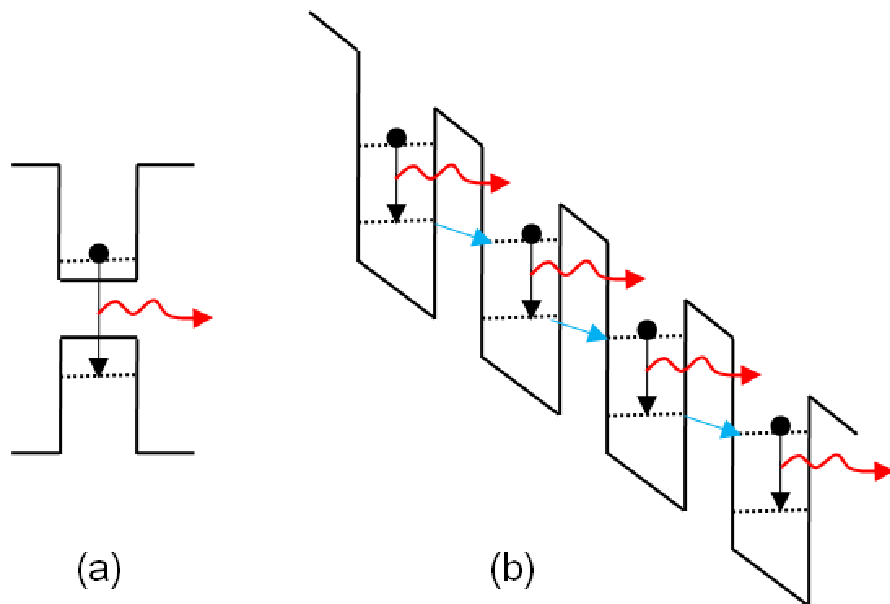

Figure 1-4: Photon generation through: (a) a conventional interband semiconductor laser transitions, (b) Multi Intersubband.

1.4.1 Theory and basic concepts

THz QCL mechanism can be described in a simple way using a three level system (see Figure 1-5).

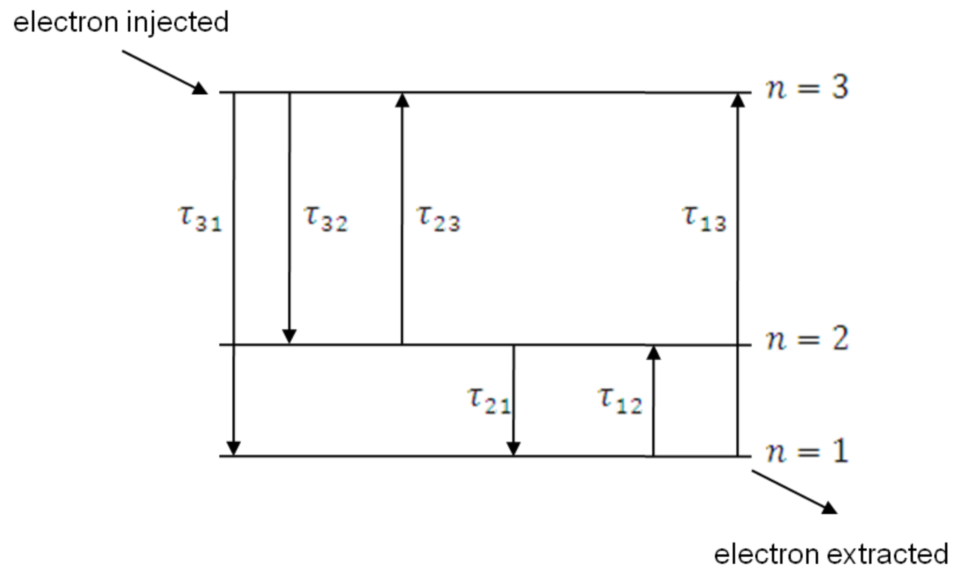

Figure 1-5: Three level system for THz QCL, figure is reproduced from reference [27] .

In this system the electrons are injected to level “3” (the upper laser) then transmit between the three levels until they are extracted from level “1” (lower laser level) emitting their photon between these levels [27].

The rate equations that describe the electrons scattering between these levels are as follows:

$$\frac{dn_3}{dt} = \frac{J_{in}}{e} + \frac{n_1}{\tau_{13}} + \frac{n_2}{\tau_{23}} - \frac{n_3}{\tau_{31}} - \frac{n_3}{\tau_{32}}, \tag{1-5}$$

$$\frac{dn_2}{dt} = \frac{n_3}{\tau_{32}} + \frac{n_1}{\tau_{12}} - \frac{n_2}{\tau_{21}} - \frac{n_2}{\tau_{23}}, \tag{1-6}$$

$$\frac{dn_1}{dt} = \frac{n_2}{\tau_{21}} + \frac{n_3}{\tau_{31}} - \frac{n_1}{\tau_{13}} - \frac{n_1}{\tau_{12}} - \frac{J_{out}}{e}, \tag{1-7}$$

where n_i is the electron population in a level (i), τ_{ij} is the transition life time between two level (i and j), J is the current density, and e is the charge of an electron. In order to obtain lasing, it is important to have a population inversion between level 3 and level 2 (see Figure 1-5). Equation (1-6) can be re-written as follows considering that the system is equilibrium, and also neglecting any absorption may happen to the electrons:

$$\frac{n_3}{\tau_{32}} = \frac{n_2}{\tau_{21}}, \tag{1-8}$$

A population inversion will only occur if $\tau_{32} > \tau_{21}$ and then $n_3 > n_2$. This means that the scattering rate (W) between level 3 and level 2 should be lower than the scattering rate between level 2 and level 1, i.e. $W_{32} < W_{21}$.

To obtain lasing, there should be a gain in the active region. Equation (1-9) defines the gain coefficient (g) for a QCL [26].

$$g = \tau_3 \left(1 - \frac{\tau_2}{\tau_{32}}\right) \left[\frac{4\pi \mathrm{e} (z_{32})^2}{\epsilon_\circ n_{eff} L_p \lambda_\circ}\right] \frac{1}{2\gamma_{32}}, \tag{1-9}$$

where $\lambda_\circ$ is the wavelength in a vacuum, $\epsilon_\circ$ is the vacuum dielectric constant, $\mathrm{L_p}$ is the period length (thickness) of the active region and injector, $\mathrm{n_{eff}}$ is the effective refractive index of the mode, $2\gamma_{32}$ is the value

of the full width at half maximum (FWHM) of the luminescence spectrum, and z_{32} is the optical dipole matrix element. From equation (1-9), it is clear that the gain coefficient is proportional to frequency and inverse proportional to period length. From [27] the module gain is defined as “the fraction of the optical field that overlap the gain medium” and is given by:

$$G_M(J) = g\Gamma J, \tag{1-10}$$

where Γ is the confinement factor.

The current density where the gain and loss in the laser are equal is called “threshold current density”. There are two sources of losses in a QCL which are waveguide loss (α_w) and mirror loss (α_m) [28].

The waveguide loss comes from two sources. The first one is from the active region (α_{act}) and the second one is from the cladding materials (α_{clad}) which is either the metal or the doped semiconductor contact layers. The common loss that comes from both of the previous losses is free carrier loss (α_{fc}). This loss is defined as follows [28]:

$$\alpha_{fc} = \frac{N_d q^3 \sqrt{\epsilon} \lambda_\circ^2}{4\pi c^3 m^2 \epsilon_\circ \mu}, \tag{1-11}$$

where N_d is the doping density, q is the transfer matrix elements, ϵ is the permittivity of the medium, c is the speed of light in vacuum, m is the electron mass, and μ is the permeability of the medium. Equation (1-11) shows the reason behind the difficulties of designing a QCL with such a long wavelength (low frequency) as the free carrier loss becomes proportional to the square of the wavelength.

The mirror loss is given by [27]:

$$\alpha_m = \frac{1}{L}\ln(R)\,, \tag{1-12}$$

where L is the length of the laser cavity, and R the facet reflectivity. To obtain lasing, the gain should be equal to or greater than to the losses, i.e. $G_M = \alpha_m + \alpha_w$. So threshold current density (J_{th}) can be written as [26]:

$$J_{th} = \frac{\alpha_m + \alpha_w}{g\Gamma}\,, \tag{1-13}$$

After the calculation of the laser threshold current density, the slope efficiency $(\frac{\partial P}{\partial I})$, which is defined from [26] as "the increase in optical power (P) per out coupling facet per unit current (I)", can be given as [26]:

$$\frac{\partial P}{\partial I} = \frac{1}{2}\frac{h\nu}{e}N_p\frac{\alpha_m}{\alpha_m + \alpha_w}\left(1 - \frac{\tau_2}{\tau_{32}}\right), \tag{1-14}$$

where $h\nu$ is the photon energy and N_p the number of active region periods.

1.5 Terahertz Quantum Cascade Laser

Two main issues made extending the wavelength of QCLs towards the THz range difficult. The first issue is the challenge in obtaining population inversion between two close levels (4-40 meV) in the quantum wells. This problem also increases the difficulty of engineering the suppression of thermal backfilling [2]. Secondly, the lack of proper mode confinement with low free-carrier absorption losses at such long wavelength [12]. Despite these two difficulties, and also the difficulty of making a laser between such two sub-band levels with an energy gap

smaller than the Longitudinal Optical (LO) Phonon ($E_{LO} \approx 36$ meV in GaAs), the first THz QCL at 4.4 THz was demonstrated in 2002 [19]. This laser was based on a chirped superlattice active region design and a surface plasmon waveguide. Since this breakthrough, many developments have occurred in both the active region and waveguide design. A brief description of typical THz QCLs designs and waveguides will be given in Sections 1.5.1 and 1.5.3 respectively.

Although the first MIR QCL was based on GaInAs/AlInAs, the materials that were adopted for the active region of THz QCLs were mostly GaAs/AlGaAs. The first MIR QCL which adopted GaAs/AlGaAs in the active region was in 1998 and it emitted a wavelength of ~ 9.4 μm [29].

1.5.1 THz QCL different active region designs

Four main active region designs have been used for THz QCLs. These designs are chirped superlattice (CSL) [19, 30, 31], bound-to-continuum (BTC) [32, 33], resonant LO phonon (RP) [34], and hybrid/interlaced active region design [12]. A schematic diagram of the different active region design can be seen in Figure 1-6.

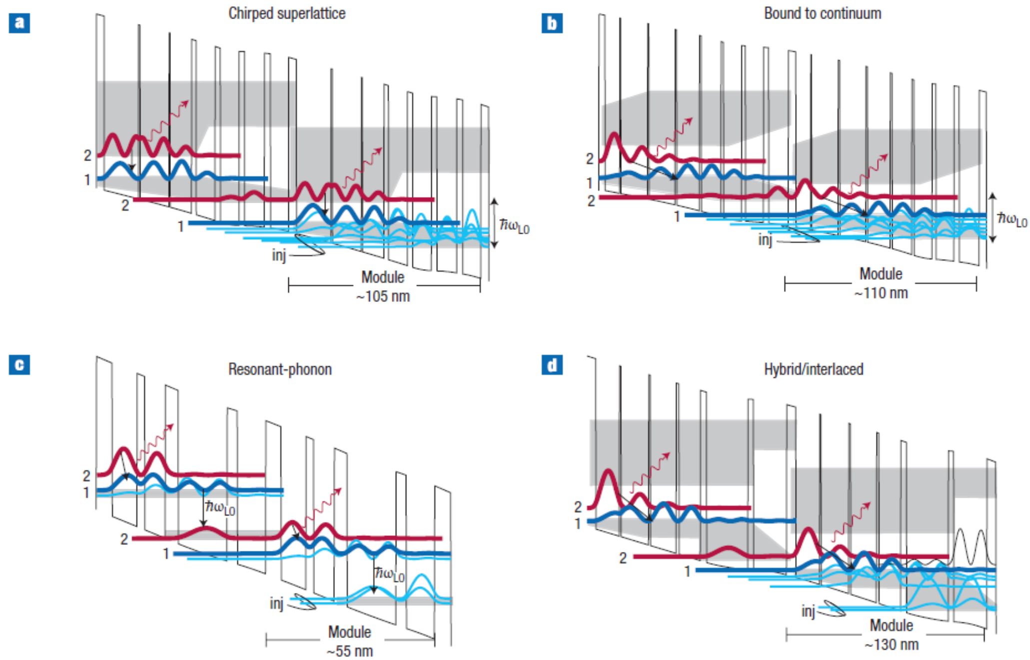

Figure 1-6: Conduction band diagrams for major THz QCL active region designs, (a) CSL, (b) BTC, (c) RP and (d) hybrid/interlaced designs. Only two modules are shown of each design. The upper and lower laser levels are plotted in red and blue respectively. The injector state is labeled as (inj). The minibands are colored in a gray shaded. figure is reproduced from reference [12].

1.5.1.1 Chirped superlattice design

The CSL active region design was the first THz QCL demonstrated [19]. This design based on coupling several quantum wells together in a superlattice structure in a way that minibands of states are created when an appropriate electric field is applied (see Figure 1-6 a) [12, 28]. Unlike the traditional interband transition, the lasing transition occurs between the lowest state of the upper miniband and the top state of the lower miniband. To maintain the population inversion in this design the lowest lasing state is depopulated by a combination of three type of scattering. These are: electron-electron, electron-impurity and interface roughness scatterings [20].

1.5.1.2 Bound-to-continuum design

The BTC active region design (see Figure 1-6 b) adopts the same principle of the chirped superlattice design in regards to the lower “continuum” radiative state the depopulation mechanism. Though, the upper lasing state is made to be a “bound” state in the mini-gap between the upper minibands and the lower minibands. The bound state is created by introducing a thin well adjacent to the injection barrier. This mechanism allows a more diagonal radiative transition in real space compared to a chirped superlattice [12, 32, 33].

1.5.1.3 Resonant phonon design

The RP active region design exploits fast LO-phonon scattering to depopulate the lower lasing level (see Figure 1-6 c). In this design, the collector and injector states are engineered to be below the lower laser level by approximately the LO-phonon energy (E_{LO} ~ 36 meV in GaAs). Thus, the electrons in the lower lasing level will scatter rapidly into the injector state by emitting an LO-phonon [12, 34].

1.5.1.4 Hybrid design

In a hybrid/interlaced active region design (see Figure 1-6 d), the optical transition and depopulation mechanisms are both adopted from BTC and RP designs respectively. The term “interlaced” comes from the alternating photon- and phonon-emission events [12].

1.5.2 Growth of THz QCL active region

The GaAs/AlGaAs material system, used for all the THz QCLs discussed in this thesis, is technologically mature. In addition, GaAs and AlGaAs match each other in term of their crystal structure. This agreement in the lattice constants is important to avoid inducing strain, defects, or dislocations in the structure (Figure 1-7) [20, 29]. However, even with such a mature material system and technology, the growth of THz QCL is challenging due to the precise calibration required for the growth rates for such a material which often exceeds thicknesses of 10 μm and typically contains over than 1000 layers. The specifications of growing THz QCLs can be met by utilizing a molecular beam epitaxy (MBE) system. In MBE, a thin film of a single crystal material (monocrystalline) is deposited onto a similar monocrystalline substrate (for example, semi- insulating GaAs substrates). This process take place under ultra-high vacuum conditions [20].

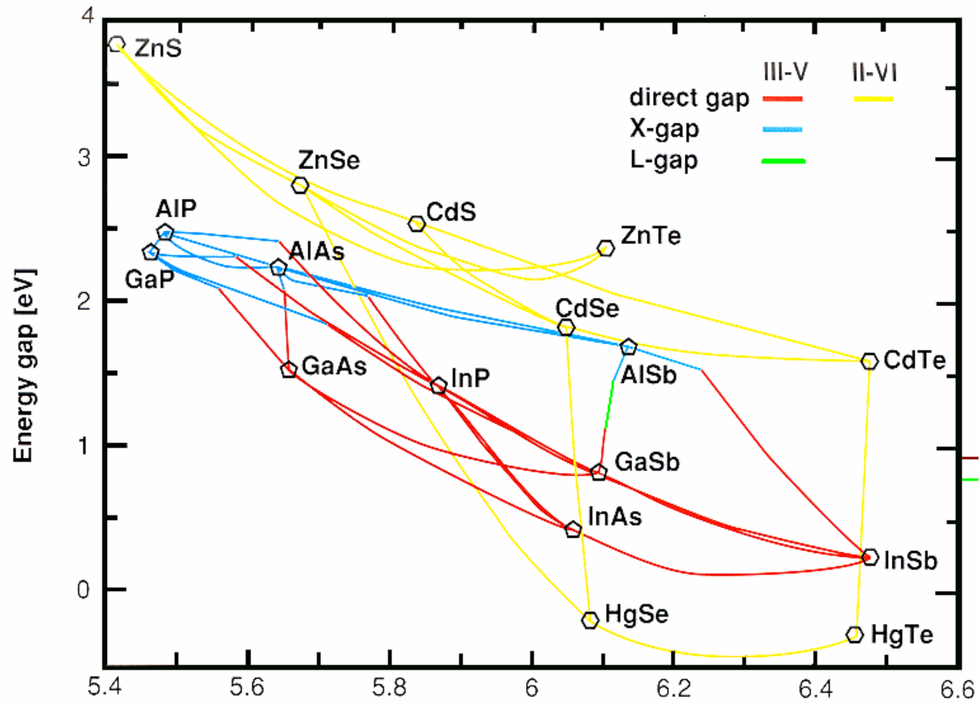

Figure 1-7: A diagram shows the energy gaps of selected semiconductors materials as a function of lattice constant, from [20].

1.5.3 THz QCL waveguides

Designing and fabricating an efficient waveguide for THz radiation is challenging for two main reasons. First, optical confinement of such long wavelengths (with an optical mode extending to several tens of micro-meters) is challenging. For mode confinement of THz QCL, it is not practical (from a growth perspective) to utilize the traditional dielectric waveguides used for MIR-QCLs as this approach requires a thick cladding layer. Secondly, the increase of the optical losses resulted from the free carrier absorption (electrons in this case), which scale with λ^2. Thus, the plasmon confinement, also used in MIR QCLs, is not suitable in THz frequency as the modal overlap with the doped GaAs regions must be in a minimum. Additionally to the main issues stated above, an ideal THz QCL

waveguide should also take into consider design schemes to maintain maximum optical confinement, good heat management, and optimised biasing [12, 20, 35]. For the optical confinement purposes, and to overcome the above challenges, two waveguide techniques have been implemented, which will be described in Sections 1.5.3.1 and 1.5.3.2.

1.5.3.1 Semi-insulating surface-plasmon waveguide

For a semi-insulating surface-plasmon (SISP) waveguide, (see Figure 1-8 a) the active region is sandwiched between a metallic layer (Ti/Au, for example) from the top and heavily doped n^+ GaAs layer (~ 800 nm) from the bottom. Thus, this waveguide also called single metal waveguide. The lower n^+ GaAs layer which grown directly above the Semi-insulating GaAs (SI-GaAs) substrate also serves as a bottom contact for electrical biasing. This layer only provides partial confinement to the optical mode, so the mode overlaps the active region down to the substrate. The thickness of this layer needs to maintain both the maximal optical confinement and minimal waveguide losses. The THz mode confinement (Γ) for this waveguide design is typically between 15 – 50 % (see Figure 1-8 a), dependent on the laser frequency [36, 37].

1.5.3.2 Double metal waveguide

As the wavelength is further increased (λ > 100 μm) the optical confinement is further reduced. In a SI-SP waveguide, where the optical modes overlap with the substrate, this phenomena causes inadequate lasing gain as a result of the reduction in the optical mode present in the gain medium [38]. Also, when the frequency approaches the plasma

frequency (ω_p), the dielectric constant of the active region decreases (as compared to the SI-GaAs substrate). This in turn further reduces the optical confinement [38]. These problems are addressed by using a double-metal waveguide [38, 39]. As seen in Figure 1-8 b, the optical mode is confined between top and bottom metallic layers. Thus, the optical mode is very well confined into the gain medium between the two metallic contacts [12]. The mode confinement (Γ) for double metal waveguide is generally 100 % with low losses (see Figure 1-8 b) [39].

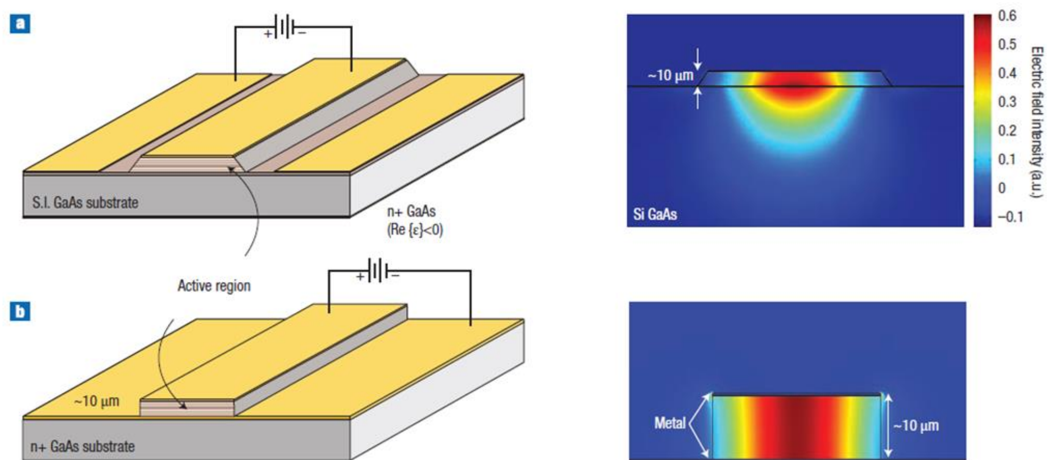

Figure 1-8: Waveguide schematic diagrams for a) single metal, and b) double metal waveguides, figure is reproduced from reference [12].

1.6 Thesis overview

Following the brief overview of THz and QCL related technology and basic theory presented, Chapter 2 specifically reviews the experimental methods for fabricating a single metal THz QCL. Additionally, a processing guide is presented for fabricating interdigitated transducers (IDTs) for the purposes of generating surface acoustic waves (SAWs). The integration between THz and IDTs will also be described in this chapter for frequency tuning purposes. It also describes the electrical and spectral characterisation procedures of THz QCL devices and IDTs measurements to obtain Scattering parameters (S-parameters) that quantify the propagation of SAWs energy. Chapter 3 discusses the study and results for a number of samples that were fabricated with a range of etched thicknesses active region. It compares the effect of varying the etched thickness of the active region on the electrical and output power performance of the lasers. Chapter 4 demonstrates the methods and the results of THz sensing and imaging through self-mixing (SM) techniques in a THz QCL and goes on to present the THz 3D imaging results for semiconductor samples. Chapter 5 reports the results of a project to study the possible utilisation of SAWs in controlling the spectral behaviour of THz QCL sources. Finally, the thesis concludes with Chapter 6, summarizing the results of the work presented together with listing possible research directions for future work.

Chapter 2

Fabrication of terahertz quantum cascade laser with single-metal waveguide and characterization setup

2.1 Introduction

In this chapter the fabrication steps to realise semi-insulating surface plasmon (SISP) terahertz quantum cascade laser (THz QCL) devices are described. The electrical and optical testing techniques used to characterise the devices are explained.

2.2 Fabrication of THz QCL with single metal waveguide

Processing was undertaken using the nanotechnology cleanroom facilities in the School of Electronic and Electrical Engineering at The University of Leeds.

In this PhD project, all the GaAs wafers containing THz QCL active regions were grown in-house by Dr. L. H. Li and Dr. S. P. Khanna utilising the molecular beam epitaxy (MBE) laboratory. The active regions of the QCL devices used in this project were designed by both the 3-Quantum-Well resonant LO-phonon (RP) and bound-to-continuum (BTC). The active regions used have differing thicknesses and ridge widths. The multi-step processing procedure is described in the following subsections.

2.2.1 Laser ridge definition

A wafer piece with an area (6×8) mm^2 was cleaved using a scalpel blade to the appropriate size to be compatible with the available photolithography mask. This chip can make use of three strip cavities with a length of 6 mm each.

In order to remove contamination from the sample, it was immersed in an acetone-based ultrasonic bath with a moderate power (~10% agitation) for two minutes. The sample is then rinsed using isopropyl alcohol (IPA) followed by an immediately applying a dry N_2 gas stream to avoid creating staining on the material surface. For further cleaning, the

sample was either subjected to an oxygen plasma asher (Emitech K1050X Plasma Asher, cleaned using a power of 85 mW for 5 minutes) or, otherwise, the sample can be dried by heating on hot plate at 200°C for 2 minutes to remove any possible residual solvent. Apart from the ultra-sonic agitation, this was the routine cleaning procedure for the each sample prior to the start of each lithography step.

The clean sample is coated with positive photo resist (Shipley S1813) and spun for 30 seconds at 5000 rpm which yields a photoresist a thickness of ~ 1.2 µm. Following the spinning, the sample is soft backed on hot plate at 115°C to harden the photoresist layer. Prior to mesa etching, to define the ridge, the sample was exposed to ultraviolet (UV) light at 4 mW cm^{-2} for 7 seconds using masks with different ridge widths. The resist was developed in MF319 for 75 seconds and rinsed in deionised (DI) water then dried by blowing with dry N_2 gas gun. The developed sample is hard baked at 90°C for one minute. To facilitate handling during etching process, the sample is mounted on a glass slide by using a thin layer of photoresist (to act as glue) on the glass slide. The sample was placed facing up on the slide, then baked on hot plate at 115°C for 1 minute. Ridges are etched into different heights using a sulphuric acid solution (H_2SO_4:H_2O_2:H_2O) in a ratio of 1:8:40 volume respectively [40] which etches at a rate of 1 µm per minute. Following the mixing of the solution, it was left for 20 minutes to stabilise the temperature before doing the etching as the solution has an exothermic reaction when mixed. The sample was agitated in a figure of ‘8’ motion to enhance even surfacing etching. Extra care was taken to only etch the active region and not etch further the bottom layer of n-GaAs by

using a surface profiler (KLA Tencor Alpha-Step IQ) to measure the exact etching rate and thickness to avoid any over and under etching (see Figure 2-1 a and b and also Figure 2-2 a).

After the etching, the sample is rinsed with DI water and dried with dry N_2 gas and removed from the glass slide using acetone, followed by IPA. The sample is then further cleaned with acetone, IPA and plasma asher at 85 W for 5 minutes to remove any residual photoresist.

2.2.2 Bottom ohmic contact and annealing

After defining the ridge the bottom contact was subsequently formed by typical photolithography processing steps (see Figure 2-1 c and Figure 2-2. b) The undergoes another photolithography processing cycle implemented above, where it was cleaned with acetone, IPA, dried by blowing with dry N_2 gas and then placed in plasma asher using a power of 85 mW for 5 minutes. The sample then was spun with photoresist, after that baked at 90°C, and exposured to UV light. The resist was then cured with Chlorobenzene for 2 minutes to form the under-cut profile which facilitates the lift-off step. Finally the sample was developed for 90 seconds. Prior to bottom contact metallisation the sample is placed in a plasma asher at 25 W for 70 seconds to remove any possible traces of organic residue left on the surface. A layer of AuGeNi bottom contact is deposited using a Turbo Pumped Thermal Evaporator (Leybold system UNIVEX 300) under a vacuum of 2×10^{-6} mBar using 0.6 g of material which gives a thickness of ~ 150 nm. The evaporation process is started at a very low rate (e.g. 0.1 Å/second) to ensure that a very smooth surface of metal is

deposited. The sample was then left in acetone for a few hours to assist the lift-off processing. In cases where traces of unwanted metal are present, the sample can be agitated by using a brush or pipette in a shallow beaker of acetone. The ultrasonic bath is avoided as it risks damaging the sample. Figure 2-2 (b) shows a microscope view after this step. Following the standard cleaning steps mention above, the sample is then annealed using a rapid thermal annealer (RTA) (AnnealSys AS-One 100) at 430°C for one minute to enhance the diffusion of the metal into the bottom n^+ GaAs layer, thus to provide n^{++} GaAs and make an ohmic contact. The bottom contact is then tested by ohmmeter, checking that the resistivity measured is ~ 10-20 Ω to ensure a good level of metal diffusion (see Figure 2-2 c).

2.2.3 Top ohmic contact

A third photolithography processing cycle is applied on the sample to form the two narrow strip top contacts (see Figure 2-1 d and Figure 2-2 d). The processing steps are the same as the previous photolithography processing steps used in the fabrication of the bottom contact, except that the applied AuGeNi metallisation thickness is reduced to 100 nm to avoid optical absorption losses in this layer. The other notable difference is that instead of the bottom contact annealing mentioned above, the sample is sintered at 270°C for 4 minutes to provide a shallow diffusion depth which is just enough to realise an ohmic contact (see Figure 2-2 d).

2.2.4 Over-layer deposition

On surfaces deposited with AuGeNi, a poor morphology caused by annealing is observed. This problem creates rough surfaces which can

negatively affect the forthcoming wire ball bonding to the device. To overcome this issue, and also to provide an optical confinement on the top of the active region, gold over-layers are deposited.

Following top contact processing, a photolithography processing cycle was applied again to create the Ti/Au over-layers. The over-layer metallisation is performed by depositing a thickness of 20 nm Ti and 150 nm Au using a Turbo Pumped Thermal Evaporator. The same lift-off and cleaning procedures described previously in Section 2.2.2 are followed (see Figure 2-1 e and Figure 2-2 e).

2.2.5 Substrate thinning

For the purposes of heat extraction from the sample to the copper block heat-sink and to improve THz radiation confinement, the process of substrate thinning is undertaken (see Figure 2-1 f). The sample is mounted up-side down on a glass slide and protected by a coating of Paraffin wax. The up-side down devices can be also protected by applying a thin layer of dry photoresist on a glass slide and then place the sample on the glass slide then bake them in oven at 50°C for 1 day until the resist is fully dried. The back-side etching process was performed using H_2SO_4:H_2O_2:H_2O solution in a ratio of 1:8:1 volume respectively [40] which gives and etch rate of 20 μm per minute. Only ~ 200 μm of the semi-insulating GaAs substrate is left in order to improve the heat removal from the active region through the copper block, onto the cold finger. During the etching process, the sample is checked using a surface profiler to measure the exact etching

rate and thickness to avoid over etching. The cleaning procedures described in Section 2.2.1 were applied.

2.2.6 Backside metallization

The back side of the sample is metallised using Ti/Au at a thickness of 20nm Ti and 100 Au to improve the adhesion between the sample and the copper block base (see Figure 2-1 f). The copper block is also cleaned and metallised with a Ti/Au layer. The last step in this process involves sintering the sample using RTA at 270°C for 4 minutes to improve the metal adhesion to the sample.

2.2.7 Cleaving facet

Extra care should be taken while cleaving using a scalpel blade as any crack can destroy the whole sample. The first step in cleaving is to separate the three 6 mm cavities in a chip, then to cleave each strip line into different lengths. Cleaving provides a very accurate, mirror-like facet on both sides of the device, which create the Fabry–Pérot cavity.

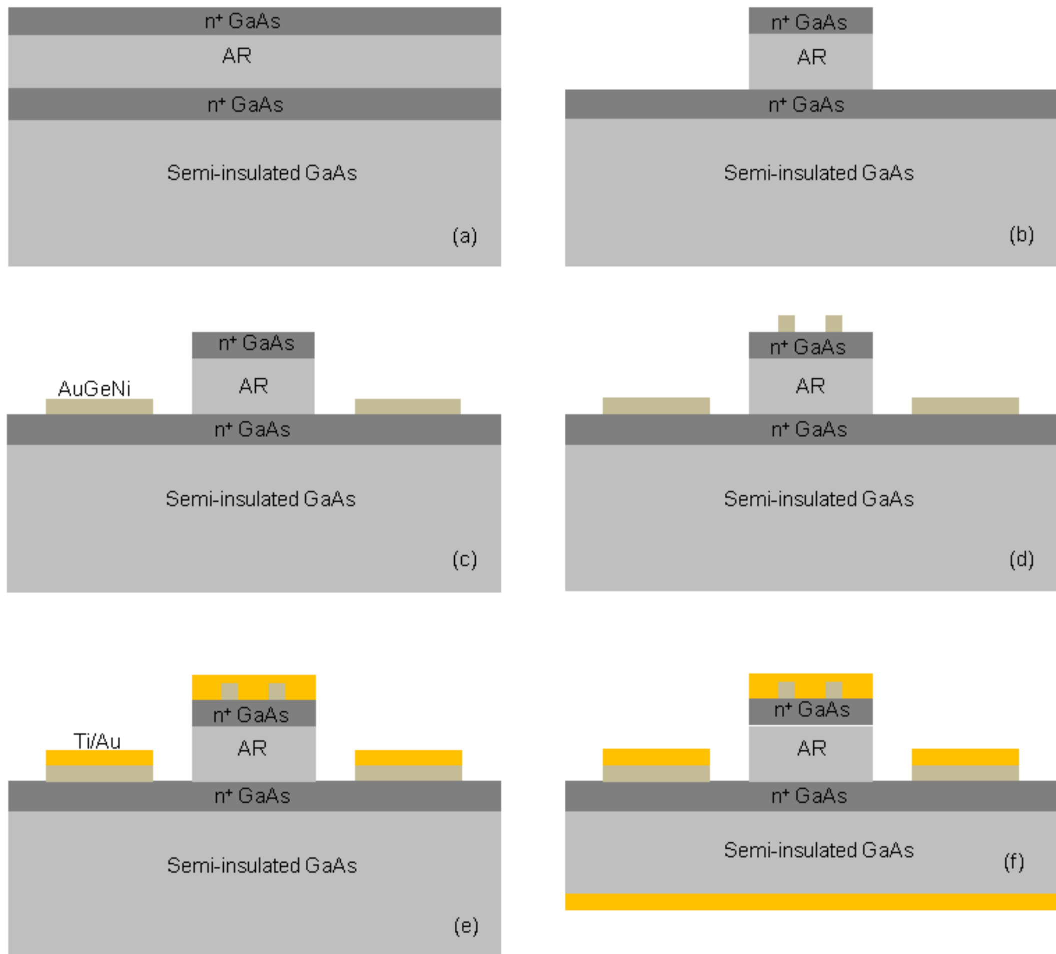

Figure 2-1: Schematic diagrams of the fabrication steps of a single metal QCL. (a) the unprocessed wafer, (b) mesa etching, (c) AuGeNi bottom contact, (d) AuGeNi top contact, (e) Ti/Au overlayer, and finally (f) substrate thinning and back side metallisation. AR is the active region. Figure not to scale.

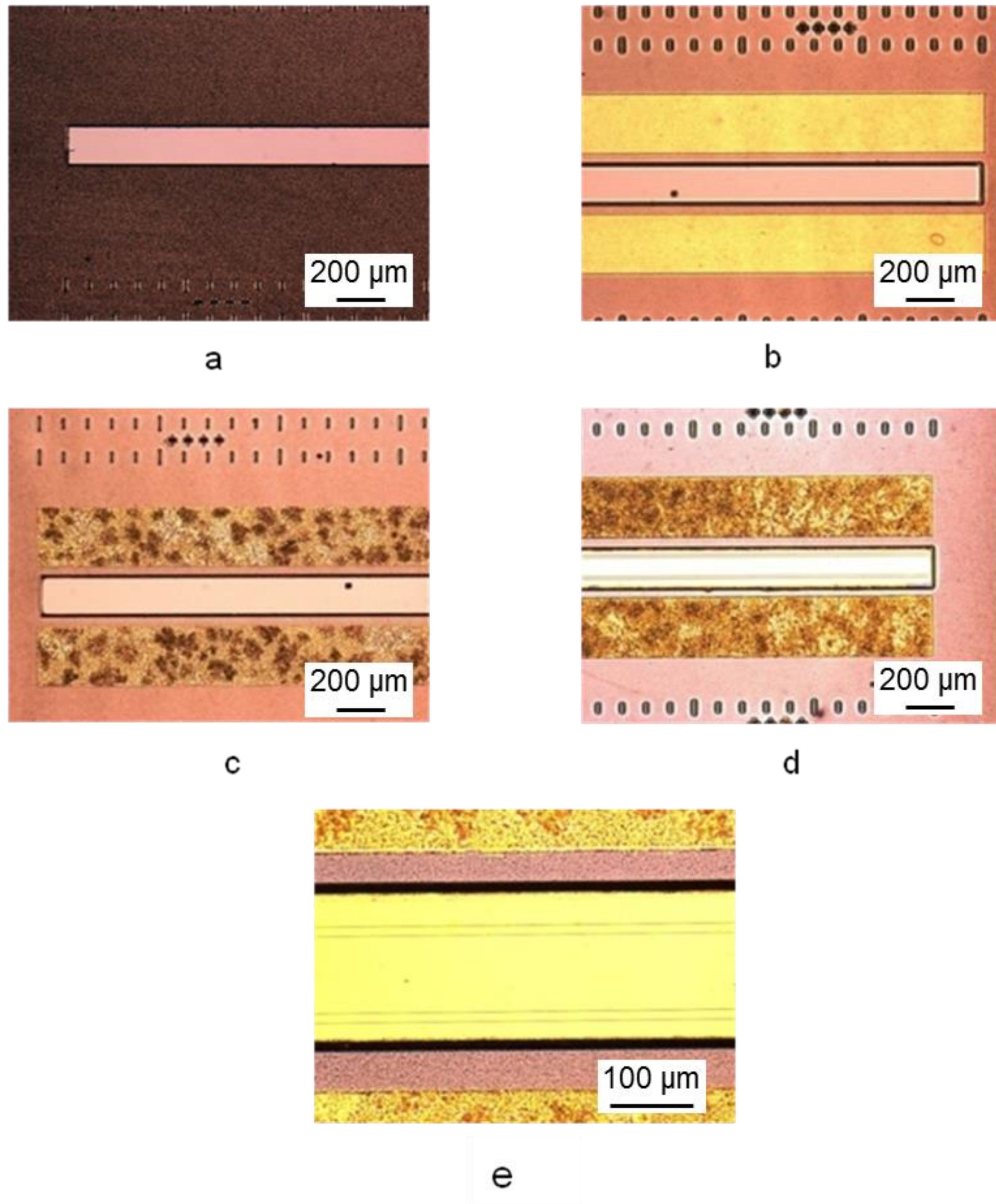

Figure 2-2: Top microscope views of a QCL at different fabrication steps. (a) mesa etching, (b) AuGeNi bottom contact, (c) bottom contact annealing, (d) AuGeNi top contact, and finally (e) Ti/Au overlayer. The mesa width in all figures is 150 µm.

2.2.8 Mounting and wiring the devices

To mount the sample on a gold coated copper block, three gold coated ceramic pads are stuck to the block using GE Varnish. The block is left to dry on a hot plate at 100°C for 5 minutes and the GE Varnish is hardened. A small piece of Indium (In) is placed on the gold coated part of the block to stick down the device chip and is spread smoothly and uniformly at a temperature of 150°C. Two devices were placed on each copper block and aligned on the Indium. A probe needle was used to apply pressure to the chip, pushing it down onto the Indium surface during the mounting process. The temperature is then increased to 170°C to melt the Indium. Once the temperature reaches 170°C it is immediately decreased to 100°C. Gold wire ball bonding is then used to connect the top and bottom contact of each device with their two respective ceramic pads (see Figure 2-3). Care should be taken at this stage to ensure the wires are not in contact with each other, forming an unwanted short circuit.

Figure 2-1 shows schematics of the fabrication steps of single metal QCL and Figure 2-2 shows microscope view of a QCL during six different processing steps.

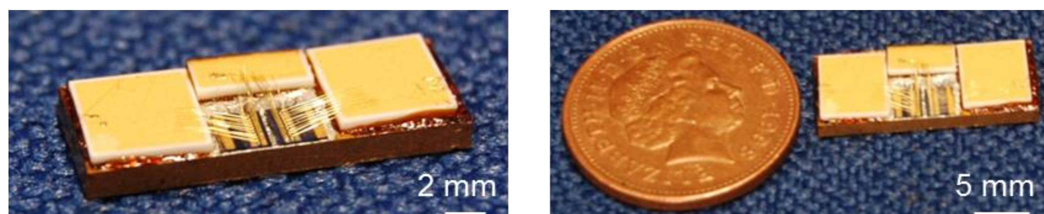

Figure 2-3: Two photos of a copper block with two single metal QCLs after mounting and wire bonding.

2.3 Fabrication of QCLs with angled facets

The THz QCL emission is typically obtained from the cleaved facet of a laser ridge. However, it has been demonstrated that THz QCL can operate with etched angled facets [41]. This design would allow the THz QCLs to be integrated with electrical photonic components. The optimisation of this design would pave the way for monolithic integration of QCLs into on-chip terahertz circuits. Such a development is also giving precisely fabricated devices.

The fabrication of THz QCLs with angled facets (Figure 2-4 and Figure 2-5) was needed in this work to facilitate the integration of THz QCL with Interdigitated transducers (IDTs). Processing these devices can be achieved using the same fabrication technique used for non-angle faceted QCLs described in Section 2.2 except for the process of ridge definition. The mesa is etched using a mixture of H_2SO_4:H_2O_2:H_2O in a ratio of 1:8:950 by volume. A magnetic stirrer is used to maintain homogeneity of the solution during etching. The rate of etching in the solution is ~ 40 nm/min. This diluted solution provides ~ 42° facet angle on the sloped laser facets [40]. Scanning electron microscope (SEM) is used to obtain an image to verified the angle measurement (see Figure 2-5 b) [41].

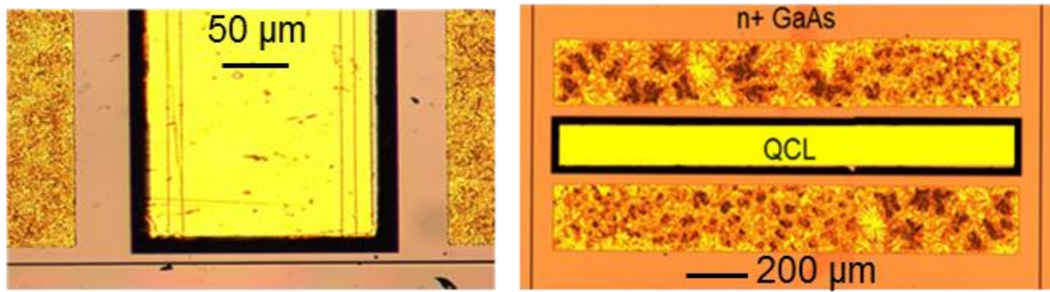

Figure 2-4: Top microscope views of angled facet QCLs.

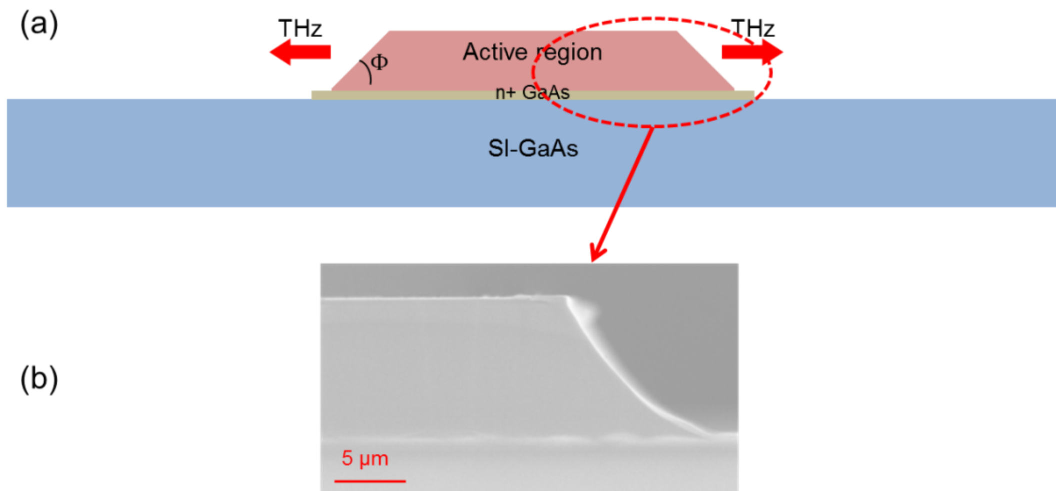

Figure 2-5: (a) Schematic diagram and (b) Scanning electron micrograph (SEM) of a THz QCL cavity formed by wet etching to provide sloped facets with angle $\Phi \sim 42^{o}$. Courtesy of [41]. Figure (a) not to scale.

2.4 Fabrication of interdigitated transducer

For the purpose of potential modulating of THz QCL frequency by surface acoustic waves (SAWs) [42], IDTs can be fabricated on bulk GaAs to generate SAWs, which will be explained further in Chapter 5. In this section the fabrication of IDTs will be illustrated. Fabricating IDTs requires precise processing to realise devices with features on the order of 3 μm, using optical lithography. In this work, each device has two IDTs – one for generating the SAWs and the other for detecting them. Each one of the two IDTs contained an array of metallic fingers. Since no metal contact could be allowed between adjacent fingers, a good finish using the lift-off process of the thermally evaporated metal is essential.

To fabricate IDTs with single-finger structure by conventional photolithography technique (as in Figure 2-6), a single resist layer technique was implemented. The sample is cleaned, spin coated, spun and baked as described in Section 2.2.1. Photolithography with a UV mask was used to make the IDT patterns. After developing the resist, described in Section 2.2.1, a Ti/Au layer (20/80 nm) is deposited using thermal evaporation. The lift-off step can then be performed as described in Section 2.2.2.

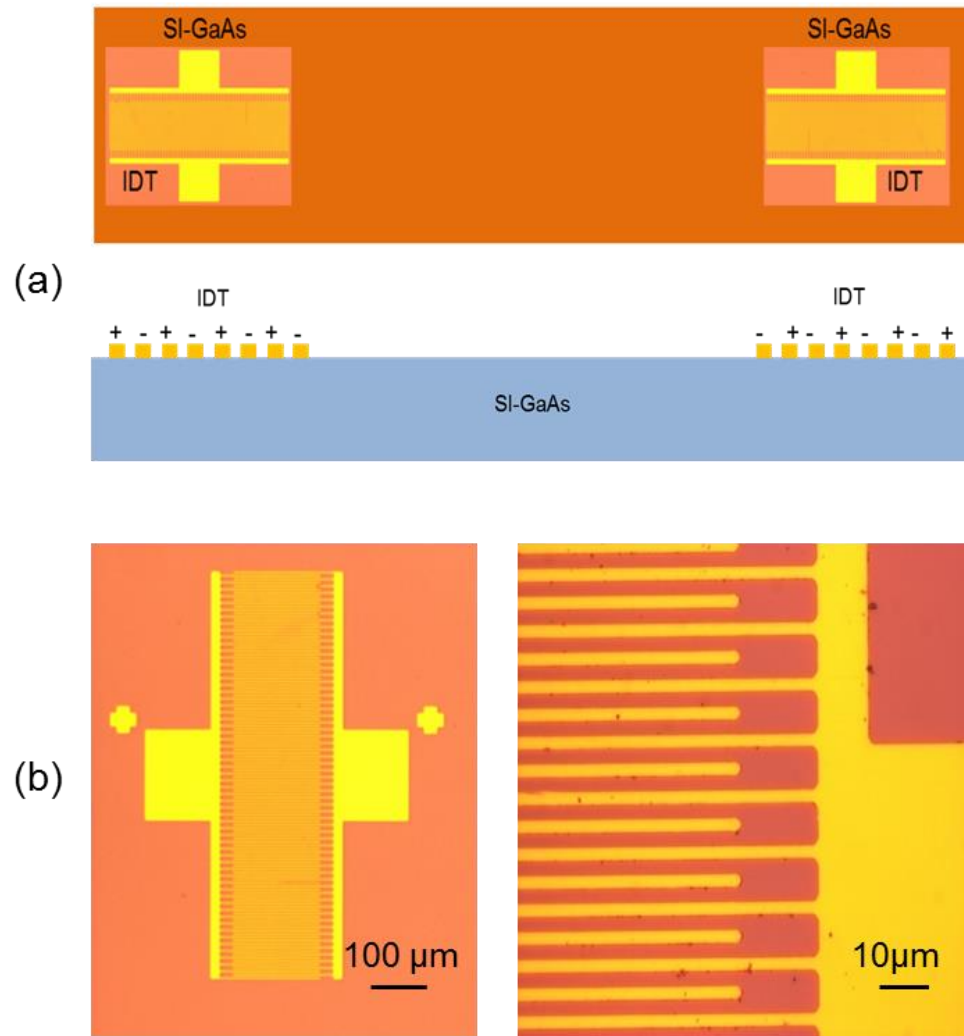

Figure 2-6: (a) Two schematic diagrams and (b) two top microscope views of IDTs fabricated on a SI GaAs chip. Figure (a) not to scale.

To mount the IDTs (Figure 2-7), a printed circuit board (PCB) was used instead of a copper block and ceramic pads as in the QCL devices described in Section 2.2.8. The PCB is etched in a ferric chloride solution with a designed mask at 70°C. To wire bond the devices, several gold pads are placed onto the PCB using silver epoxy as conductive glue. The IDTs are then connected to a network analyzer via SMA connectors to measure the Scattering parameters (S-parameters).

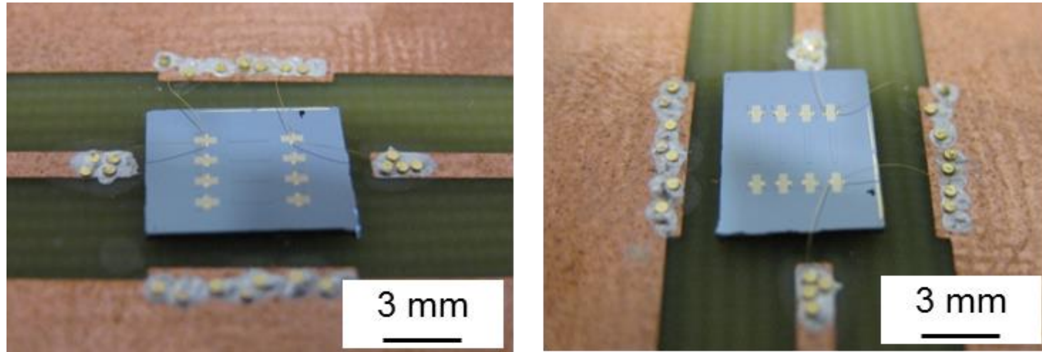

Figure 2-7: Top views of a GaAs chip containing four set of IDTs, in which one of them is wire bonded to a PCB through several gold pads.

2.4.1 Zinc oxide thin film deposition

In order to compensate for the weak piezoelectricity and low acoustic phase velocities of GaAs for monolithic integrated devices, a Zinc oxide (ZnO) thin layer was deposited on the top of the bulk GaAs before the IDTS are fabricated. To achieve efficient SAW excitation and to reduce SAW propagation losses, the ZnO film needs to maintain smooth surface morphology. The ZnO film is deposited on bulk GaAs using the Sputter coating process (The Kurt J. Lesker Company, PRO Line PVD 75 – Versatile Sputtering, Electron Beam, Thermal, & Organic Evaporation Deposition Platform). The ZnO target was 2.0 in. in diameter and 0.125 in. thick. The sputtering was undertaken under a pressure of 7×10^{-3} Torr, with a substrate temperature of 200°C, a power equal to 100 W and at a deposition rate of ~ 100 nm/h.

2.5 Fabrication of THz QCL with IDTs

The fabrication of THz QCL monolithically integrated with IDTs was achieved with the same processing procedure described in Sections 2.3 and 2.4. An extra step was introduced in fabricating the QCLs in order to remove the bottom n^+ GaAs layer in the area where the IDTs will be set. This step involved performing etching ~ 2 μm in both side of the ridge from the facet direction. The etched area allows SAWs to propagate on SI-GaAs. Etching down the bottom n^+ GaAs is necessary to provide a sufficient electrical bias to be applied between the IDT fingers. Fabricating the IDTs is performed before thinning the sample substrate. Figure 2-8 shows schematic diagrams and top microscope view of a single metal QCL integrated with IDTs.

The QCL and IDTs were mounted on a copper block as described in Section 2.2.8. The method described in Section 2.5 was implemented to wire bond the devices. Figure 2-9 shows two IDTs monolithically fabricated with a QCL mounted onto a copper block and wire bonded to two PCBs.

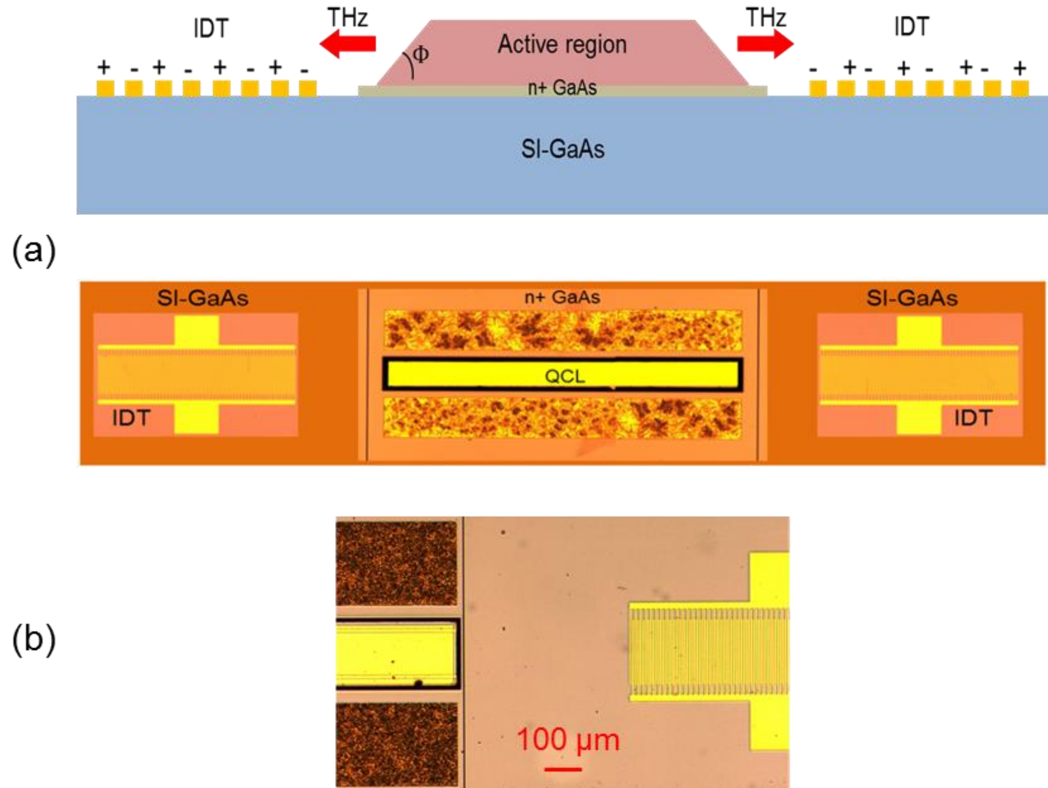

Figure 2-8: (a) Two schematic diagrams and (b) top microscope view of a single metal QCL monolithically integrated with IDTs. Figure (a) not to scale.

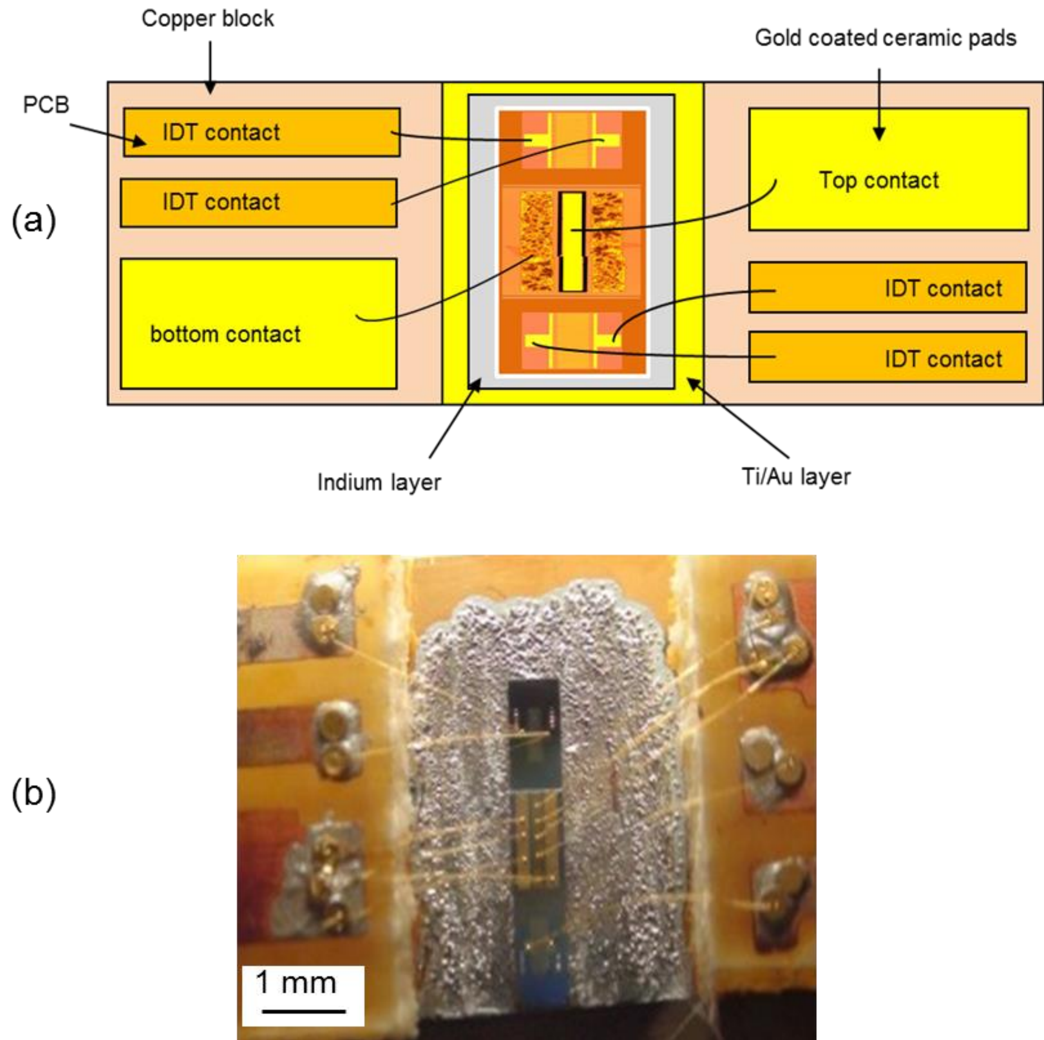

Figure 2-9: (a) Schematic diagram and (b) top view of two IDTs monolithically fabricated with a QCL all mounted onto a copper block and wired to two PCBs. Figure (a) not to scale.

2.6 Experimental setup

In this section, the experimental techniques used for electrical and optical characterisation of THz QCLs are detailed. Two different standard measurements were performed to characterise the devices. The first method was used to measures the transport characteristics of the devices by plotting current versus voltage (I-V) while measuring the power level of the output (L-I). The second measurement was used to measure the emission spectrum of the lasers.

Firstly, the two processed devices mounted on a copper block were mounted on the cold finger of a continuous flow Helium cryostat (Janis ST-100 optical cryostat) fitted with a polyethene (PE) window. The cryostat was placed in a purged enclosure to avoid absorption by water vapour of THz frequencies. The cryostat was then mounted on a X-Y-Z micrometer stage.

The lasers were electrically connected as shown in Figure 2-10 and driven in pulse mode at different temperatures and duty cycles with a pulse repetition rate of 10 kHz using a pulse generator (Agilent 8114A 100 V /2 A Pulse Generators). To control the temperature of the cold finger in the cryostat, a proportional-integral-differential (PID) controller (Lakeshore 331Temperature Controller) is used.

An oscilloscope (Tektronix TDS 2014) is used to measure the voltage that crosses the devices. Due to some of the devices requiring a high threshold current, a high frequency transformer (AV Tech Electro

systems AVX-MRBS) was used to double the current-voltage pulse taken from the pulse generator. The transformer output was also sent to an oscilloscope as a proportional voltage via a current probe that uses an induction loop to measure the current (for the setup used, 1 V ≡ 1 A).

For the transport characteristic and power mapping, the setup layout shown in Figure 2-11 is used. Two parabolic mirrors (f/0.8 and f/1.0) are utilized to collect the radiation from the lasers and focus it into the detector. A THz frequency thermal detector is used where the intensity of the incident light changes the electrical resistivity of the detector. The detector used is a composite silicon bolometer (TK1813, QMC Instruments Ltd) and operates at cryogenic temperatures of 4 K, provided by Liquid helium cooling and has a polythene window for optical access. It has a broad bandwidth detection and a sensitivity of 10.1 kV/W (at 80 Hz). To calibrate the responsivity of the bolometer a power meter (Thomas Keating THz Absolute Power Meter System) is used.

The emission from THz QCL is usually very weak, hence it is difficult to detect. This is because THz radiation absorbed by water in the atmosphere. Also, the background THz radiation can add extra noise to the signal. In addition, the detectors may introduce noise and have a limited sensitivity. Thus, using a lock-in detection technique is important to separate the QCL signal.

To detect the radiation with a lock-in technique and to meet the inherently slow responsivity of the bolometer, the current pulse that drives the laser is modulated with a chopping frequency of ~ 167 Hz. The

modulated output of the bolometer is fed into a lock-in amplifier (Amtek Signal Recovery Model 7225 Dual phase DSP Lock-in Amplifier) and measured by an oscilloscope to observe the output waveform.

To measure the THz radiation spectrum of the laser output, a second experimental setup was used (as illustrated in Figure 2-11). Three parabolic mirrors (f/1.0) were used to collimate the radiation. A spectrometer (Bruker IFS66/V FTIR) is used to determine the operating frequency of the device. In this setup the beam was fed into Fourier-Transform-Infra-Red spectrometer (FTIR) before guiding it into the bolometer. The spectral resolution in this system is 7.5 GHz.

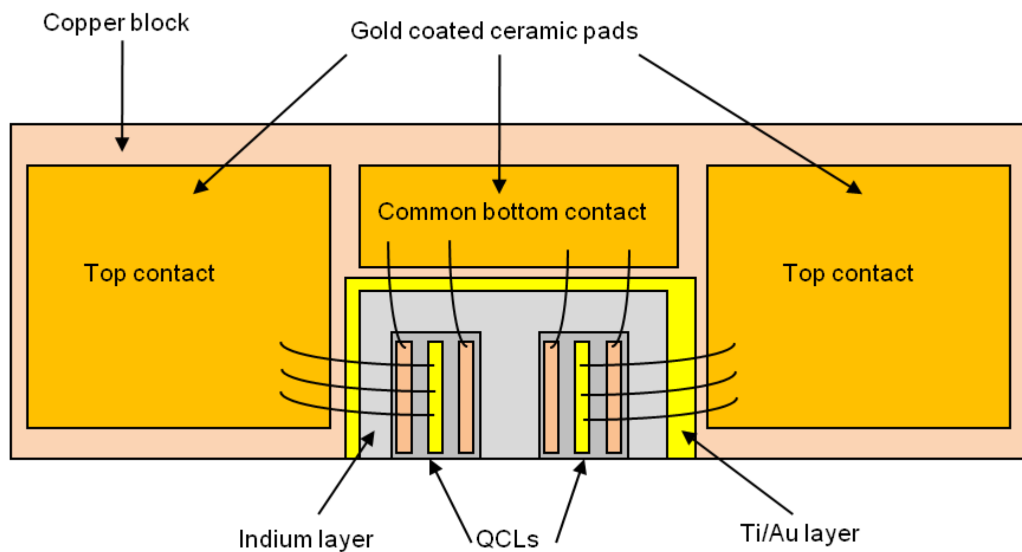

Figure 2-10: Schematic diagram shows two mounted QCL devices on a copper block. Electrical connections to the laser cavities also illustrated. Figure not to scale.

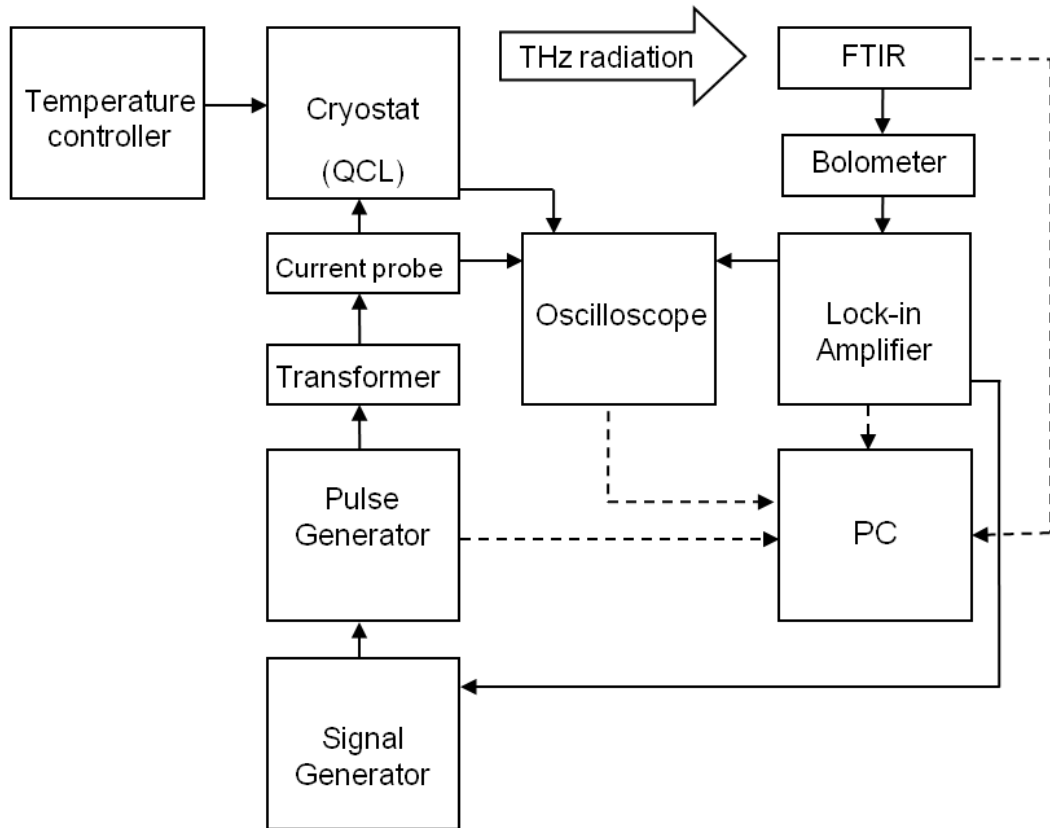

Figure 2-11: The layout of the Experimental setup used for radiation spectrum characterisation of a QCL. For power (L-I) measurements, the FTIR was excluded and the radiation was directly fed to the bolometer.

2.7 Summary

In this chapter, detailed description of the fabrication techniques for defining the devices used in this thesis is presented. The fabrication of single metal THz QCL waveguide is described. Next, the fabrication guide of QCL with angled facet is presented. The fabrication procedures of IDTs and integrating them with QCL are discussed. Finally, the experimental apparatus used to electrically and optically characterise the fabricated devices are presented. The use of FTIR spectroscopy to characterise QCL spectra was also presented.

The experience I gained in the fabrication and characterisation of THz QCLs allowed me to contribute to a published work of other people through supplying and testing part of the devices used in that project. Further details of this work are described in reference [43].

Chapter 3

Investigation of terahertz quantum cascade laser performance with thin etched active regions

3.1 Introduction

This chapter presents a systematic study on the performance of single metal terahertz quantum cascade lasers (THz QCLs) as the etch depth of the active region is changing.

THz QCLs are compact, semiconductor sources of narrowband THz frequency radiation. Owing to their coherence and high power, they are potentially well-suited for use in a broad range of application areas, including chemical sensing, industrial inspection, pharmaceutical analysing and imaging for security and biomedical applications [7, 19]. The

implementation of such applications requires in a number of cases the monolithic integration of the THz QCL with electronic and/or optical devices. For instance, since tunability THz QCLs would be highly beneficial for imaging and sensing applications [44], it has been suggested that QCL emission could be modified by surface acoustic waves (SAWs) providing a widely tunable single mode laser emission [42, 45]. In order to propagate SAWs over the top of THz QCL ridges (see Chapter 5) one could process interdigitated-transducers (IDTs) on both side of the laser facet. To facilitate the SAW travel over the laser cavity, the active region thickness/etch depth would then ideally be reduced without sacrificing performance. This requires development of QCLs with thin etched active regions.

It can also be noted that THz QCLs typically have an active region thickness of ~ 10 μm, but this thickness provide an obstacles to commercial exploitation. For example, to achieve the threshold electric fields, high operating voltages are required. This means that large electrical power is dissipated in the active region which leads to device heating [46]. As a result, continuous-wave (CW) operation of the laser is difficult to obtain, which is a condition for many applications [41, 47]. This effect is particularly significant in QCLs with high performance resonant phonon depopulation (RP) active region designs, which require a higher operating current density than chirped superlattice (CSL) [19] or bound-to-continuum (BTC) structure [32, 41, 47].

This chapter presents an investigation of the performance of THz QCLs with different active region designs and operating at different

frequencies, as the active regions etch thickness is reduced from the fully etched 10 μm down to 4.2 μm. In each case the active region was incorporated into a single metal waveguide. A similar study has been undertaken in metal-metal [48] and single metal [41, 47] waveguides. However, both studies focus on epilayers grown with thin active region, and not the partial etching of a structure. Section 3.2 will present the device parameters of the different THz QCLs studied. Section 3.3 focuses on characterisation of samples from wafer L559 in terms of threshold current density (J_{th}), the optical output power (P_{max}) and the maximum operating heat-sink temperature (T_{max}). Similar characterisation for other wafers will be presented in Section 3.4 where the electrical characterisation and output power of different thin etched active regions design will be discussed together with their output frequency. Section 3.5 will conclude the chapter.

3.2 Devices parameters

Twenty devices were fabricated based on either GaAs/AlGaAs three-well THz resonant-phonon depopulation (3-QW LO-RP) or BTC designs, with the active region etched to depth of 10, 8.5, 7.5, 6.5, 5 and 4.2 μm. All devices fabricated from wafers grown with a normal 10 μm (fully etched) active region thickness. As the samples were grown by MBE system at different operating times, the background doping levels may not be the same in different wafers, affecting the relative performance. Table

3-1 shows the dimensions, active region design and emission frequency of these devices (growth details tabulated in Appendix A).

The (±5%) error percentages in the laser width and etch depth correspond to the un-equal width and depth throughout the laser ridges owing to the nature of the chemical etching. As QCL in its typical geometry is a simple free-running Fabry–Perot, it is typically exhibit un-stable multiple longitudinal modes, therefore the optical frequency presented in Table 3-1 is the designed optical frequency.

The emission frequency given in Table 3-1 is the designed frequency when the wafers were grown. As can be seen in the table, twelve devices were fabricated from the same wafer (L559). This was to have a systematic study of the active region etched thickness without changing the wafer, active region design or the operating frequency. However, more devices were processed to investigate the effect of active region etched thickness on different wafers, active regions design and operating frequencies.

Wafer number	Length (mm)	Width (µm) ±5%	Etch depth (µm) ±5%	Active region design	Frequency (THz)
L559	1.5	150	10	3-QW LO-RP	3.1
L559	1.6	150	10	3-QW LO-RP	3.1
L559	1.5	150	8.5	3-QW LO-RP	3.1
L559	2.1	150	8.5	3-QW LO-RP	3.1
L559	1.1	150	8.5	3-QW LO-RP	3.1
L559	1.7	150	7.5	3-QW LO-RP	3.1
L559	1.5	150	7.5	3-QW LO-RP	3.1
L559	2.2	150	7.5	3-QW LO-RP	3.1
L559	1.2	150	7.5	3-QW LO-RP	3.1
L559	1.4	150	6.5	3-QW LO-RP	3.1
L559	1.9	150	5	3-QW LO-RP	3.1
L559	2.2	200	4.2	3-QW LO-RP	3.1
L647	3.1	150	11	BTC	2.6
L647	3.1	150	8.2	BTC	2.6
L281	1.2	150	10	3-QW LO-RP	4
L281	1.6	150	10	3-QW LO-RP	4
L281	1.2	150	7.5	3-QW LO-RP	4
L281	1.2	150	7.5	3-QW LO-RP	4
L645	1.8	150	10	3-QW LO-RP	3.1
L645	1.8	150	7.5	3-QW LO-RP	3.1

Table 3-1: The dimension, active region design and designed optical frequency of twenty devices used to investigate the changes to threshold current density, maximum operating temperature and peak power, all as a function of the etched active region thickness. All devices fabricated from wafers grown with a normal 10 µm active region thickness.

The fabrication steps are described in detail in Chapter 2 Section 2.2. Single metal waveguides were used owing to their high output power compared to double-metal waveguides and also for more uniform output beam profiles [41, 47]. Also, this waveguide was chosen as it allows lasing from etched-facet devices, rather than cleaved facet devices, thus facilitating the integration of SAWs on semi-insulating GaAs (as will be described in Chapter 5). As detailed in Chapter 2, optical lithography was used for defining laser ridges and ohmic contacts. The thicknesses of the AuGeNi bottom and top contacts were ~ 150 nm and ~ 100 nm respectively, and the thicknesses of the over-layer Ti/Au were ~ 20/150 nm.

The method used to vary the active region height was by wet etching the active region to different thickness (see Figure 3-1). The performance of each active region is expected to depend on the thickness of the active region as well as the cavity length and width [41].

Figure 3-1: Illustrative diagrams of two THz QCL with different etched thicknesses. The change in thickness was achieved through wet etching, where Ψ is the etch depth. Figure not to scale. The right diagram represents a fully etched (10 μm) device.

3.3 L559 devices characterisation

Before comparing the performance of different etched depth, each sample was characterized. The voltage-current density (V-J) plots and light-current density (L-J) plots for one device at each etch depth will be shown. Good agreement was obtained between samples with the same etch depth. After all samples were characterised, their performances were compared to investigate the effect of reducing the etch depth on the THz QCL. The experimental setup used to test and characterise the devices is described in details in Chapter 2 Section 2.6. In these measurements, the devices were characterised in pulsed mode, with a pulse repetition rate of 10 kHz, electrically gated by a 167 Hz square-wave, thus supplying each QCL with a driving pulse at 2% of duty-cycle. However, for the T_{max} measurements, the lowest duty-cycle at which lasing occurred was used to reduce heating. To improve the detection sensitivity, a lock-in amplifier was used. The peak power at 4 K was calibrated with a power meter (Thomas Keating THz Absolute Power Meter System).

3.3.1 L559 - 10 µm etch depth

Table 3-2 gives an overview of the performance for two different devices with 10 µm (fully etched) etch depth from wafer L559. The lowest value of J_{th} was 906 A/cm^2 from a 1.5 mm long device, whereas the two devices generate almost the same P_{max} and T_{max}. This can be understood as the two devices are not very different in their length. Figure 3-2 and Figure 3-3 show the V-J and L-J characteristics for L559 (10 µm etch

depth) at different temperatures, respectively, for the 1.50 mm × 150 µm device.

Length (mm)	Width (µm) ±5%	J_{th} (A/cm^2) ±2%	P_{max} (mW) ±10%	T_{max} (K) ±5%
1.5	150	906	16.4	106
1.6	150	953	16.5	103

Table 3-2: Performance overviews of two different devices fabricated from L559 with 10 µm etch depth (fully etched).

The error percentages in Table 3-2, and in other tables in this Chapter, are due to different reasons range from the nature of the chemical etching, to facet cleaving issues, to laser beam alignment, to heat-sink temperature and cooper block mounting.

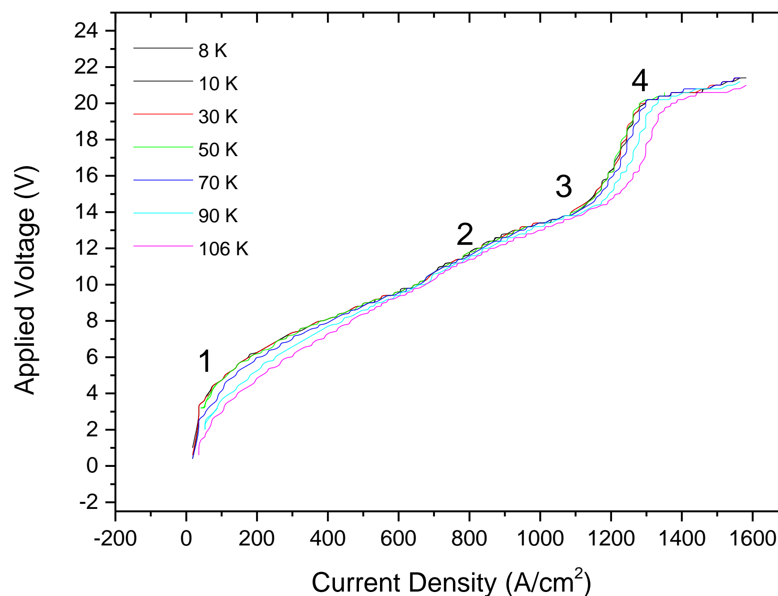

Figure 3-2: The V-J characteristics of L559 (10 µm etch depth) for 1.50 mm × 150 µm device at different temperatures.

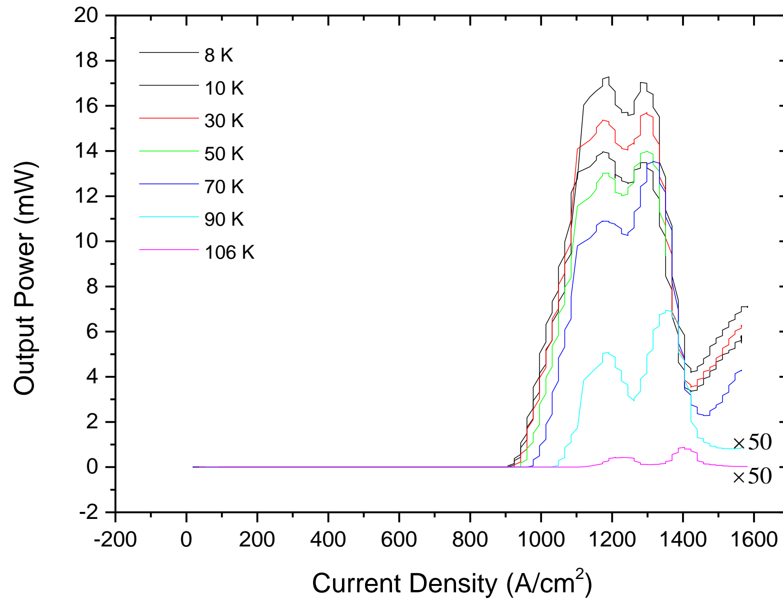

Figure 3-3: The L-J characteristics of L559 (10 μm etch depth) for 1.5 mm × 150 μm device at different temperatures. The unsmooth nature of the line is due to experimental limitation.

There are four features present in this V-J plot (see Figure 3-2). In feature 1 (see also Figure 3-5 a), the current increases rapidly. This feature happens when the energy levels responsible for the parasitic conduction channel become into alignment with each other [49]. The reason of this is that the injected electron from the previous period (come from level 1', see Figure 3-4) is injected to level 2 (lower laser level) instead of 4 (upper laser level) [28]. Feature 2 occurs when the parasitic conduction channel is stopped and the electron injected from level 1' of the previous period to level 4 (upper laser level). Just after this feature the system reaches threshold (see Figure 3-5 b). The pinching point in feature 3 occurs when the conductance of the device decreases dramatically (see Figure 3-5 c). This is caused by the misalignment, again, between level 1' and 4 [50]. In feature 4 the current increase dramatically owing to the separation between the two laser levels being ~ 36 meV which means the phonon induced non-lasing channel (PNC) is start to open [28].

The two peaks in the L-J (Figure 3-3) may be attributed to the mode hopping between two frequencies, which are clearly suggested by the laser emission spectra in Figure 3-6.

Figure 3-4: Conduction band diagram of 3QW LO-phonon design [51].

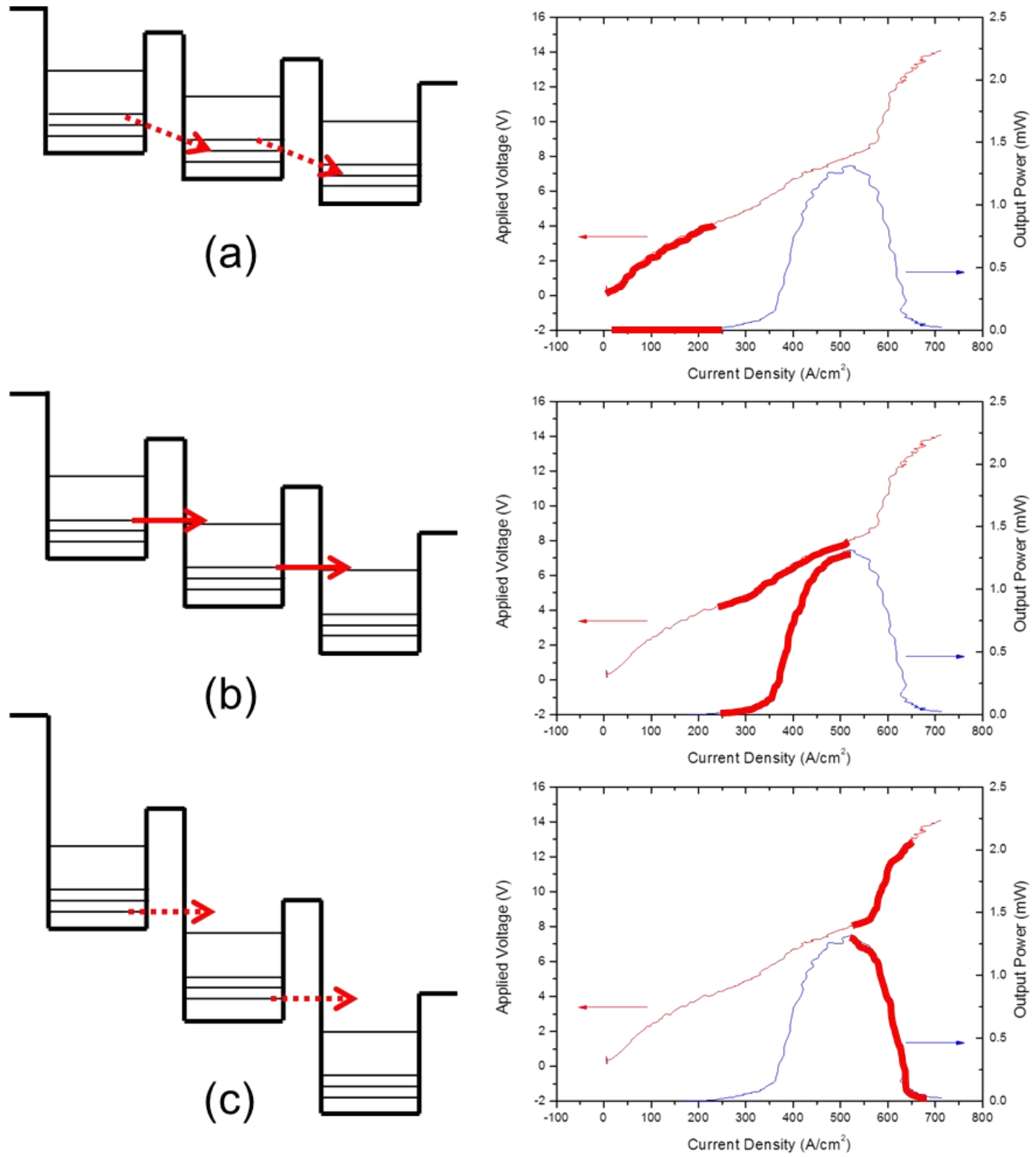

Figure 3-5: Illustration diagrams correspond to current injection stages in a THz QCL. At (a) the parasitic conduction channel become into alignment with each other, (b) correspond to the threshold and lasing stage and at (c) the conductance of the device decreases dramatically. The LIV plots used in this figure is for illustration only.

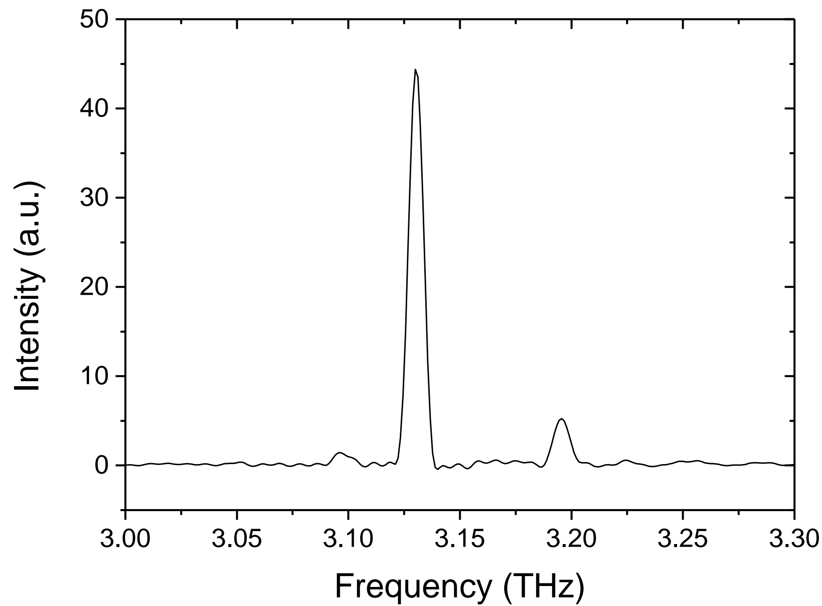

Figure 3-6: The emission spectra of 3.1 THz of L559 (10 µm etch depth) for 1.5 mm × 150 µm device. The spectra were taken at 16 kV/cm and a heat-sink temperature of 10 K. The spectra are normalized relative to its maximum value for a given device.

3.3.2 L559 - 8.5 µm etch depth

Table 3-3 shows an overview of the performance for three different devices with an 8.5 µm etch depth. As expected, the longest device (2.1 mm) produced the largest peak power (35 mW) amongst the three devices a result of the increased area of the gain medium. The device with a length of 1.5 mm surprisingly emitted less power than the device of 1.1 mm. This can be attributed to the poor quality of the cleaved facet. The maximum heat sink temperature measured at 1.4 % duty cycle was 108 K for the longest device (2.1 mm). Figure 3-7 illustrates the V-J and L-J characteristics for L559 (8.5 µm etch depth) at 4 K. of a device of

dimensions 2.1 mm × 150 µm, The T_{max} was 108 K and it was measured at 1.4 % duty-cycle.

Length (mm)	Width (µm) ±5%	J_{th} (A/cm^2) ±2%	P_{max} (mW) ±10%	T_{max} (K) ±5%
1.1	150	960	23	104
1.5	150	930	13	104
2.1	150	985	35.5	108

Table 3-3: Performance overviews for three different devices fabricated from L559 with an 8.5 µm etch depth.

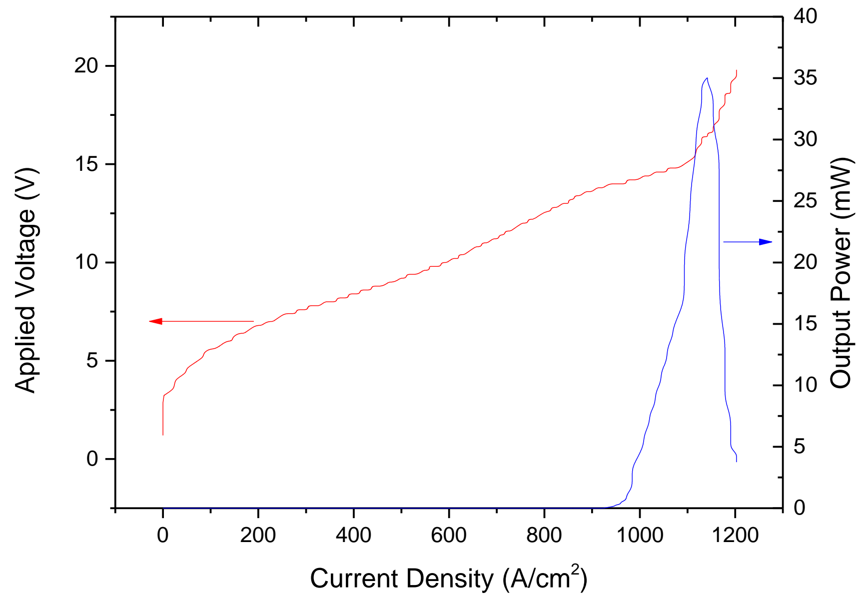

Figure 3-7: The V-J and L-J characteristics of L559 (8.5 µm etch depth) for 2.1 mm × 150 µm device at 4 K.

3.3.3 L559 - 7.5 µm etch depth

In Table 3-4, an overview of the performance of four devices fabricated from wafer L559, all with a 7.5 µm etch depth, is shown. The longest device (2.2 mm) produced the largest peak power (53 mW). J_{th} for these lasers varied from ~ 950 to ~ 1100 A/cm^2 and T_{max} between 110 and 120 K. Figure 3-8 shows the V-J and L-J characteristics for L559 (7.5 µm etch depth) at different temperature. For a device of 1.5 mm × 150 µm dimensions, the T_{max} was 117 K and it was measured at 0.7 % duty-cycle. The relation between J_{th} and duty-cycle at 4 K is presented in Figure 3-9. It can be seen from the figure that the highest electrical current for lasing occurs around a 2 % duty-cycle where the highest output power is produced.

Length (mm)	Width (µm) ±5%	J_{th} (A/cm^2) ±2%	P_{max} (mW) ±10%	T_{max} (K) ±5%
1.2	150	950	32	110
1.5	150	1100	45	112
1.7	150	960	50	120
2.2	150	970	53	110

Table 3-4: Performance overviews for four different devices fabricated from L559 with 7.5 µm etch depth.

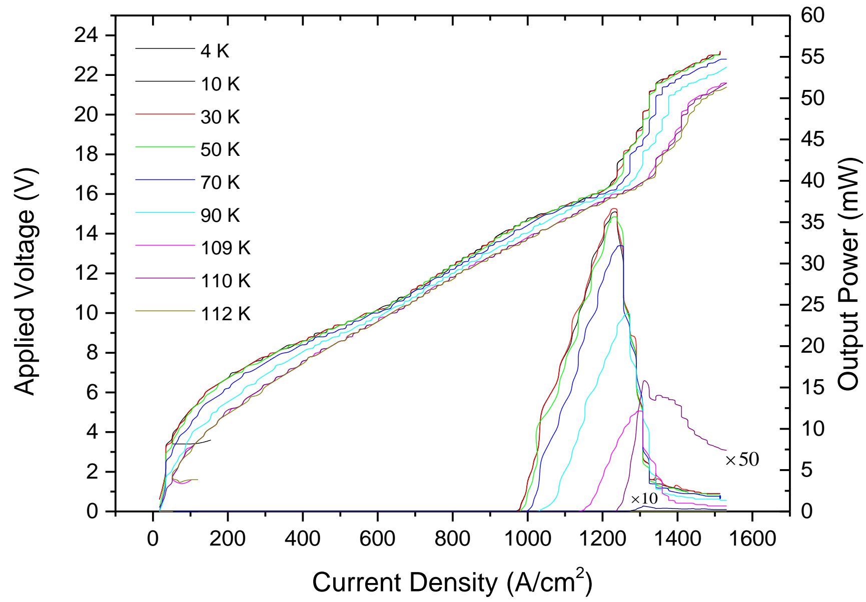

Figure 3-8: The V-J and L-J characteristics of L559 (7.5 µm etch depth) for 1.5 mm × 150 µm device at different temperatures. The unsmooth nature of the line is due to experimental limitation.

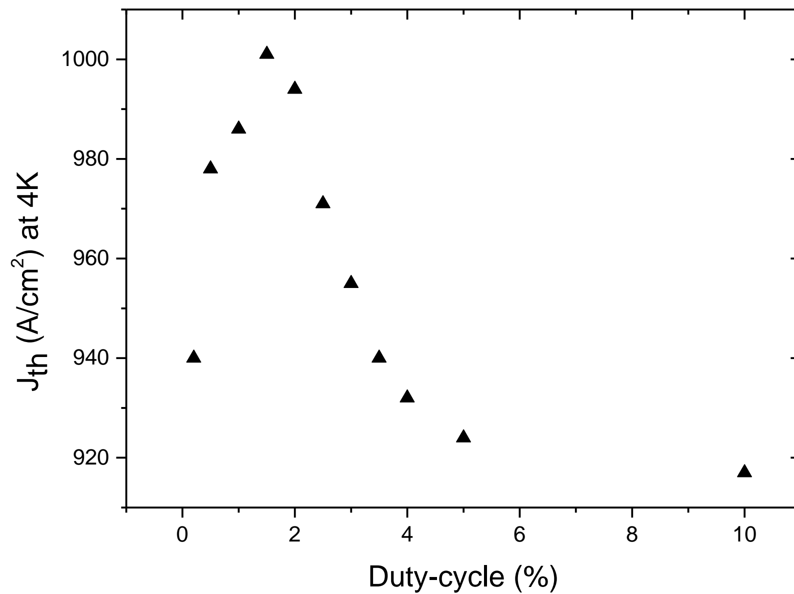

Figure 3-9: The relationship between J_{th} and duty-cycle at 4 K for the device 1.5 mm × 150 µm × 7.5 µm dimension etch depth.

3.3.4 L559 - 6.5 µm etch depth

Table 3-5 shows an overview of the performance for three different devices with a 6.5 µm etch depth. Only one device was working, the other did not lase. J_{th} was 1050 A/cm^2, P_{max} was 11 mW and T_{max} was 95 K when operating the device at a 2 % duty-cycle. Figure 3-10 shows the V-J and L-J characteristics for this 1.7 mm long device taken at 4 K. The 1.4 mm long device, fabricated from the same wafer has the same active region thickness, but did not lase. This could be because of the reduced gain medium caused by thinning the active region and reducing the device length.

Length (mm)	Width (µm) ±5%	J_{th} (A/cm^2) ±2%	P_{max} (mW) ±10%	T_{max} (K) ±5%
1.4	150			
1.7	150	1050	11	95

Table 3-5: Performance overview for two different devices fabricated from L559 with a 6.5 µm etch depth.

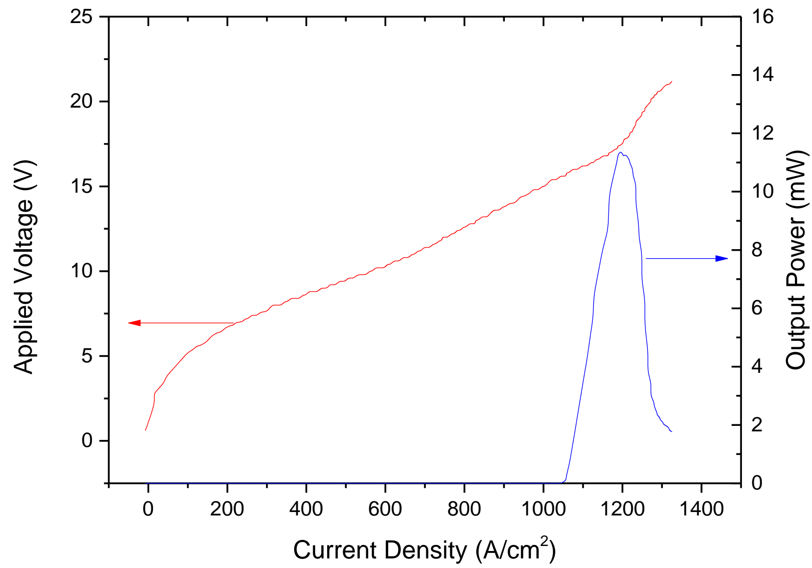

Figure 3-10: The V-J and L-J characteristics of L559 (6.5 μm etch depth) for 1.7 mm × 150 μm device at 4 K.

3.3.5 L559 - 5 μm etch depth

Table 3-6 shows an overview of the performance for one device with a 5 μm etch thickness. T_{max} was 64 K when operating the device at a 2% duty-cycle. Figure 3-11 shows the V-J and L-J characteristics for L559 (5 μm etch depth) at different temperature, respectively.

Length (mm)	Width (μm) ±5%	J_{th} (A/cm^2) ±2%	P_{max} (mW) ±10%	T_{max} (K) ±5%
1.9	150	1160	1.5	65

Table 3-6: Performance overviews for device fabricated from L559 with a 5 μm etch depth.

Figure 3-12 presents the V-J characteristics at different duty-cycle. As can be found in Table 3-6, despite the slightly longer length of the 5 μm

etch depth device, lower active region temperature is maintained when compared to the standard 10 μm etch depth devices.

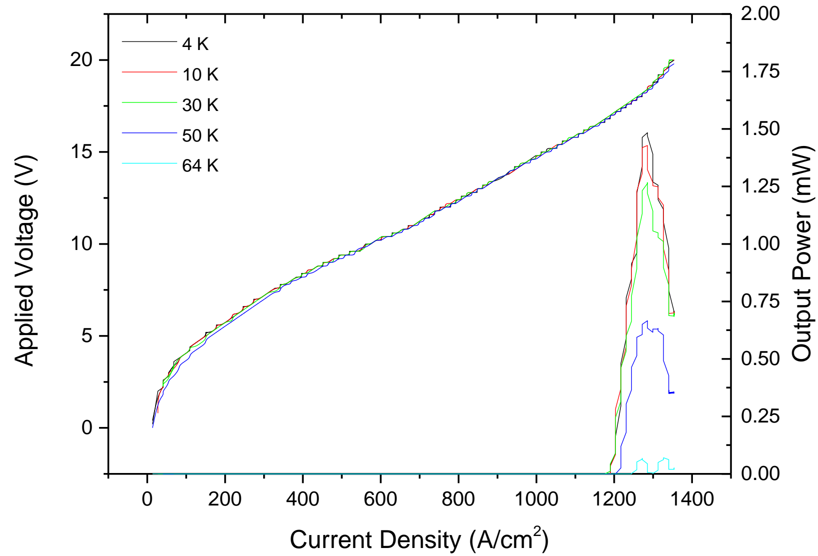

Figure 3-11: The V-J and L-J characteristics of L559 (5 μm etch depth) for 1.55 mm × 150 μm device at different temperatures.

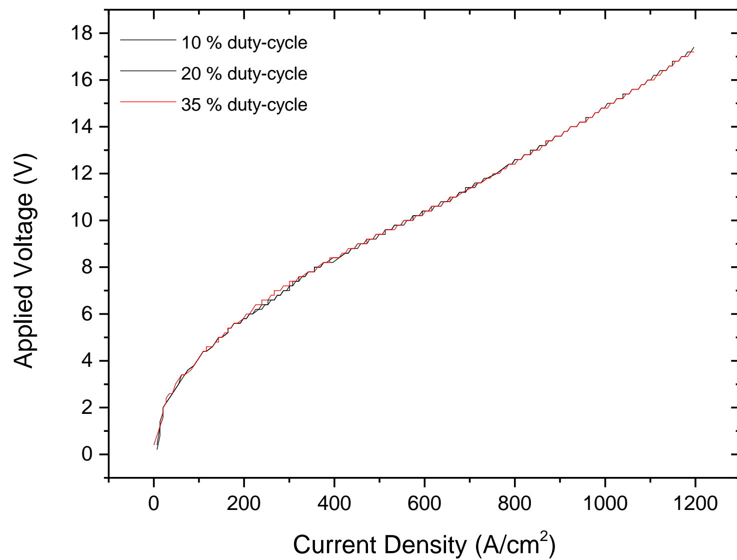

Figure 3-12: The V-J characteristics of L559 (5 μm etch depth) for 1.9 mm × 150 μm device at different duty-cycle.

3.3.6 L559 - 4.2 μm etch depth

For this active region thickness, only one device was fabricated and tested. The length of this device was 2.2 mm and the width of the ridge was 200 μm. The active region cavity was processed wider than other devices in order in compensate for the reduced gain medium. Nonetheless, this device did not lase.

A possible reason for the absence of lasing from the device with 4.2 μm etch depth is that as the optical confinement factor (Γ) is becoming smaller and the waveguide absorption is higher, this may prevent lasing in 4.2 μm thick active region device. This is because the devices would have reached the negative differential resistance (NDR) region before lasing starts. Another possible reason for the absence of lasing in this device is that the gain medium is small, thus the gain could be more easily exceeded by the higher waveguide absorption associated with thinner active region [41, 47].

3.3.7 L559 devices discussion

Figure 3-13 shows the V-J relationship for a number of devices from wafer L559 of different cavity length from 10, 8.5, 7.5 and 5 μm etch active region. It can be seen that the active region dimensions has low impact on the V-J relationship. This can be understood as the current path stays unchanged when the device is partially etched (see Figure 3-15).

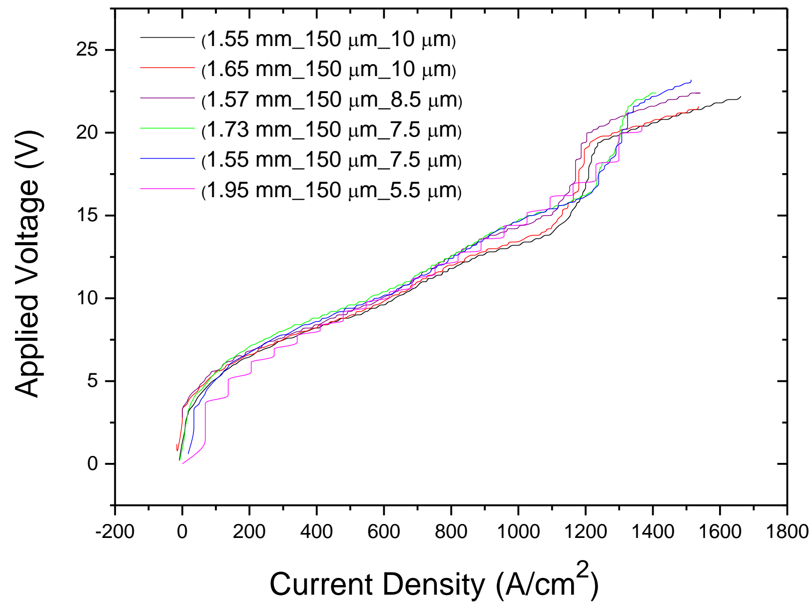

Figure 3-13: The V-J relationship for a number of devices from wafer L559 of different cavity length from 10, 8.5, 7.5 and 5 µm etched depth. The dimension of each device (length × width × thickness) is shown in the legend. The unsmooth nature of the line is due to experimental limitation.

The maximum operating temperature correspondingly fell from 120 K to 65 K. The maximum peak output power was ~ 53 mW in 7.5 µm higher than all other devices from different active region thickness. Figure 3-14 shows the L-J taken for three devices one with 10 µm and two with 7.5 µm. The maximum peak output power for the 7.5 µm devises is about 3 times higher than the 10 µm thick active region device.

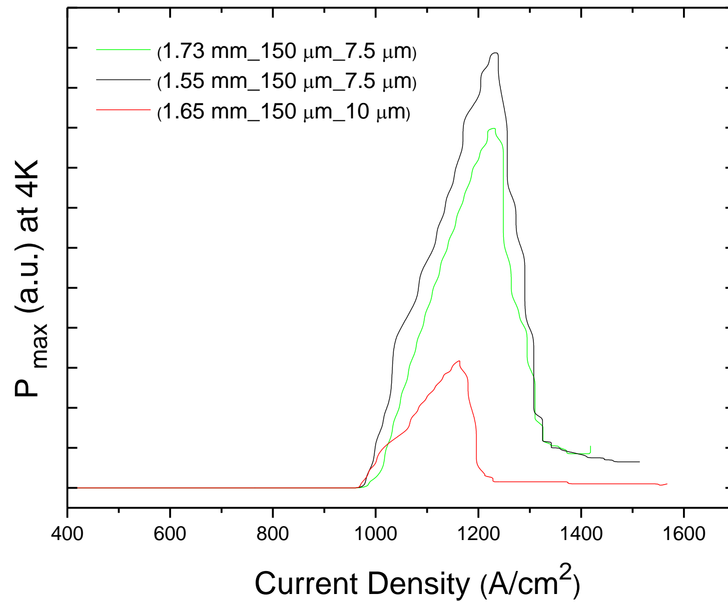

Figure 3-14: The L-J characteristics comparison of L559 (10 and 7.5 μm thick active region) at 4K and 2 % duty-cycle. The dimension of each device (length × width × thickness) is shown in the legend.

The results of this investigation show that regardless of the etch depth of the active region; the current density show no significant change over the range of samples suggesting that the current path is independent of the etch depth (Figure 3-15). However, except for 7.5 μm devices, the radiation output power and the maximum operating heat-sink temperature exhibit degradation as the active region etch thickness reduced. This degradation can be attributed to the additional losses in the unbiased structure below the bottom contact. Moreover, the left (un-etched) structure causes optical absorption and do not contribute to the gain. Also, the low optical mode confinement, along with the difficult output coupling compared to the planer structure made the laser degradation even worse. Though, these structures did offer better heat extraction. Therefore, the 7.5 μm

devices work best for L559 and that may be due to having the highest operating bias and better heat extraction.

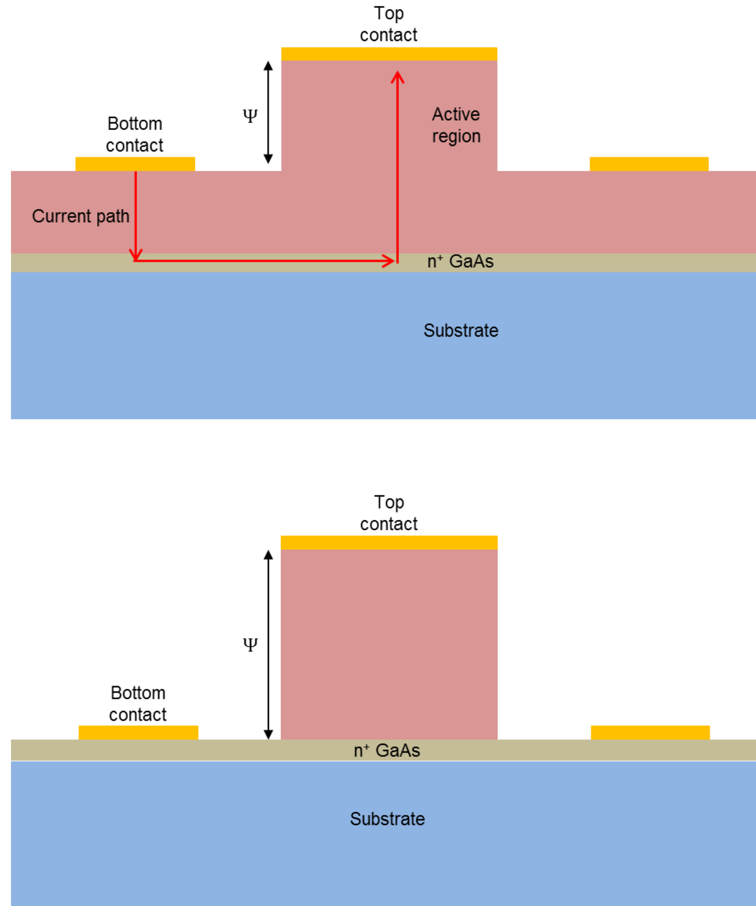

Figure 3-15: Schematic diagrams for two devices with different etch depth Ψ. The current path is illustrated by the red arrows. Figure not to scale.

Figure 3-16 shows the relationship between the J_{th} and heat sink temperature for different thick active region devises. Figure 3-17 illustrate summary three plots to illustrate the effect of changing the etch depth on (a) J_{th}, (b) P_{max} and (c) T_{max} for a number of devices from wafer L559. An increase in threshold current density from ~950 A/cm^2 to ~1200 A/cm^2 was observed (Figure 3-17 a) as the etch depth decreased from 10 to 5 µm. The increased J_{th} and reduced T_{max} (Figure 3-17 c) are attributed to the

reduced active region confinement factor (Γ) and increased waveguide losses in thinner etched devices [47]. Another possible reason for the increase in J_{th} when reducing the etch depth of the active region (Figure 3-17 a) is the current leakage into the left (un-etched) area of the active region underneath the ridge (see Figure 3-1). As this area is large (~ 500 µm wide) and it also does not confine the electrical field within the active region this issue makes the lasing condition difficult to achieve, thus increasing the required threshold current density. The un-etched area, aside from not contributing to the lasing gain, may contribute destructively to the optical absorption owing to the free carrier losses in the active region within the doping area.

Figure 3-17 (b) summarizes the maximum peak output power for the tested devices from wafer L559. As can be seen, the 7.5 µm devices exhibit the largest P_{max} among all devices from different active region etch depths. Similarly, 7.5 µm etch depth active region devices exhibit larger T_{max} in comparison to other devices (Figure 3-17 c). This can be attributed to the optimal heat extraction of these devices.

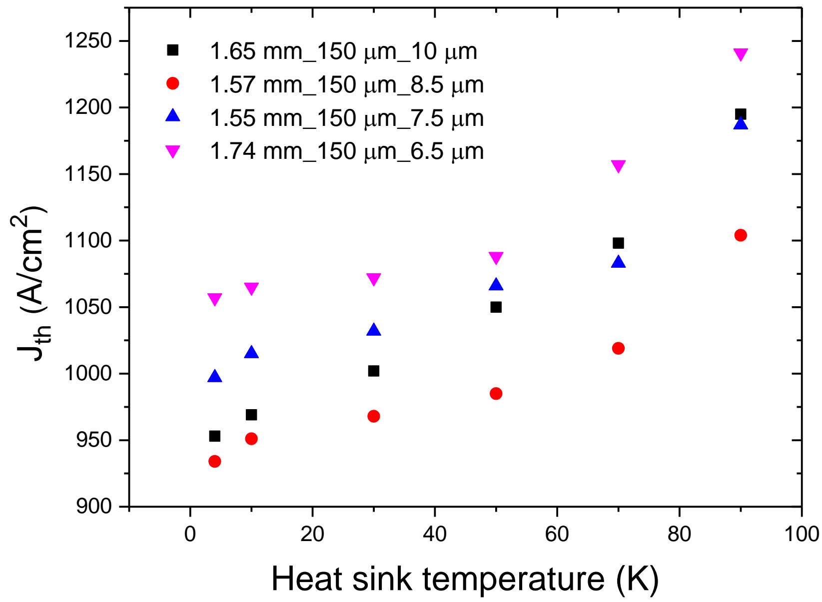

Figure 3-16: The relationship between J_{th} and heat sink temperature for different thick active region devises. The dimension of each device (length × width × thickness) is shown in the legend.

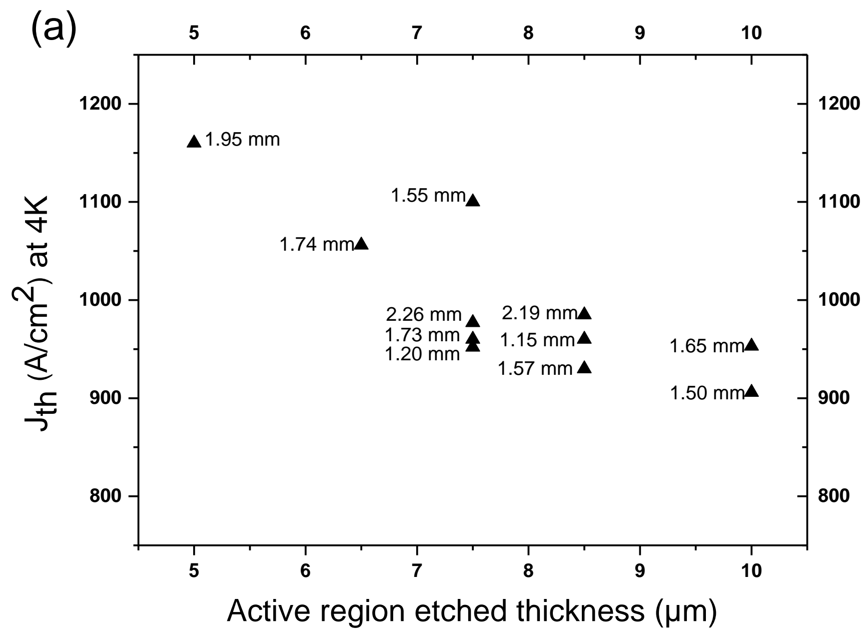

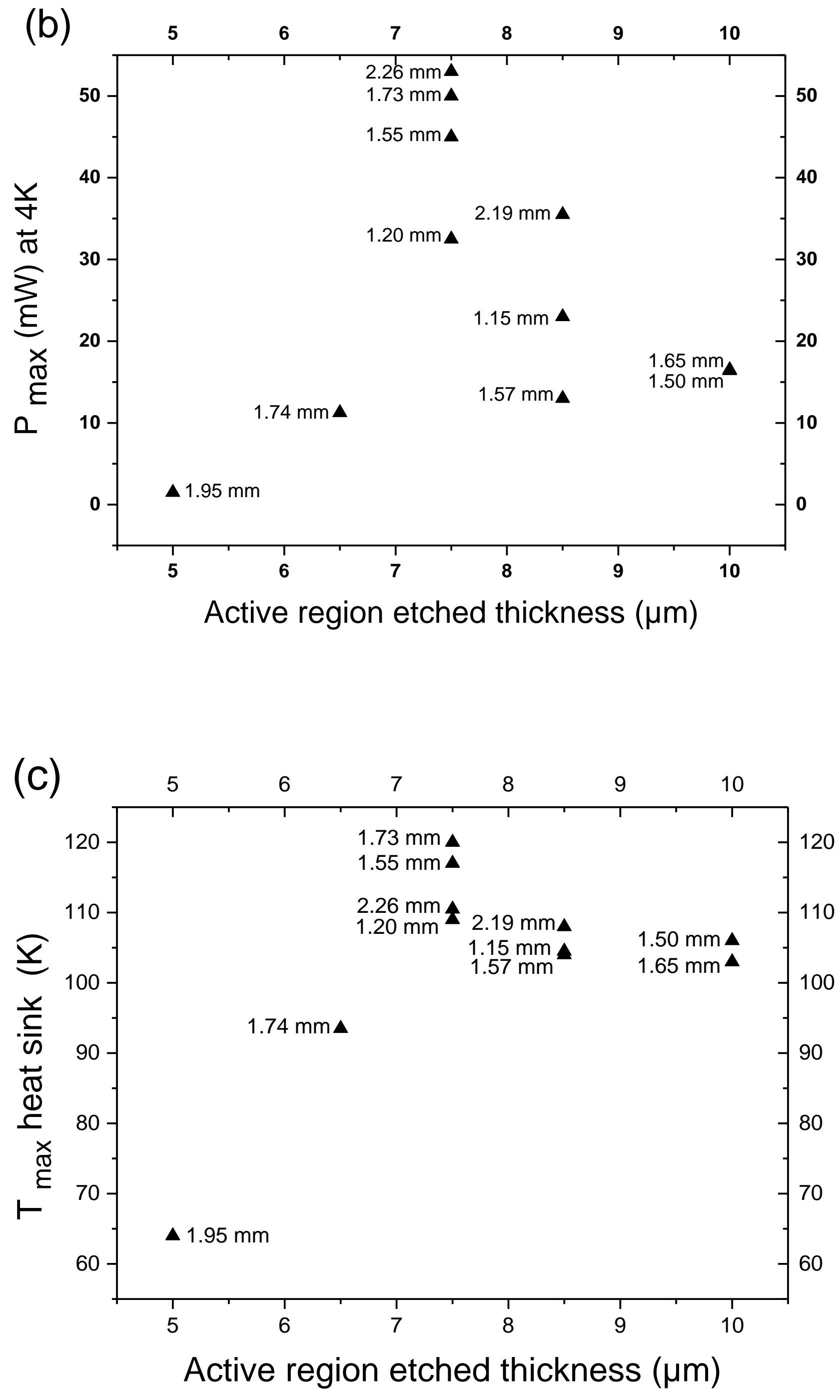

Figure 3-17: Summary three plots to illustrate the effect of changing the etch depth on (a) J_{th}, (b) P_{max} and (c) T_{max} for a number of devices from wafer L559. The length of each device is shown in the figures.

3.4 Devices characterisation for different active region

In Section 3.3, the results show that devices with 7.5 µm etch depth from wafer L559 exhibit larger P_{max} and T_{max} amongst the other devices from the same wafer but with different etch depths. In order to investigate this finding, eight more devices were fabricated, characterised and their results compared (see Figure 3-18). Table 3-7 shows an overview of the performance for eight different etch depths from the wafers L281, L645 and L647. The active region design and optical frequency for these devices are presented previously in Table 3-1 in Section 3.2.

Wafer number	Length (mm)	Width (µm) ±5%	Etched (µm) ±5%	J_{th} (A/cm^2) ±2%	P_{max} (mW) ±10%	T_{max} (K) ±5%
L281	1.22	150	10	863	51.5	107
L281	1.61	150	10	860	55	112.5
L281	1.21	150	7.5	943	38	103.5
L281	1.50	150	7.5	975	50	104.5
L645	1.86	150	10	860	75	123.5
L645	1.80	150	7.5	1050	20	99.5
L647	3.1	150	11	190	8.25	84
L647	3.1	150	8.2	230	5	76.5

Table 3-7: Performance overview for eight devices with different etch depths from the wafers L281, L645 and L647.

As can be seen from Table 3-7, the 7.5 µm thin active region devices did not show the same trend present with samples from wafer

L559. The 10 μm devices here always produce higher power and operate at higher heat sink temperature.

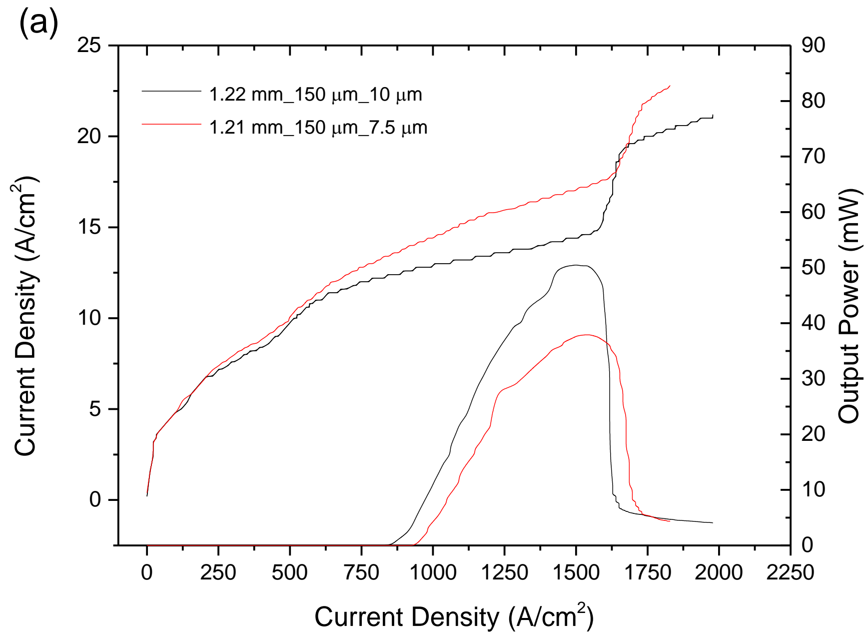

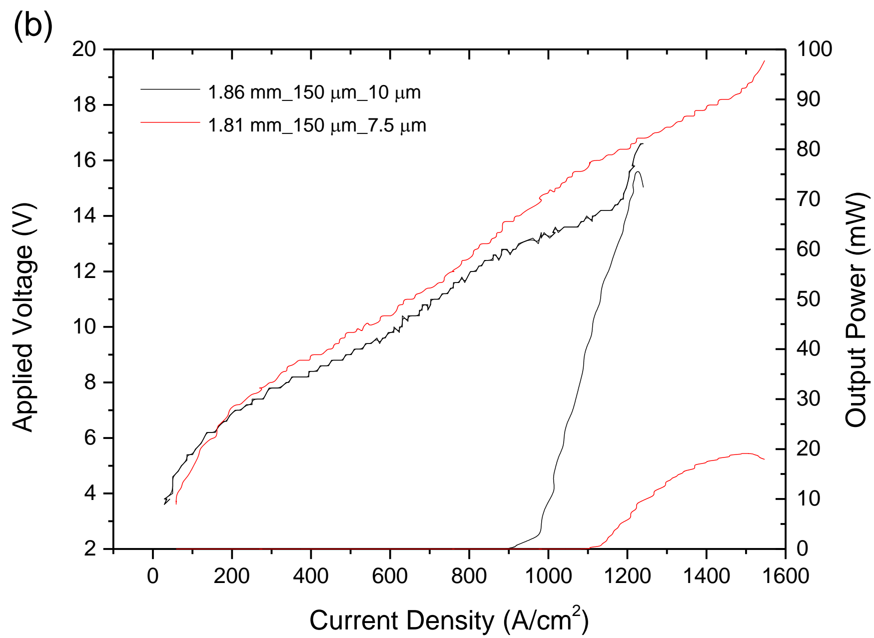

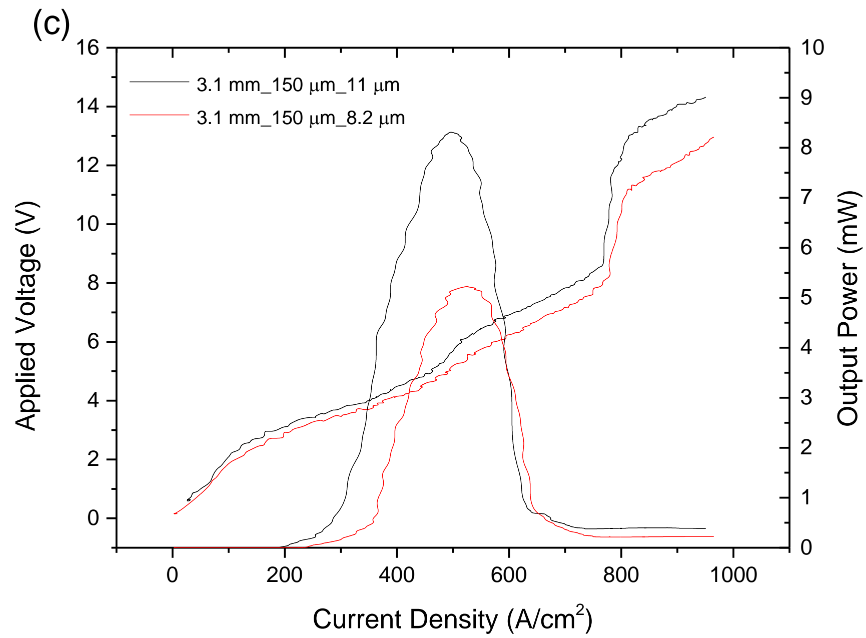

Figure 3-18: Comparison V-J and L-J characteristics between one 10 µm and 7.5 µm etch depth devices for the wafers (a) L281 (b) L645 and (c) L647. All measurements were taken at 4 K. The dimension of each device (length × width × thickness) is shown in the legend.

3.5 Conclusion

This chapter has presented an investigation of the THz QCLs performance based on different active region design operating at different frequency, as the active region etched thickness was reduced from 10 μm (fully etched) down to 4.2 μm.

In Section 3.3, the samples taken from wafer L559 were characterised in term of the threshold current density (J_{th}), the optical output power (P_{max}) and the maximum operating heat-sink temperature (T_{max}). Similar characterisations but for different wafers were presented in Section 3.4 where the electrical and output power properties of different thin etched active region designs and output frequencies were discussed.

This studies show that the etch depth of the active region has no effect on the current density. This could be attributed to independency of the current path on the etch depth as described in Figure 3-15.

Due to poor optical confinement in thinner etched active region, waveguide loss is expected to increase and the confinement factor expected to decrease, thus leading to increase in J_{th}. Also, the increase in J_{th} when reducing the thickness of the active region by wet etching (see Figure 3-1) may be due to the current leakage into the partially etched area of the active region underneath the ridge. As this area is large (~ 500 μm wide), this issue make the lasing condition difficult to achieve, thus increasing the required threshold current density. Also, despite the un-etched area does not contribute to the lasing action since it does not

confine the optical mode in the active region; it may also contribute negatively to the optical absorption owing to the free carriers loss in the doping area of the active region. In addition, the difficult output coupling in these design add more weakness to the performance.

Except for the 7.5 μm thick active region, the optical peak power was noticeably reduced as the thickness of the active region decreased. This may be because of the reduced number of quantum wells and higher waveguide losses in thin active regions. The performance characteristics of THz QCLs with thin etched BTC structures have also been shown, demonstrating clearly the performance reduction experienced as the etch depth is increased. However, RP structures did offer better heat extraction. Therefore, the 7.5 μm devices work best for L559 and that may be due to having the highest operating bias and better heat extraction.

Chapter 4

Self-mixing technique in a terahertz quantum cascade laser

4.1 Introduction

As previously mentioned in Chapter 1 Section 1.1, THz frequency has many imaging and sensing applications in astronomy [52], biomedical sciences [4], security screening [3], and non-destructive testing owing to the material-specific THz resonances in crystalline and polycrystalline materials and the ability to penetrate many visibly-opaque packaging materials with non-ionizing radiation [7, 19, 53]. However, THz sources are typically too large, expensive or low-powered for many applications [53]. Terahertz quantum cascade lasers (THz QCLs) are an attractive solution to be used in THz spectral range applications since these compact semiconductor sources provide a THz source that have many advantages,

such as coherence, high output power and broad spectral coverage (~ 1-5 THz) [5, 44, 53].

To benefit from such sources, THz-QCL-based sensing and imaging systems are needed. However, such systems normally implement thermal detection schemes which use helium-cooled bolometers [54], pyroelectric detectors [5], Golay cells [9] or microbolometer arrays [55]. Though, such schemes are slow and insensitive to the phase of the THz frequency range.

An alternative coherent detection scheme that can be used in a simple and compact design exploits the self-mixing (SM) effect in THz QCLs [56, 57]. In this approach, THz radiation is reflected from an external object back into the QCL cavity. The resulting interference modulates the emitted optical output power and QCL terminal voltage [56], depending on the amplitude and phase of the reflected radiation field. The laser may therefore be used simultaneously as a radiation source and a phase sensitive detector. This allows a simple, 'detector-free', self-aligned and robust system to be constructed for measuring displacement and reflectivity, all with high-sensitivity owing to its coherent nature. Also, in this system, the THz transmitter, local oscillator, mixer, and detector are all combined in a single laser [57, 58].

Advantages of the SM sensing scheme are [59-61]:

1) No optical interferometer external to the source is needed, leading to a very simple and compact setup;

2) The sensitivity of the scheme is very high owing to its homodyne (coherent) nature, potentially at the quantum noise limit (i.e. sub-nm sensitivity in path length is possible);
3) Good operation on rough diffusive surfaces can be achieved;
4) Information is carried by the laser beam and it can be picked up everywhere;
5) Offers high signal-to-noise ratio and fast acquisition, ultimately limited by the picoseconds lifetime of inter-subband transitions [62]. And as the maximum speed of response to optical feedback is determined by the frequency of relaxation oscillations in the laser, in THz QCLs, this allows response frequencies of the order of 100 GHz [58];
6) The systems offer the advantage of potential implementation into arrays.

Since the seminal work of Lang and Kobayashi in 1980 [56], SM sensors have been reported both at infrared and visible laser wavelengths [59]. However, little has been reported in the THz band with the notable exception of Green et al. [63] who used the SM technique as a means of extracting the linewidth enhancement factor of a THz QCL.

Whilst the laser SM signals are traditionally acquired from an external photo detector, SM signals of comparable quality can also be obtained by monitoring the voltage variations across the laser terminals [57].

This chapter presents the basic theory of SM in Section 4.2. Section 4.3 demonstrates the SM effect on the terminal voltage of a THz QCL by measuring the displacement of a moving target using a THz SM sensor. Section 4.4 shows the electrical and optical SM signals taken by monitoring the voltage and power variation in response to a moving remote object, and demonstrates the equivalence of these two measurement approaches. Also, in Section 4.5, owing to the high SM sensitivity, a stand-off imaging at round-trip distances of up to 21 m through air is demonstrated. And finally, three-dimensional (3D) SM imaging using QCLs is shown in Section 4.6.

4.2 Self-mixing theory

The SM effect can be modelled as a three-mirror Fabry-Perot structure [59]. This theory of the SM effect is considered in a weak optical feedback for a single mode semiconductor laser [64]. The schematic setup of the SM effect in a semiconductor laser is illustrated in Figure 4-1 [65].

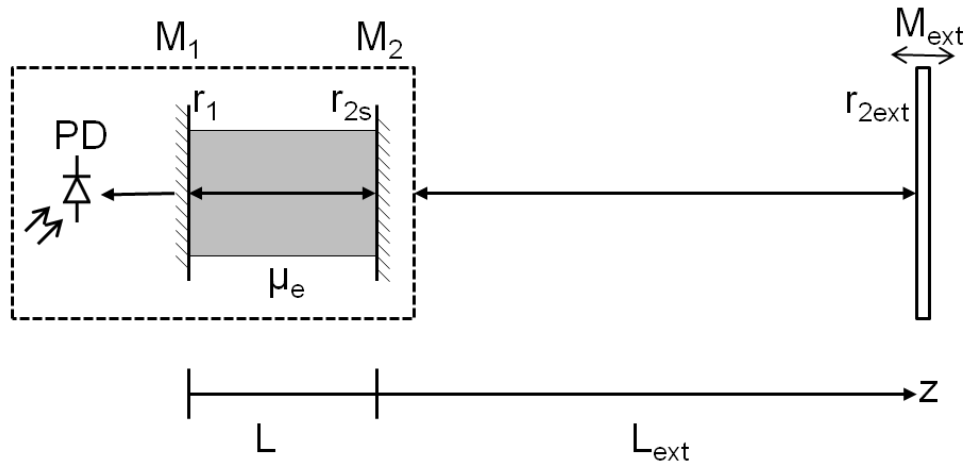

Figure 4-1: Three-mirror model and compound cavity model for SM effect in a single mode semiconductor laser, mirrors M_1 and M_2 form the laser cavity, the length of the cavity is L and which has an effective refractive index of μ_e. The external target, M_{ext}, is located on the optical axis z, at distance L_{ext}. PD is a monitor diode located in the laser package behind the laser cavity to measure power fluctuations within it.

The mirror M_2, in Figure 4-1, is replaced by an effective mirror, which combines the laser cavity and the external cavity to form a compound cavity. The amplitude reflection coefficient of the effective mirror r_2 is [65, 66]:

$$r_2(v) = r_{2s} + (1 - |r_{2s}|^2).r_{2ext}.exp^{-j2\pi v\tau_{ext}}, \tag{4-1}$$

where r_{2s} and r_{2ext} are the amplitude reflection coefficients of laser mirror M_2 and external target M_{ext}, respectively. The optical frequency is v, and τ_{ext} corresponds to the round trip delay backward and forward through the external cavity, $\tau_{ext} = 2L_{ext}/c$, where c is the speed of light and the external cavity is assumed to be air in this case [66, 67].

To have a successful operation of the laser, both the phase and the amplitude conditions must be satisfied. The phase condition states that the round trip phase of the compound cavity must be an integer multiple of 2π

$$2\beta L + \Phi_r = 2\pi m, \tag{4-2}$$

where β is the phase constant of the optical wave $(\beta = (2\pi\nu\mu_e)/c)$, m is an integer and Φ_r is the phase term of the external cavity. The amplitude condition states that the gain of the compound cavity must be larger than the cavity losses to produce leasing

$$r_1|r_2|exp^{(g_c-\alpha_s)L} = 1, \tag{4-3}$$

where g_c is the threshold gain for the compound cavity and α_s is the cavity loss factor [65, 66].

For weak feedback, the following equation for gain variation due to external feedback can be derived

$$g_c - g_{th} = -\frac{\kappa_{ext}}{L}\cos(2\pi\nu\tau_{\text{ext}}), \tag{4-4}$$

where g_{th} is the threshold gain without optical feedback. κ_{ext} is the feedback coupling coefficient to the external cavity and is indicative of the quantity of light being coupled into the laser cavity [68]. κ_{ext} varies between zero and one, and is defined as $\kappa_{ext} = (1-|r_{2s}|^2)r_{2ext}/r_{2s}$. The gain in the diode laser is produced by driving a high current density into the active area. Because external optical feedback causes gain variation, the SM phenomenon can also be measured from the pump current of the diode laser [66, 69].

In the same feedback conditions, the following equation for the laser frequency variations can be derived

$$\Delta\Phi_L = 2\pi\tau_L(\nu - \nu_{th}) + \kappa_{ext}\sqrt{1+\alpha^2}\sin(2\pi\nu\tau_{ext} + \arctan(\alpha)), \qquad (4\text{-}5)$$

where $\Delta\Phi_L$ is the round trip phase change compared to $2\pi m$, τ_L is the round trip delay in the laser cavity $(\tau_L = 2L\mu_{eg}/c)$, where μ_{eg} is the effective group refractive index, ν_{th} is the emission frequency of the laser without feedback, and α is the linewidth enhancement factor and is related to the amount of stimulated emission and it is the ratio of the real to imaginary parts of the variation in the complex refractive index [63, 70]. α is used to quantify the effect of the change of refractive index and gain with carrier density on the dynamical properties of semiconductor lasers

$$\alpha = -\frac{4\pi}{\lambda}\frac{dn/dN}{dg/dN},$$

where n is the refractive index, g is the gain per unit length, λ is the wavelength and N is the carrier density. The simultaneous variation of mode index and mode gain with injected carrier density resulted in amplitude-phase coupling that affect the laser properties, one of which is the enhancement of the laser linewidth by a factor of $(1+\alpha^2)$ [71-73].

The possible emission frequencies can be numerically solved from equation (4-5) and after calculation of ν, the gain g_c can be solved from equation (4-4) [65, 67].

Under feedback, the laser frequency shifts to provide phase-continuity of the radiation field at the laser facet. The difference between

the unperturbed frequency ν_{th} and the frequency under feedback ν is given by the phase-matching condition in equation (4-5) [53].

Depending on the phase of the feedback, the radiation field in the laser cavity is either enhanced or depleted. Correspondingly, the threshold gain of the cavity decreases or increases, and the radiative power P emitted from the laser is perturbed as:

$$P(\tau_{ext}) = P_{th}(1 + m\,cos(\nu\tau_{ext})), \tag{4-6}$$

where P_{th} is the unperturbed laser power, and m is an amplitude factor that is proportional to $\varepsilon\sqrt{r_{2ext}}$ and also called the modulation index [53, 59]. Equation (**4**-**6**) shows that the laser power changes as a function of the distance between the source and the external target (through τ_{ext}). A perturbation in the electron distribution within the laser cavity correspondingly occurs, leading to a measurable change in the device drive voltage [53, 74].

The strength of external feedback is an important consideration in SM interferometry [59]. The feedback parameter of the SM effect is defined as

$$C_{fb} = \frac{\tau_{ext}}{\tau_L}\kappa\sqrt{1 + \alpha^2}, \tag{4-7}$$

where κ is the feedback parameter which is given, for a Fabry-Perot laser, by $\kappa = \varepsilon\kappa_{ext}$, where $\varepsilon \leq 1$ is the coupling efficiency which takes into account the mode mismatch, field attenuation in the external cavity and the finite coherence length [69].

If the parameter $C_{fb} \ll 1$, power fluctuations at the laser output are sinusoidal. When C_{fb} increases; the fluctuations become more saw-tooth-like. When $C_{fb} > 1$, the operation of the laser is no longer stable, leading to increased noise and mode hopping [67, 75]. On the other hand, the saw-tooth signal can be used to detect the direction of a moving target, because the SM signal changes its inclination in respect to the phase of the external target [76]. Therefore, the C_{fb} parameter is important, because it classifies the different feedback regimes. It depends on both the amount of feedback and the target distance, L_{ext}. Feedback regimes can be divided into 4-categories [59, 64, 69, 77]

1) $C_{fb} \ll 1$ (Very weak feedback regime): The function $cos(\nu\tau_{ext})$ takes a cosine shape;
2) $0.1 < C_{fb} < 1$ (Weak feedback regime): The function $cos(\nu\tau_{ext})$ becomes slightly distorted, showing a non-symmetrical shape (see Figure 4-2 a);
3) $1 < C_{fb} < 4.6$ (Moderate feedback regime): The function $cos(\nu\tau_{ext})$ becomes saw-tooth like and exhibits hysteresis. It exhibit three-valued for certain values of the phase Φ_r, i.e. the system is bistable, with two stable states and one unstable (see Figure 4-2 b);
4) $C_{fb} > 4.6$ (Strong feedback regime): The function $cos(\nu\tau_{ext})$ may become five-valued (see Figure 4-2 c). Laser diode enters in the mode-hopping regime and interferometric measurements are no longer possible.

Figure 4-2 shows calculated shapes of the function $cos(\nu\tau_{ext})$ for three different feedback regimes [59]. The effect of external feedback strength to the shape of the interference signal with three different values of C_{fb} is shown in Figure 4-3 [64, 77]. The line in (a) shows the driving signal of the vibrating external reflector. In (b) the line shows the interference signal for $C_{fb} = 0.01$, (c) $C_{fb} = 0.7$ and (d) $C_{fb} = 3.3$. The saw-tooth effect is clearly visible, when the value of C_{fb} is changed from 0.01 to 0.7. In addition, in the case of stronger feedback the inclination change can be also detected, when the direction of the movement of the external target is changed.

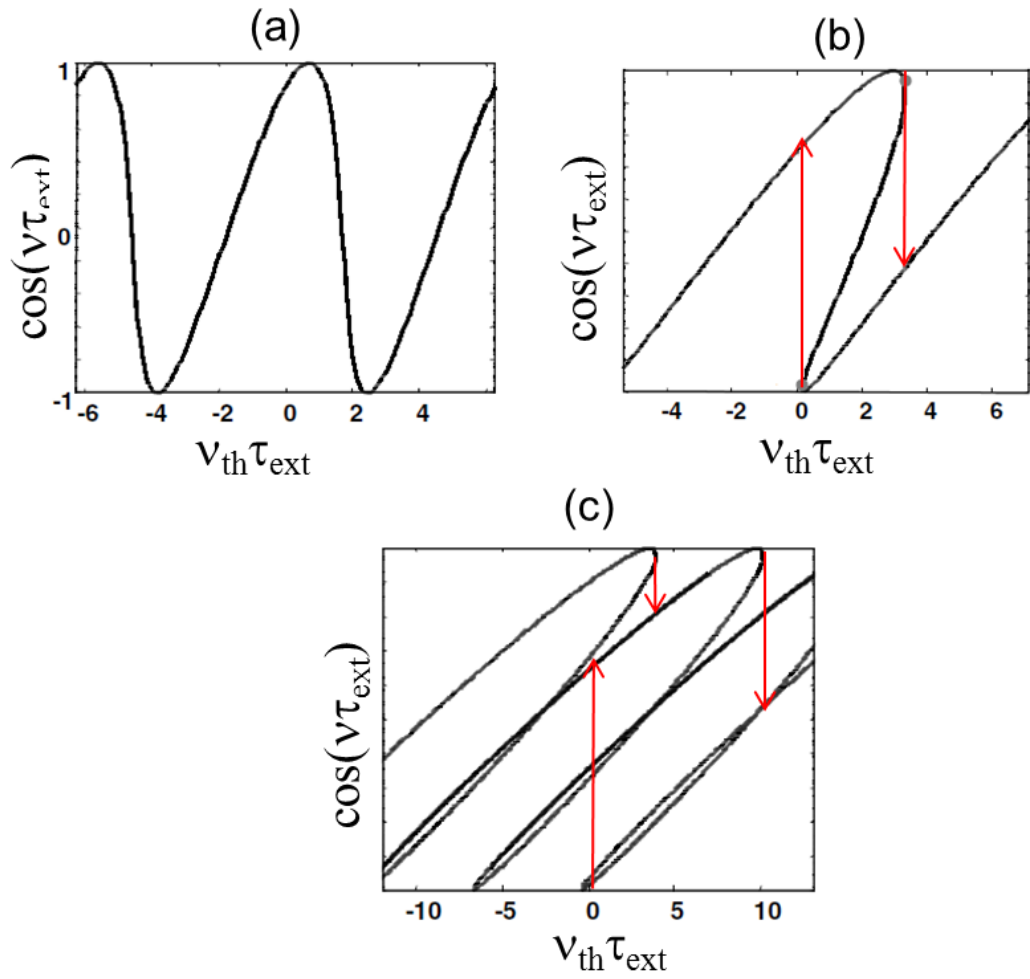

Figure 4-2: Calculated waveforms of the function cos($\nu\tau_{ext}$) for different values of the C_{fb} parameter. (a) C_{fb} = 0.7; (b) C_{fb} = 3 and (c) C_{fb} = 10 [59].

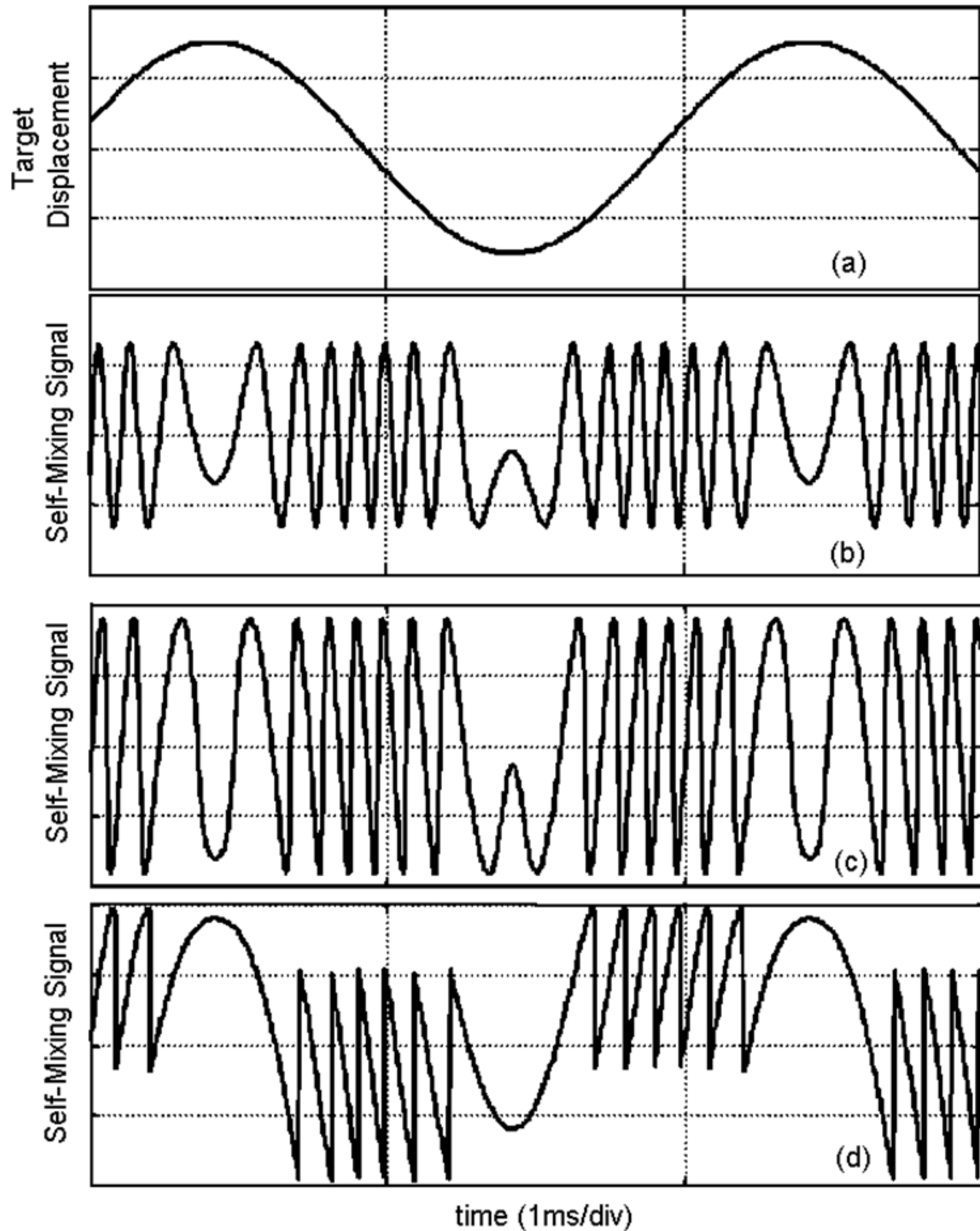

Figure 4-3: Experimental SM signal waveforms demonstrate the effect of different feedback strength on the shape of the interference signal (a) Signal driving the target; (b) SM output for C_{fb}=0.01; (c) SM output for C_{fb}=0.7; (d) SM output for C_{fb}=3.3, from [64].

Until above, the SM effect has been considered only in the case where the target remains at constant distance, L_{ext} from the front facet of

the laser diode. If the external target moves with a uniform velocity v in the positive direction along the z-axis, then τ_{ext} varies as [66]

$$\tau_{ext} = \frac{2(L_{ext} + vt)}{c}, \tag{4-8}$$

where L_{ext} is now the distance between target and laser at zero time and t denotes time. Substituting equation (4-8) into equation (4-4), power fluctuations become [67]

$$\Delta P \approx g_c - g_{th} = -\frac{\kappa_{ext}}{L} cos\left(\frac{4\pi \nu \tau v t}{c} + \frac{4\pi L_{ext} \nu}{c}\right), \tag{4-9}$$

When the target moves forward or backward, the reflected or scattered light contains a frequency shift. This shift is proportional to the velocity of the moving target, and according to the Doppler theorem, the Doppler frequency, ν_D, is [66]

$$\nu_D = \frac{2v}{\lambda}\cos(\varphi), \tag{4-10}$$

where v is the velocity of the moving target, λ is the operating wavelength of the diode laser and φ is the angle between the moving target and the laser beam. If the measurement is vertical to the target, the equation (4-10) is reduced to $\nu_D = 2v/\lambda$. Substituting this into equation (4-9) it can be seen that the power fluctuations of the laser diode are related to the Doppler frequency. Thus, it is possible to determine the velocity (the component of the velocity parallel to the laser beam) of the target by measuring these power fluctuations.

4.3 Demonstration of SM effect on the terminal voltage of a THz QCL

Initially, an experiment was set to demonstrate the SM effect on the terminal voltage of a THz QCL by measuring the displacement of a moving target using a THz SM sensor. Target displacements were measured for a range of attenuations including opaque (in the visible spectrum) materials [57].

The THz QCL used in the experiment consisted of a 10 µm thick GaAs/AlGaAs bound-to-continuum (BTC) active region [33]. The device was processed into a semi-insulating surface-plasmon (SISP) ridge waveguide with dimensions 3 mm × 140 µm and was mounted on the cold finger of a continuous flow cryostat fitted with a polythene window. The laser was operated in continuous-wave (CW) mode with a driving current of 0.9 A, and with a heat sink temperature of 25 K. It has been demonstrated that the QCL is most sensitive to optical feedback near threshold operating currents (see Figure 4-4) [58]. Similar behaviour has also been observed in junction semiconductor lasers [58, 78]. The power–current (L-I) , current–voltage (I-V), and spectral characteristics of the laser are shown in Figure 4-5 [57]. The emission spectrum shown in the inset was obtained at a drive current of 0.9 A using a Fourier-transform spectrometer (FTIR) with a spectral resolution of 7.5 GHz. The spectrum indicates emission in a single longitudinal mode at 2.6 THz.

The noise margin of this system was estimated previously in:[57] that the system could tolerate a round-trip attenuation of 45 dB, indicating a minimum detectable reflected power equal to - 4 nW [57].

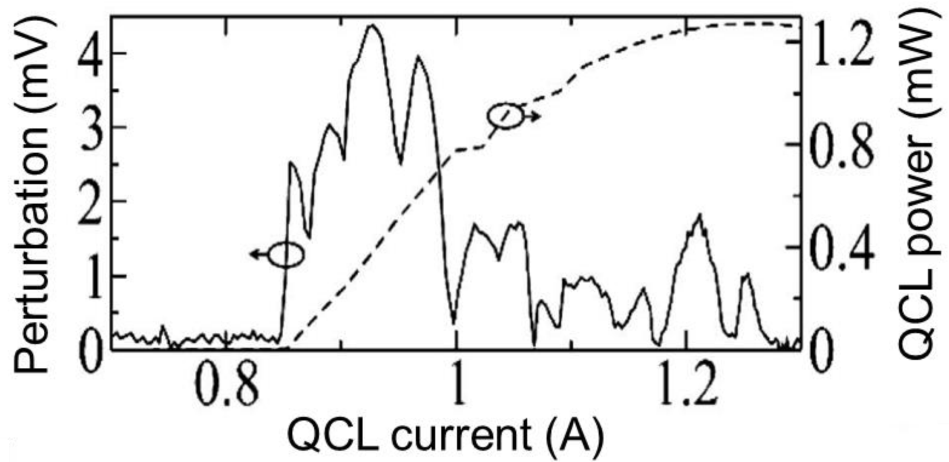

Figure 4-4: Root-mean-square SM signal (left axis) and QCL power (right axis) as a function of the QCL driving current.

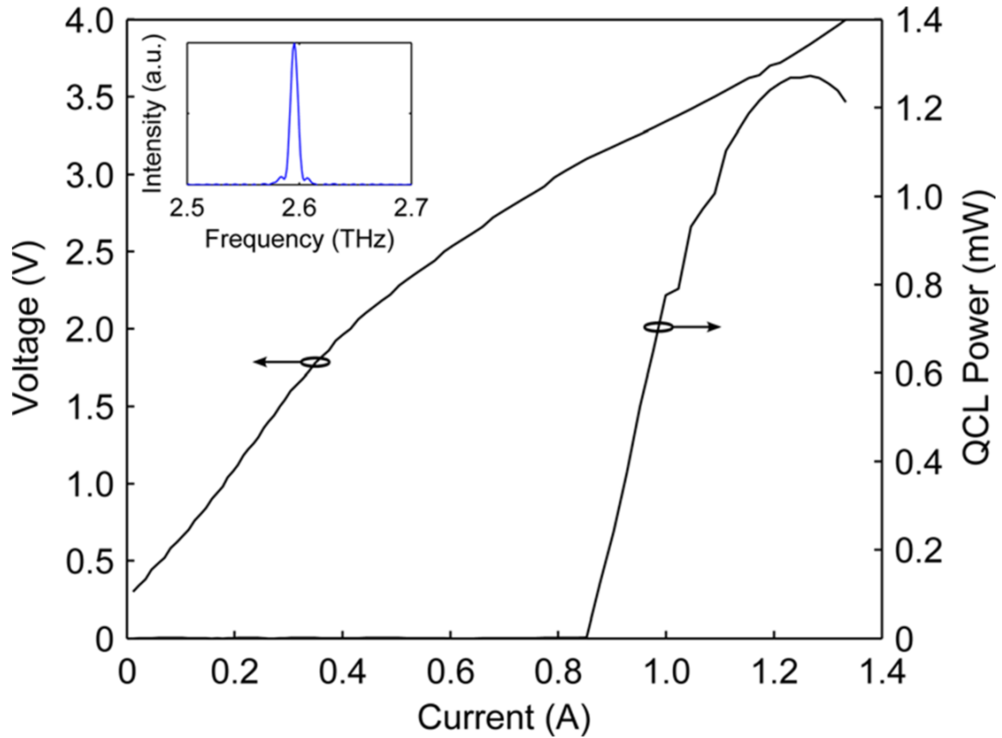

Figure 4-5: The L-I and I-V characteristics of the THz QCL used in this work. Inset: the emission spectrum of the THz QCL at a drive current of 0.9 A [57].

A schematic diagram of the experimental SM apparatus used to measure target displacement is shown in Figure 4-6 [53]. Radiation from the THz QCL was collimated using an f/2 off-axis parabolic reflector with a diameter of 2 in. and directed normally onto a vibrating target consisting of an aluminium plate that was attached to a subwoofer speaker cone. The total distance between the QCL and the target was 47 cm. In the experiments, the beam path length between the QCL and the target was varied periodically by driving the speaker with a sinusoidal voltage signal at 20 Hz. The amplitude of the target motion was adjusted to approximately 100 μm using a digital dial indicator (Mitutoyo, Model: 543-682). The SM signal was measured by monitoring the voltage variations across the terminals of the QCL, amplified by an ac-coupled amplifier with a gain of

100, and then recorded by a digital oscilloscope. No atmospheric purging was in use during the experiments. The SM signals acquired experimentally using an unobstructed beam path is shown in Figure 4-7.

To model SM signal as a function of external object displacement, the conventional three mirror SM model can be used [57, 64]. The laser phase condition with feedback can be rewritten from equation (4-5) as:

$$0 = 2\pi\tau_{ext}(\nu - \nu_{th}) + C_{fb}\, sin(2\pi\nu\tau_{ext} + arctan(\alpha)), \quad (4\text{-}11)$$

$$2\frac{(L_{ext} + \delta L_{ext})(\nu_{th} - \nu)}{c} = C_{fb}\, sin\left(2\frac{(L_{ext} + \delta L_{ext})\nu}{c} + arctan(\alpha)\right), \quad (4\text{-}12)$$

In this model, one can numerically solve this equation for the lasing frequency, ν. The change in the threshold gain relate to ν by equation (4-4), and it leads to the proportional change in terminal voltage (in the small signal approximation) [57].

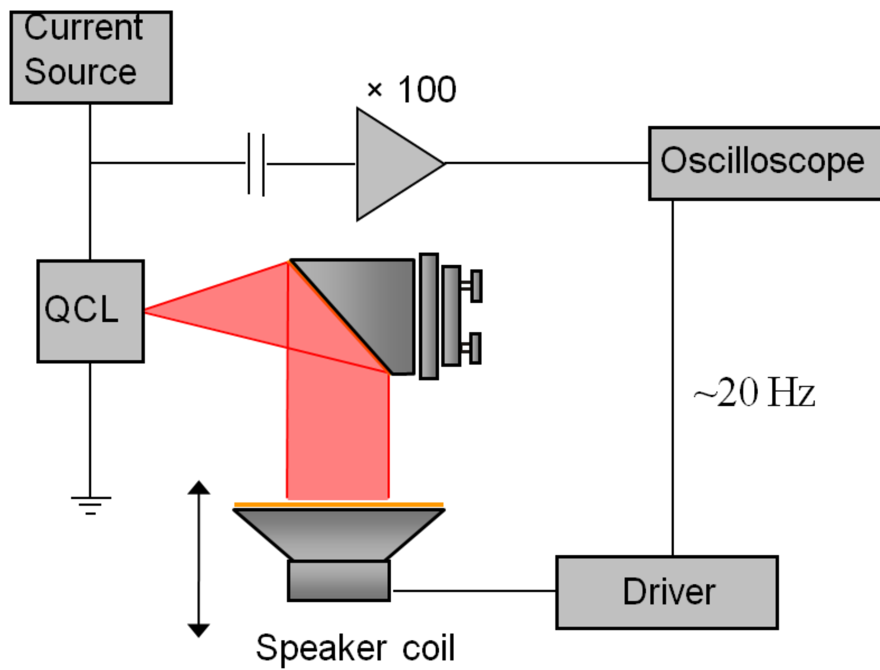

Figure 4-6: Schematic diagram of the experimental apparatus used for measuring target displacement. The QCL is driven by a constant current source and the QCL terminal voltage variations are amplified by an ac-coupled amplifier for acquisition on an oscilloscope. A parabolic mirror collimates the beam and directs it onto the remote target [53].

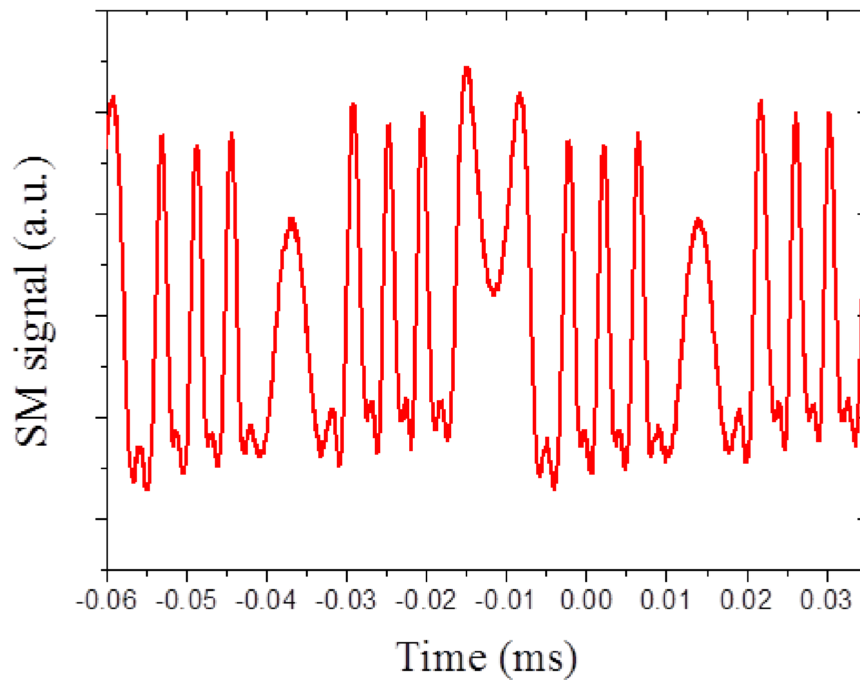

Figure 4-7: Exemplar electrical SM signals obtained in response to a moving target (the speaker). The distance between the source and the target is of 10.5 m.

In Figure 4-7, the experimental time-domain photocurrent SM signals is shown, obtained when the phase ψ of the back-reflected field is sinusoidally varied, i.e. by moving the remote target by means of a speaker. The resulting SM signal is a periodic function of ψ and a complete interferometric fringe appears each time the phase is varied by 2π. Consequently, the fringe period corresponds to a target displacement of $\lambda/2$, where λ is the free-space emission wavelength of the QCL (115 μm in this case).

4.4 Equivalence of SM-voltage and SM-power signals

At near-infrared and visible wavelengths, SM signals are typically acquired by observing fluctuations in the radiative power of the laser [59]. However, the THz-SM measurements conducted in: [58, 63] have obtained SM signals by monitoring the laser voltage. At THz frequencies, this presents many advantages over detection of the emitted power. Principally, the need for an external THz detector is removed, reducing the cost, complexity and size of the optical-system setup. The detection system may also be intrinsically faster, as it is fundamentally limited by electron transport in the QCL rather than by thermal processes in the THz detector. However, it has been shown theoretically that voltage SM signals may have a reduced signal-to-noise ratio in comparison to measurements of the radiative output power at near-infrared frequencies [79].

A radiative-power-based THz-SM sensing capability was examined in order to investigate the equivalence between SM-perturbations to the THz power and to the laser voltage. A schematic representation of the system is given in Figure 4-8 [53], with the THz emission from the back facet of the QCL being collimated and focused onto a liquid-helium cooled silicon bolometer using a pair of 3 in., 90° parabolic mirrors (f /2.4 and f/2.0 respectively). The perturbation to the detector signal was monitored on an oscilloscope using an ac-coupled ×1000 voltage amplifier.

A comparison between the two SM sensing methods was obtained by monitoring the perturbations caused by SM effect to the THz power and the terminal voltage simultaneously in response to a speaker motion with peak amplitude ≈ 150 μm (as measured with a dial gauge), and $f_s = 20$ Hz. A varying number N of 3 mm thick sheets of polytetrafluoroethylene (PTFE) were inserted midway between the QCL and the speaker in order to reduce the feedback. Figure 4-9 (a) shows that both measurement techniques produce similar SM signals, with only a slight change at the stationary points ($t = -12$ and $+14$ ms).

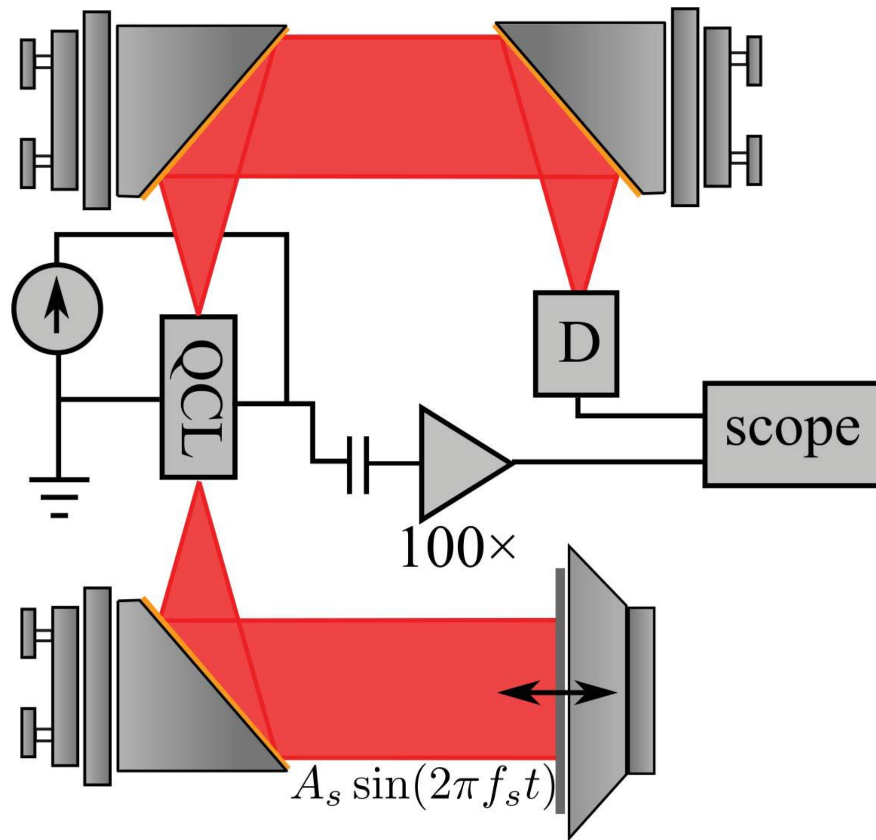

Figure 4-8: Schematic diagrams of the THz-SM sensor systems to study the equivalence of SM-voltage and SM-power signals. The QCL is driven by a dc current, and perturbations to the voltage are measured using an ac-coupled differential amplifier. A collimated THz beam is reflected by a plate attached to the cone of a subwoofer speaker, which is driven by a sinusoidal voltage. In this system, SM signals are also acquired using a helium cooled bolometer *D* to observe THz emission from the back facet. Ranges of obstructing materials (not shown in the diagram) were placed in the beam between the mirror and the target [53].

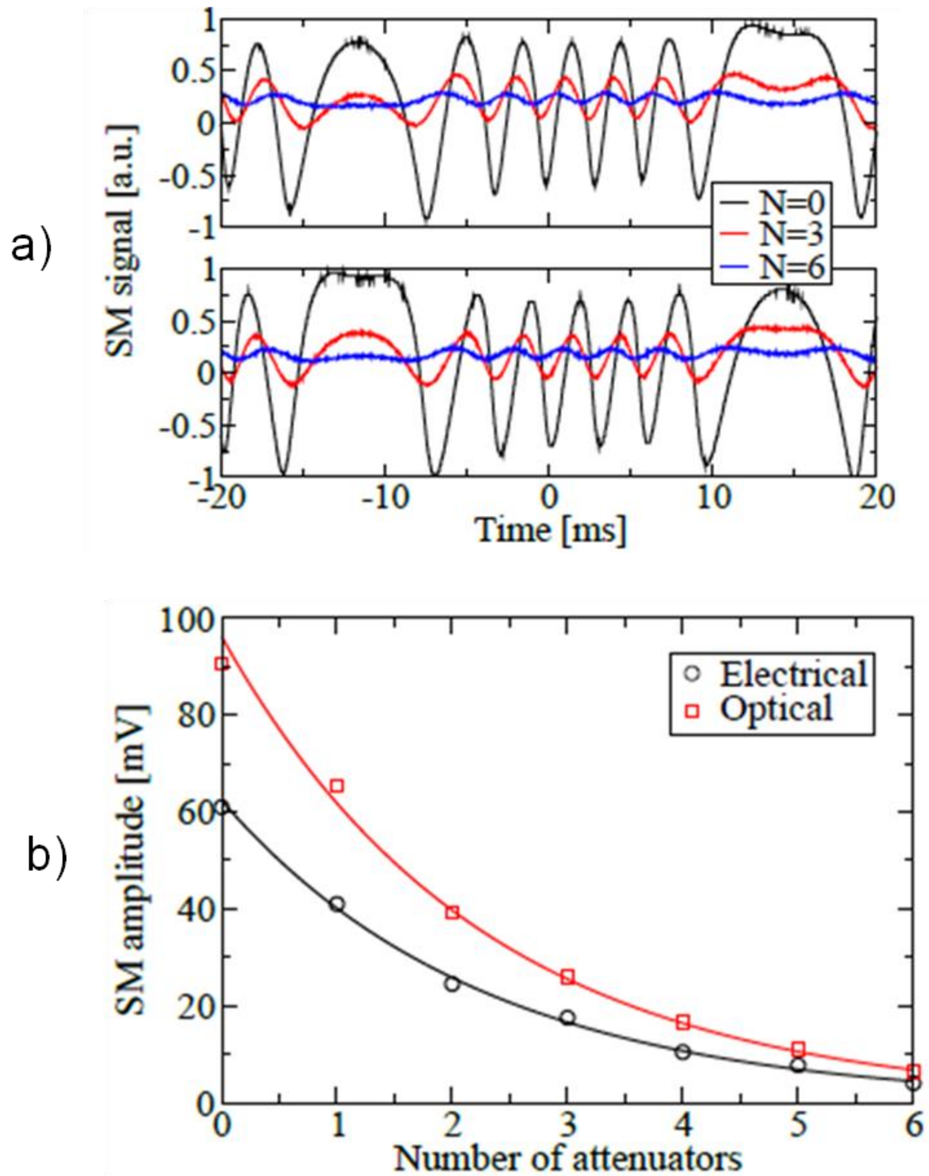

Figure 4-9: Comparisons between SM signals obtained by monitoring electrical and optical perturbations in response to 150 μm 20 Hz speaker motion. (a) Corresponding electrical and optical SM signals (upper and lower graphs, respectively), with varying numbers *N* of PTFE attenuator sheets between the QCL and the target. (b) Decay in SM signal amplitude as a function of the number of attenuators. The solid lines in each case show regressions to an exponential decay [53].

The change in the amplitude of the SM signals as the number of attenuators is increased is shown in Figure 4-9(b). It can be seen that both signal amplitudes decay exponentially with respect to the number of

attenuators, with the forms $\Delta V_{SM} \propto \exp(-0.442N)$ and $\Delta P_{SM} \propto \exp(-0.443N)$ for the electrical and optical SM signals respectively [53]. The identical exponential decay in each SM signal indicates that both methods respond equivalently to changes in the SM feedback path.

4.5 Long stand-off imaging and sensing

Phase-sensitive imaging using a THz-SM technique has previously been demonstrated [58], allowing transverse features smaller than 250 μm to be resolved without the need for any external THz detector. To date, however, THz-SM imaging has only been performed at short range, while conventional thermal (bolometric) detectors have been used at scanning ranges exceeding 25 m in air [55], by matching the laser frequency with a low-absorption atmospheric window. Here, this work shows that the high sensitivity feature of THz-SM sensing allows imaging to be conducted without any optimisation of the laser frequency at a range of 10.5 m (21 m round-trip) in air, which is the longest-range interferometric measurement with a THz QCL to date [53].

The system used for this work is shown schematically in Figure 4-10. The collimated THz beam was focused onto a sample mounted on a two-dimensional (2D) motorized translation stage, using a second 2 in., f/2, 90° parabolic mirror. This imaging system represents an intrinsically confocal configuration; in which only light reflected from the focal plane may couple efficiently back into the narrow laser aperture. Thus, the system is effectively self-aligning, and easily achieves resolutions close to

the diffraction limit (d ≈ 281 μm). The system was initially configured with a length of 50 cm between the QCL and the object, and an image of a scalpel blade was obtained by raster-scanning the stage of the objective over the focal plane. The reflected radiation was modulated at 230 Hz using an optical chopper, and the modulation amplitude of the SM voltage was acquired for each pixel of the image using a lock-in amplifier.

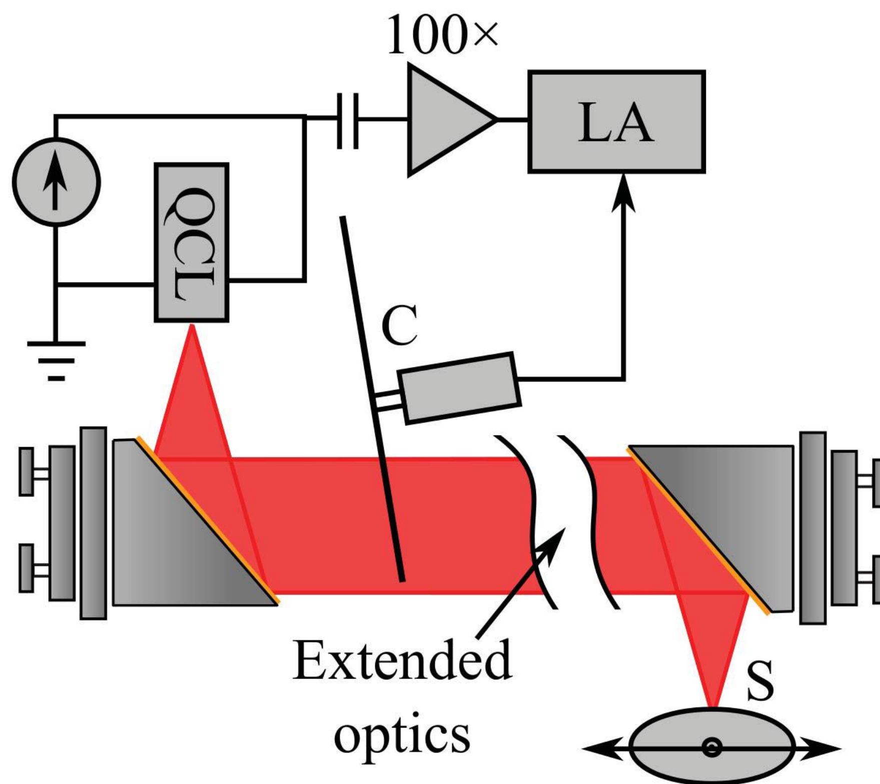

Figure 4-10: Schematic diagrams of the THz-SM sensor systems to demonstrate long range SM sensing and imaging. The QCL is driven by dc current, and perturbations to the voltage are measured using an ac-coupled differential amplifier. The THz beam is focused onto a sample on a 2-D motorized translation stage S. A set of planar mirrors (not shown) is inserted between the two parabolic mirrors in order to extend the optical path length. The feedback is modulated using an optical chopper C and the modulation-amplitude of the SM voltage signal is acquired using a lock-in amplifier LA [53].

The initial reference image was obtained using a 250 × 250 μm^2 pixel size, and is shown in Figure 4-11 (upper image). The blade can be distinguished clearly from the background, where no radiation is reflected back into the laser. Light and dark interference fringes in the image reveal variations in the surface morphology of the blade, with adjacent fringes corresponding to a longitudinal distance of half a wavelength, or ~ 58 μm in this case [53].

The optical path length between the QCL and the sample stage was then extended to 10.5 m by inserting a set of planar gold reflectors between the two parabolic mirrors. The system was aligned initially using a helium–neon laser. Fine-alignment was then achieved by inserting an oscillating reflector (as in Section 4.3) at a number of positions in the system, at progressively larger distances from the QCL, and adjusting the planar reflectors to maximize the SM voltage. Finally, an image of a scalpel blade was acquired at this range, using a 100 × 100 μm^2 pixel size as is shown in Figure 4-11 (bottom). Again, the quality of the image is sufficiently high for the blade to be distinguished clearly.

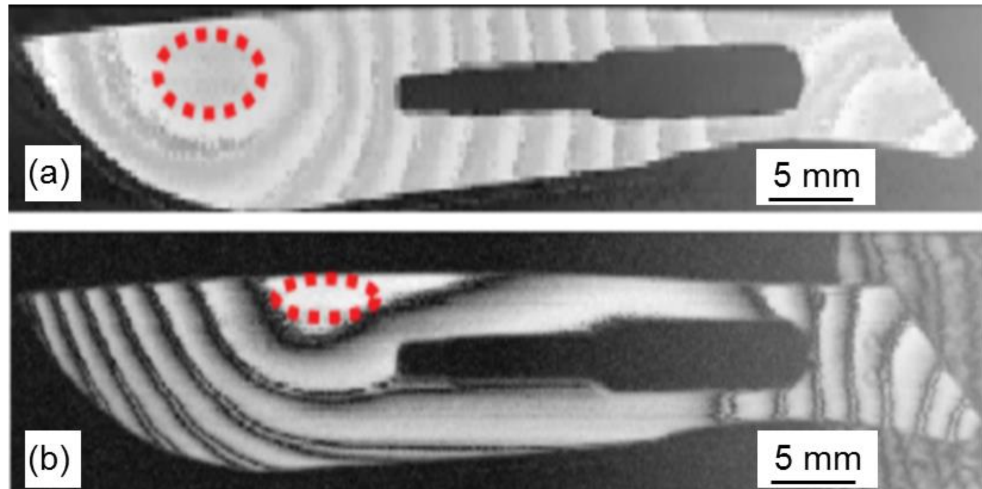

Figure 4-11: SM images of a scalpel blade at a range of (a) 50 cm and (b) 10.5 m between the QCL and the object. Pixel spacings of 250 μm and 100 μm were used, respectively. The feature at the right-hand side of the bottom image is due to reflections from the sample mount. Different blades were used for the two images. [53].

4.6 Surface-profiling through self-mixing in a THz QCL

In this work, the coherent nature of SM interferometry is exploited to demonstrate 3D profiling of exemplar structures using a THz QCL. Interferometric waveforms are acquired by monitoring the QCL voltage under feedback from the THz field which has been reflected from the surface of etched semiconductor (GaAs) samples, while the surface is scanned by a mechanical XY stage.

The imaging system used in this work was based on that described in Section 4.3. The THz QCL consisted of a 10 μm thick BTC active region emitting at ~ 2.65 THz ($\lambda \approx$ 113 μm), which was processed into a SISP ridge waveguide with dimensions 3 mm × 140 μm. The device was cooled

using a continuous flow helium cryostat and maintained at a constant temperature of 25 K. A dc power supply was used to drive the laser at a constant current of 1050 mA, just above the lasing threshold. Radiation from the laser was focused onto the sample using a pair of 2 in. diameter f/2 parabolic reflectors, with the mean distance between the laser facet and the target being $L_{ext} \approx 41$ cm through an unpurged atmosphere. The THz beam was chopped at a frequency of ~ 200 Hz and coupled back into the laser cavity along the same optical path as the incident radiation. The SM signal was observed electrically through the laser voltage using an ac-coupled differential amplifier with ×100 gain that was monitored using a lock-in amplifier synchronised to the mechanical modulation frequency. For imaging acquisition, the sample was raster-scanned in two-dimensions, vertical to the THz beam, using computer-controlled translation stages. In addition, the sample was mounted on a third translation stage allowing longitudinal scanning of the sample along the beam path (z-axis) at each transverse position [80].

Initially, high-resolution 2D images of conic samples fabricated from PTFE were obtained to demonstrate the surface-profiling capability of the SM technique. Figure 4-12 shows an image of a 2 in. diameter cone with an angle of elevation of 4.6° ± 0.4°, measured using a calliper. The image was produced by plotting the magnitude of the lock-in signal. In this case, a pixel size of 100 μm was used and no longitudinal scanning of the sample was undertaken. Concentric fringes corresponding to a λ/2 = 57 μm change in depth are clearly visible.

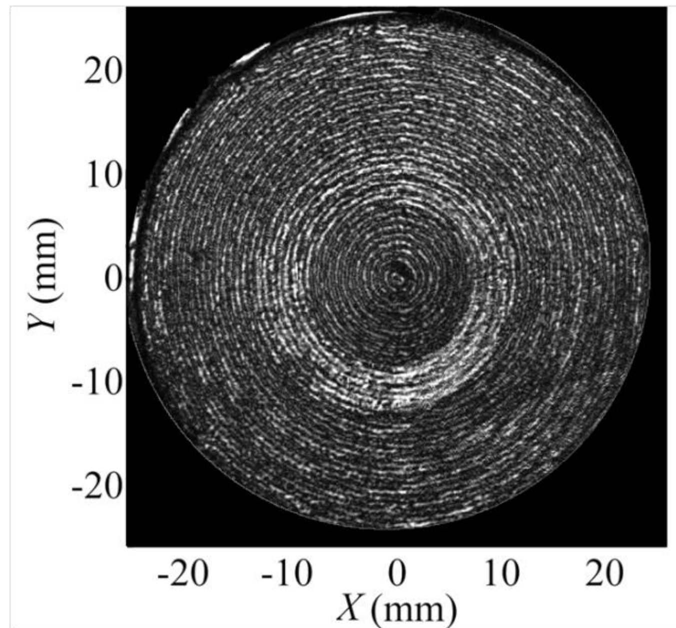

Figure 4-12: THz SM image of a PTFE cone with an angle of elevation of 4.6º ± 0.4º, showing concentric fringes arising from the slope of the cone surface [80].

Coherent 3D imaging was performed on exemplar GaAs structures that were fabricated by wet chemical etching. Figure 4-13 shows 2D and 3D images of the sample comprised of five stepped regions (in the X-direction) with a nominal step height ~ 5 µm and a width (in the Y-direction) of ~ 1.2 mm. The upper half of each structure was also coated with a ~ 125 nm thick layer of gold in order to provide regions of differing reflectance. For coherent image acquisition, the sample was scanned on a pixel-by-pixel basis through a longitudinal (z) distance of 0.5 mm, corresponding to nine interferometric fringes. The use of a high sampling resolution of 0.5 µm, corresponding to 1/100 of a fringe, allowed the shape of the fringes to be measured accurately. With a lock-in time constant of 10 ms, the resulting acquisition rate was 20 s/pixel.

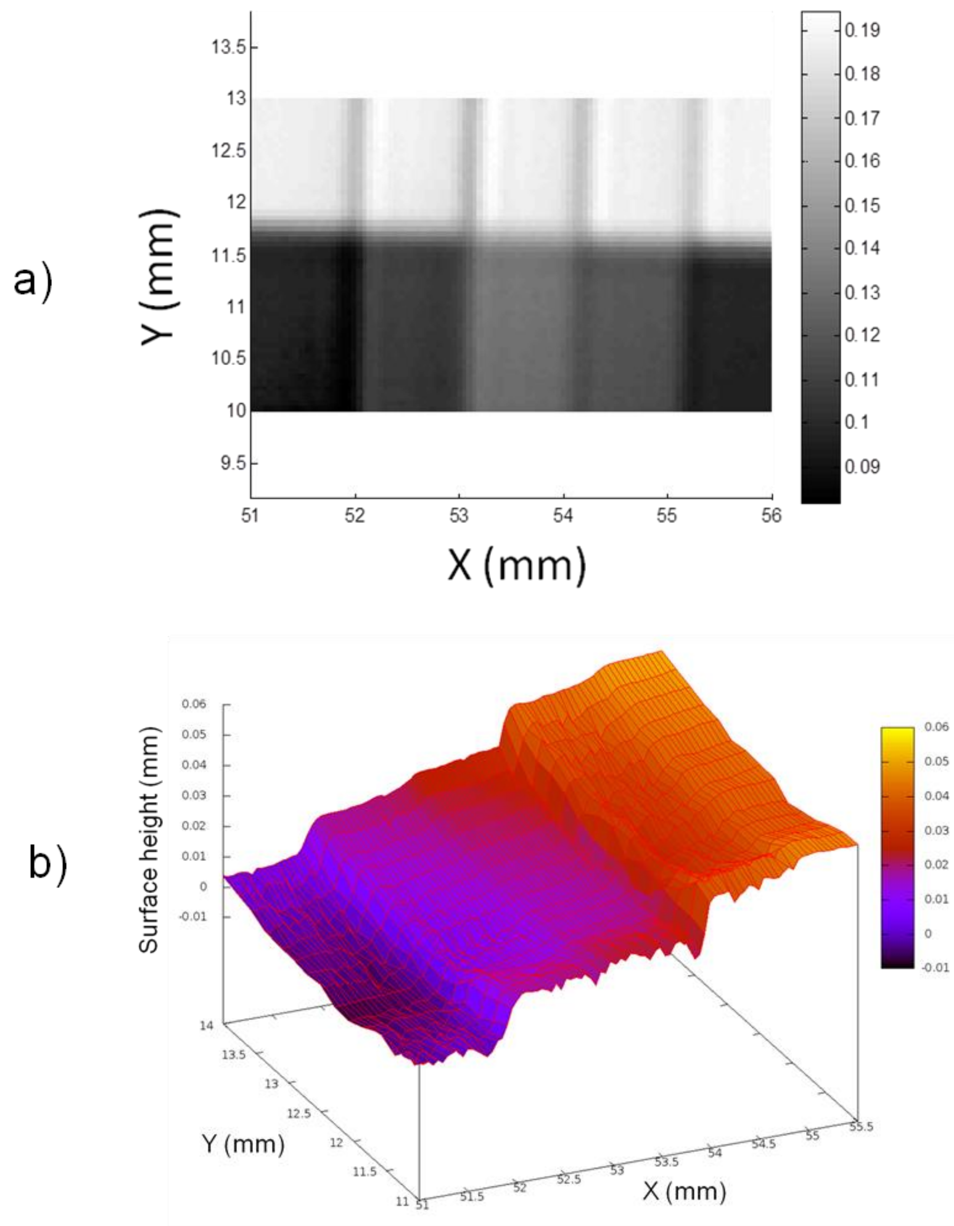

Figure 4-13: a) 2D and b) 3D, THz SM image of a stepped GaAs sample with 50 cm between the sample and the QCL. The top region in each image corresponds to the gold-coated region of the sample.

4.7 Conclusion

In summary, this chapter demonstrated sensing and imaging systems that exploit THz SM interferometry, in which a single THz QCL is employed as both the radiation source and detector. The experiments of using a “detector-less” sensor system in which the SM signal is monitored through the QCL drive voltage were shown. This technique is well-suited to fast, high-resolution, high sensitivity imaging at THz frequencies without the need for an external THz detector. Applications of this technique could include monitoring the motion of visibly concealed instrumentation.

It was also verified that these measurements are equivalent to those obtained using a more conventional optical SM technique, and that both methods are capable of determining the THz absorption coefficient of samples in the beam path. This method could readily be applied to the development of compact systems for a broad range of applications including high resolution gas spectroscopy using a tunable QCL.

The high-resolution THz-SM imaging over an extended distance of 10.5m between the QCL and an object was demonstrated.

Finally, the experiments to show that this technique allows both the depth and reflectance to be mapped across the surface of structures were presented.

Subsequently, the outstanding results presented in this chapter has led to publications in two journal papers; in Sensors Journal, IEEE [53] and Applied Physics Letters [80].

Chapter 5

Terahertz quantum cascade lasers with surface acoustic waves

5.1 Introduction

Reliable, repeatable and widely tunable single-frequency terahertz quantum cascade lasers (THz QCLs) are highly desired for imaging and sensing applications [44, 81]. QCL in its typical geometry is a simple free-running Fabry–Perot laser that implements the two cleaved facets of the semiconductor crystal as cavity mirrors. This causes the laser to emit on multiple longitudinal modes [81].

There are different approaches to achieve single and stable modes of THz QCLs. Some of these solutions are distributed feedback (DFB) resonators, macroscopic external cavities, miniaturized vertical cavities and opto-mechanical coupling systems to manipulate the lasing mode [81].

Currently it is only possible to tune THz QCLs over a frequency range of ~ 100 GHz, which is achieved by using an external silicon or metallic plunger in front of the THz QCL [82], or by changing the applied electric voltage across the device [83]. External cavity QCLs tuned by variation of the cavity length. The tunability of the feedback is provided by the inserting of a controllable optical elements or a simple movable mirror. This approach provides tuning up to 3 cm^{-1} [84].

As a consequence of this unmet requirement, a large number of researchers are engaged in developing techniques to tune THz QCLs. In particular, it has been suggested that QCLs can be tuned by using surface acoustic waves (SAWs), which could provide a widely tunable single mode laser emission [42, 45]. The SAW device would be monolithically integrated with the QCLs so that the acoustic waves propagate through the optical axis (see Figure 5-1). This will produce a periodic modulation of the carrier density and the optical gain, which is enough to provide a DFB effect [42]. Since the wavelength of SAWs can be readily changed, the frequency of the main DFB mode of the laser could be tuned through a broad range [42].

In order to achieve modulation of QCL THz emission by SAWs, it is essential to have good coupling between the SAW devices and the active region of the laser. To fulfill this condition, angled-facet QCLs, described in Chapter 2, were fabricated. The need for an etched facet of a THz QCL is to overcome the challenge of coupling SAWs up the facet and into the upper single metal (SM) waveguide of the laser. Otherwise, the 10 μm

mesa step, existing at the cleaved facet of a traditional THz QCL, will reflect back the incident SAWs.

For the aim of modeling QCL output emission via SAWs; interdigitated-transducers (IDTs) were monolithically processed with THz QCLs on a piezoelectric GaAs chip.

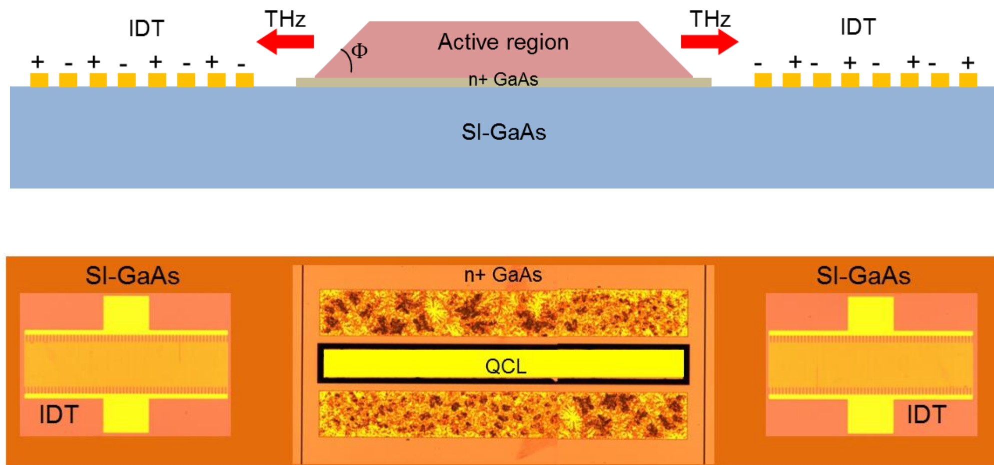

Figure 5-1: Two schematic diagrams with top microscope images showing a THz QCL integrated with SAW transducers. Figure not to scale.

This chapter will look at the possibilities of laser modulation using both travelling and standing surface acoustic wave configurations. In Section 5.2, the underpinning theory for integrating SAWs with a THz QCL will be discussed. Then, in Section 5.3, the information about the device parameters will be given. Sections 5.4 and 5.5 will describe the IDT characterisation on bulk GaAs and GaAs sputtered with Zinc oxide (ZnO), respectively. Integrating IDTs with THz QCLs is described in Section 5.6. This chapter concludes with suggestions for improvement on the work described in this Thesis, which are presented in Section 5.7 and expanded upon in Chapter 6.

5.2 Theory

5.2.1 Surface acoustic waves

SAWs are defined as waves which travel along the surface of a solid, and were first discovered by Lord Rayleigh in 1885 [85]. In the present day, SAW devices are implemented in mobile and wireless communication and signal processing applications [86, 87]. SAWs are typically generated and received by using IDTs, which are made up of a number of metallic "finger" electrodes on a piezoelectric substrate (see Figure 5-1 and Figure 5-2). All the electrodes on the same side share the same bus bar, and the wavelength of the SAWs can be adjusted by altering the dimension of the IDT. Ideally, IDTs are processed on materials with high piezoelectric coefficients, such as silicon dioxide (SiO_2) and lithium niobate ($LiNbO_3$) [87]. GaAs, however, also can be used as a substrate for IDTs, despite being a weak piezoelectric semiconductor material where both the coupling coefficient and velocity ($v = \sim 2.8 \times 10^3$ m/s) are relatively low.

A periodic electric field is created from the IDTs by applying a potential voltage across the two isolated IDT elements. For a piezoelectric material, strain will then occur in the substrate. A so-configured IDT will operate as an emitter. The emitter converts the energy applied in the electric field across the piezoelectric material into a mechanical wave generated within it. The condition of this conversion is that the frequency of the applied time-varying voltage satisfies the relation [88]:

$$\lambda_{SAW} = \frac{\nu_{SAW}}{f_{\circ}}, \tag{5-1}$$

where λ_{SAW} is the SAW wavelength, and is defined as the distance between two adjacent fingers. ν_{SAW} and $f_{\circ}$ are the SAW velocity and the detection frequency respectively. A second IDT, which is utilised as a receiver, can then convert the resulting mechanical wave applied across the IDT elements, back into an electrical signal [87].

Figure 5-2 demonstrates IDT operation. By applying an electric voltage on one of the IDT “transmitter”, the electric field lines, which go through the crystal in the sections between the multiple fingers, induce mechanical stresses in the substrate due to the piezoelectric effect (Figure 5-2 a). These stresses in turn initial a SAW that travels along the crystal as a mechanical wave (Figure 5-2 b). Other waves may also be created – such as bulk acoustic waves. The transmission medium should be set up such that SAWs are allowed to propagate and other waves are inhibited. This aforementioned mechanical wave is then detected by a second IDT that act, as a receiver, and converts the mechanical wave into an electrical signal (Figure 5-2 c) [88].

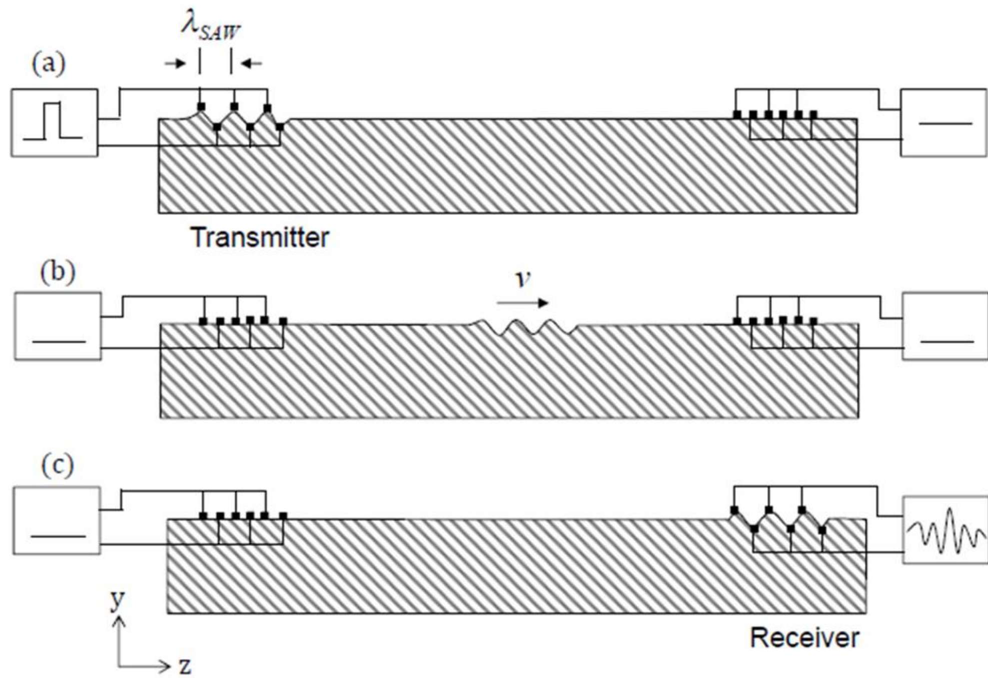

Figure 5-2: Demonstration of the IDT operation: (a) an electrical field is applied to the transmitter IDT, (b) a SAW travels across the crystal towards the second IDT and (c) the travelling mechanical wave is collected by the receiver IDT and converted back to an electrical signal. λ_{SAW} is SAW wavelength and ν is SAW velocity [88].

Assuming that the width of fingers and the space between them are all equal, the SAWs created from parallel metallic fingers will be in phase and can be added together in amplitude. This means that the finger width will be one fourth of λ_{SAW}.

The velocity ν and the electromechanical coupling constant K^2 can be defined as [89, 90]:

$$\nu = \sqrt{c'/\rho}\,, \tag{5-2}$$

$$K^2 = \frac{(\mathrm{e^S})^2}{\mathrm{c^E}\epsilon}\,, \tag{5-3}$$

where c', ρ, e^S, c^E and ϵ are the elastic constant, mass density, piezoelectric stress constant, stiffness at constant electric field and permittivity of the medium at constant stress (dielectric constant), respectively. Equation (5-3) shows that K^2 does not account for dielectric or mechanical losses [89, 90].

Although GaAs is considered to be a weak piezoelectric material (small K^2) when compared to other materials, it has been shown in the literature [91-96] that interactions between SAWs and GaAs can occur. A direct current induced by SAW through a quantum point contact defined in a GaAs–AlGaAs two-dimensional electron gas (2DEG) by means of a split gate is demonstrated in [92, 93]. The effect of perpendicular magnetic field on the quantized acoustoelectric current in a one-dimensional channel observed using a shallow-etched channel SAW device [95]. In [96] a measurement of acoustoelectric current flow in two submicron-separated quantum wires formed in an AlGaAs/GaAs heterostructure.

For a (100) GaAs substrate and a (110) SAW axis, the SAW velocity is ~ 2841 m/s and K^2 = 0.06 % [86].

5.2.2 Interaction of surface acoustic waves with laser active region

To understand the interactive effect of SAWs on the laser cavity performance, one needs to consider the acoustic induced distributed feedback (ADFB) [90, 97, 98].

Figure 5-3 demonstrates how a laser cavity can be achieved using a DFB in periodic structures [97]. In the figure, two waves are travelling in opposite directions along the laser cavity. The energy of the waves can transfer between them during the propagation due to Bragg scattering. This leads to changes in the spectrum due to the periodicity and strength of the perturbation. A coupled wave theory can be used to represent the above. The scalar wave equation for electric field can be written as [97]:

$$\frac{\partial^2}{\partial \mathrm{z}^2} E_a + \kappa_\mathrm{p}^2 E_a = 0 \tag{5-4}$$

where z the direction of propagation, E_a is the complex amplitude of a field of angular frequency ω and κ_p is the propagation constant of the wave.

The modulation of the refractive index $n_{eff(z)}$ and the waveguide losses can be defined as:

$$n_{eff(z)} = n_{eff} + \Delta n_{eff} \cos(\mathrm{z}), \tag{5-5}$$

where n_{eff} is the effective refractive index of the waveguide.

The coupling constant κ_c of travelling waves along both negative and positive directions of z, can be expressed as [90]:

$$\kappa_c = \frac{\pi \Delta n_{eff}}{4 n_{eff} \Lambda} + i \frac{\Delta a_w + g_{th} \Delta \Gamma}{2}, \tag{5-6}$$

where Λ is the periodic modulation, g_{th} is the gain of the material at threshold, Δa_w the modulation of the waveguide loss and $\Delta \Gamma$ the modulation of the confinement factor of the waveguide.

In order to obtain single mode emission using DFB, periodic modulation of a QCL active region in needed. This has been demonstrated using lithography patterning structure [99]. But, in this work, it is proposed to use SAWs to control the laser frequency.

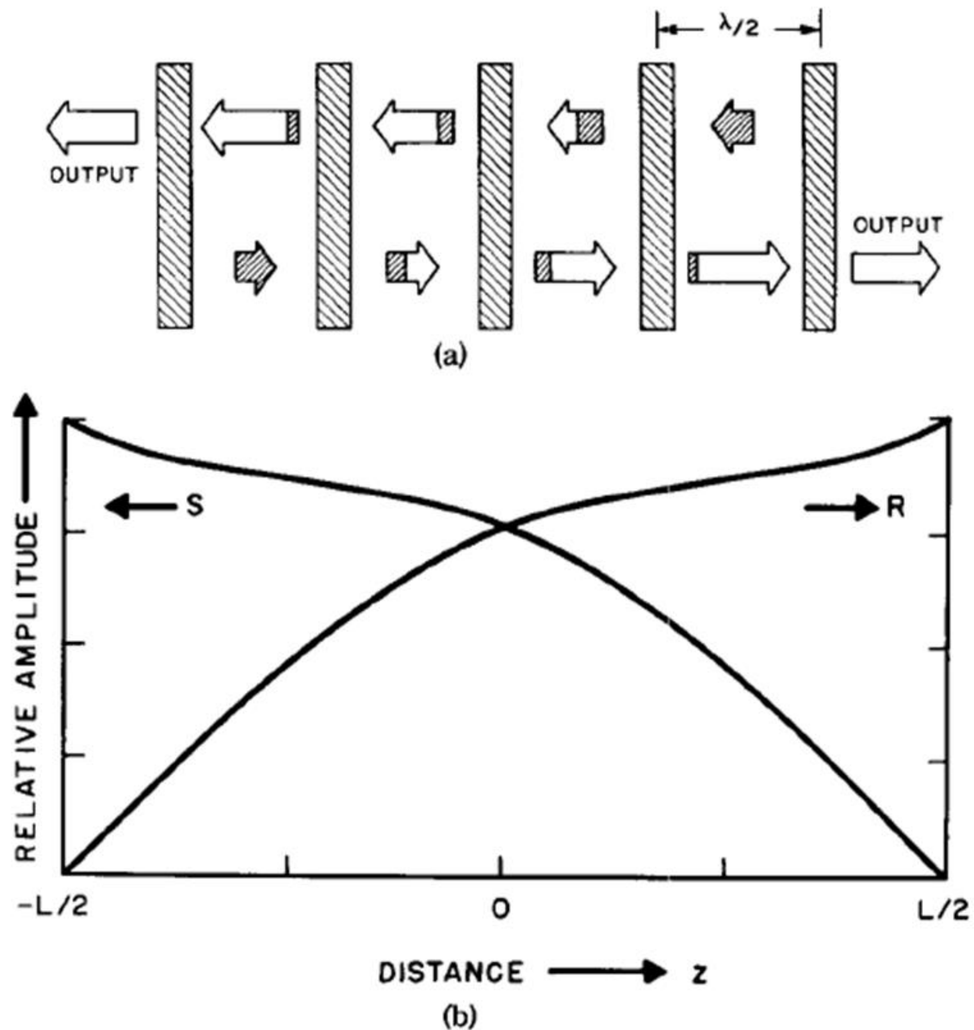

Figure 5-3: (a) Illustration demonstrating laser oscillation in a periodic structure. (b) Plot of the amplitudes of left traveling wave (S) and right traveling wave (R) versus distance [97].

The following relation shows the variation of the refractive index induced by SAWs [98]:

$$\Delta\left(\frac{1}{n^2}\right) = \rho_{IJ} S_J, \tag{5-7}$$

where ρ_{IJ} is the photo-elastic tensor of the material and is related to the piezoelectric properties of the material and S_J is the strain tensor.

As in [90], the optical interaction between SAWs and the QCL is weak as a result of the limited modulation depth which is about one wavelength of the SAW. For a SAW with power of 20 dBm, the value of $\Delta n_{eff}/n_{eff}$ is calculated to be 8.7×10^{-4} , which results in a coupling constant κ_c value equal to 0.046, which is lower than a conventional DFB. This inevitably will make SAW-induced modulation of QCL output difficult to obtain experimentally.

5.3 Device parameters

Two different SAW wavelengths were investigated in this work for modulating the emission for THz QCLs. They were chosen based on the work on [100] where a focused ion beam (FIB) was used to introduce periodic etched regions into a QCL laser cavity. These two wavelength were ~ 187 MHz (λ = 15 μm) and ~ 224 MHz (λ = 12.5 μm). The widths of the fingers and the gaps, required for this investigation, were 3.75 μm and 3.125 μm respectively. To maximize the coupling between the SAW and QCL, 60 metallic fingers were used and fabricated to be the same width to the laser ridge which is 200 μm. The fingers were made from Ti/Au with ~ 20/ 100 nm thickness (see Figure 5-4).

Four different THz QCLs were implemented: L500, L514, L645 and L654 (growth details tabulated in Appendix A) each of which operated at ~ 3.1 THz. The lasers were based on the a 10 μm thick, three-well resonant phonon (RP) depopulation active region design [51]. The fabrication details for both the QCLs and the IDTs are presented in Chapter 2.

The THz QCLs were 1.6 mm long, 200 μm wide and 10 μm active region thickness. This geometry gives best performances for etched facet devices based on work concluded by M. Salih [41] and lasers were processed with an angled facet of Φ ~ 42° to minimize the SAW loss. Five set of experiments were undertaken with IDTs:

1) The IDTs were first fabricated on SI-GaAs to demonstrate the SAW propagation.
2) The effect of mesa height on SAW propagation was studied for a range of thicknesses. Both SI-GaAs chips and un-processed THz QCLs structures were used.
3) SAW propagation was tested through etched facets in SI-GaAs.
4) Thin (~ 200 μm) ZnO layer was then deposited on SI-GaAs before patterning the IDTs in order to improve the coupling strength.
5) The IDTs were fabricated on both sides of the etched facet on THz QCL samples. In this work, the bottom n^+ GaAs layer was removed by etching to minimize the SAW losses during the travel from IDT along to the QCL ridge.

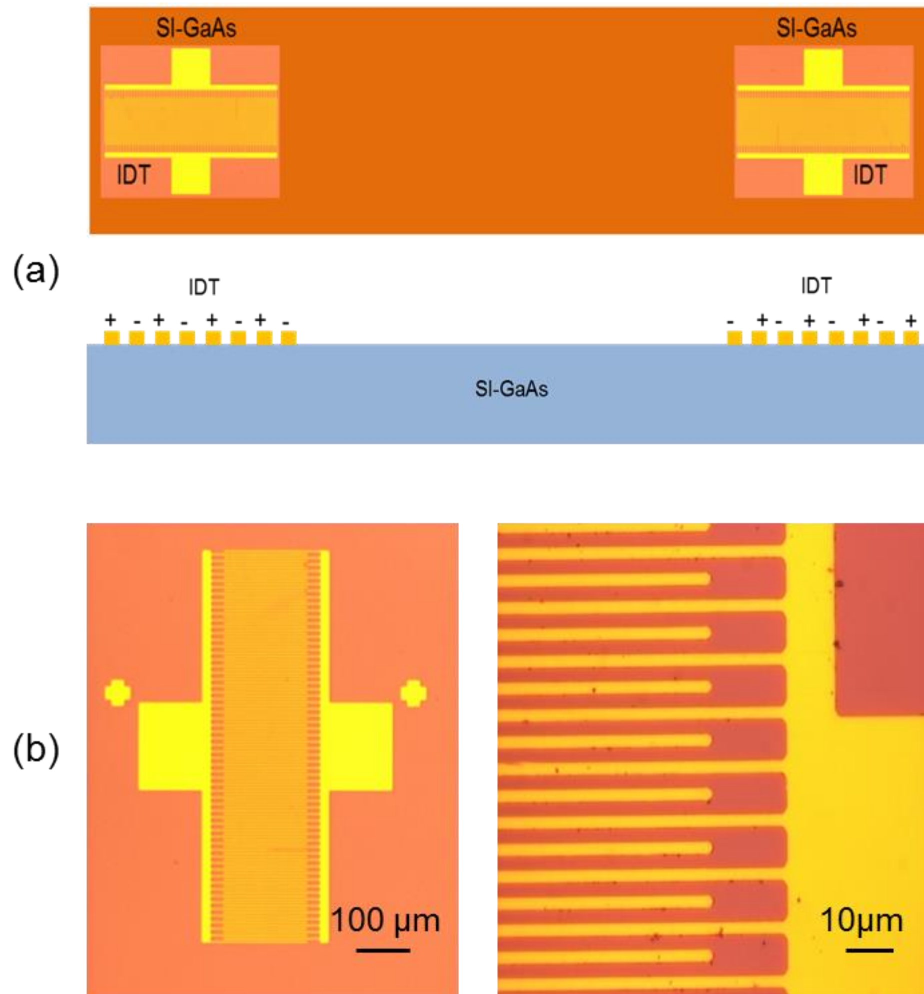

Figure 5-4: (a) Two schematic diagrams and (b) two top microscope images of IDTs fabricated on a SI-GaAs chip. Figure (a) not to scale.

5.4 IDTs characterisation on bulk GaAs

In order to demonstrate the propagation of SAWs on SI-GaAs, IDTs were first fabricated on a bulk GaAs wafer. The measured scattering parameters (S-parameters) that quantify the propagation of SAWs energy between the transmitter and the receiver transducers, taken by a network analyzer, are presented in Figure 5-5. The IDTs were connected to the network analyzer via SMA connectors. S11 and S22 measurements

indicate the signal reflected at port 1 and port 2 respectively. While S21 refers to the response at port 2 due to a signal at port 1, and S12 the response at port 1 due to a signal at port 2. These measurements were taken at room temperature. Although 50 Ω matching was not implemented in this work, a response was detected at ~ 187 MHz (Figure 5-5) and ~ 224 MHz as designed. At ~ 187 MHz response, the transmission values (S12 and S21) were ~ - 35 dB and the reflection (S11 and S22) were ~ - 0.5 dB (see Figure 5-5). The power injected into IDTs by network analyser was 0 dBm.

The very high SAW reflection, suggested by S11 and S22 in Figure 5-5, means that little power was transmitted from one port to the other. This can be attributed to the large characteristic impedance mis-match, and could be overcome through the application of an appropriate matching circuit. Nevertheless, Figure 5-5 demonstrated successful SAW fabrication and operation.

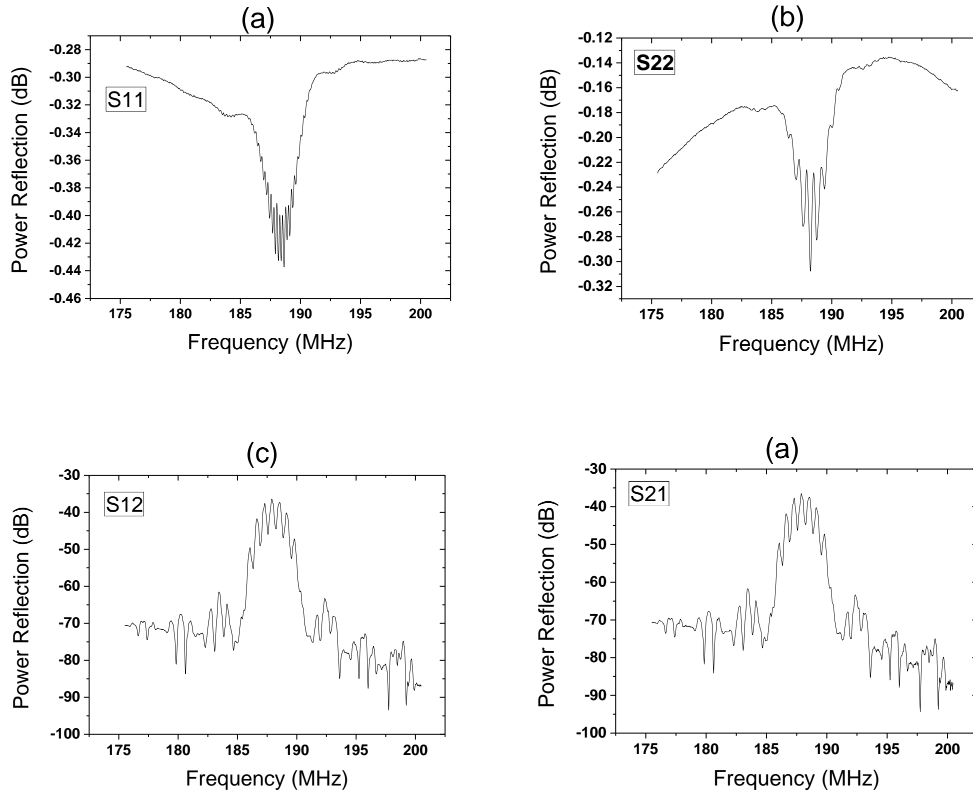

Figure 5-5: S parameters configurations measured by a network analyser generating SAWs at 187 MHz (a) S11, (b) S22, (c) S12 and (d) S21.

As THz QCLs are working in cryogenic environments, it was also important to qualify the SAW performance under the same operating conditions. Under a 10 K ambient temperature, the frequency peak of S12 and S21 was observed to undergo a shift from ~187 to ~189 MHz. This can be attributed to the change of velocity between the metallic IDTs fingers as a result of the change in the temperature.

As GaAs is a weak piezoelectric material, a weak SAW propagation was observed as a result of the high loss during the transmission. While S12 and S21 in this work were measured to be ~ -35 dB, the ideal value is expected to be higher than -7 dB.

5.4.1 IDTs characterisation on GaAs with different mesa height

In order to investigate the effect of the mesa height between the two IDTs on the SAW performance, twenty devices with different mesa configurations were fabricated using bulk SI-GaAs wafers (see Figure 5-6). Also, four more devices were fabricated using THz QCL structures to study the QCL doping effect on the SAW propagation. The sample details are presented in Table 5-1.

material	Mesa height (μm)	No. of devices
SI-GaAs	No mesa	4
SI-GaAs	5	4
SI-GaAs	7.5	4
SI-GaAs	8.7	4
SI-GaAs	10	4
THz QCL	10	4

Table 5-1: Summary of 24 devices fabricated to study the effect of the mesa height and doping on SAW transmission.

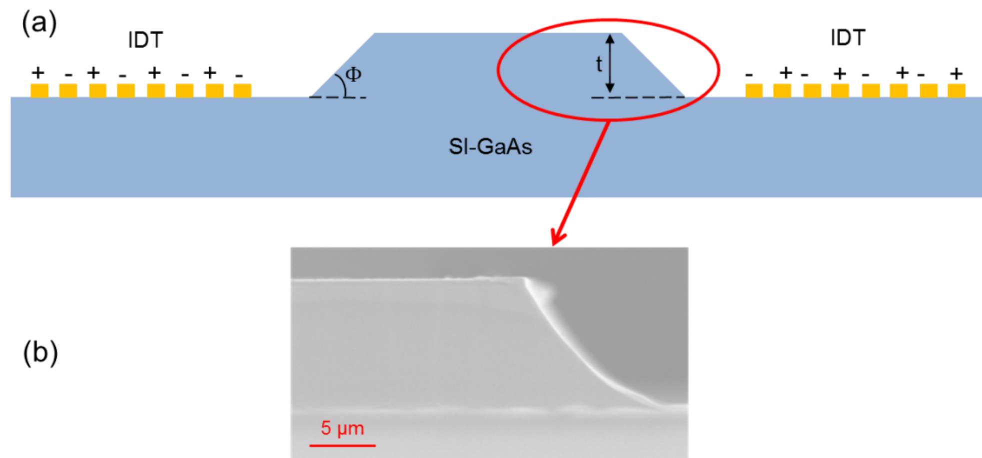

Figure 5-6: (a) Schematic diagram and (b) Scanning electron micrograph (SEM) of IDTs fabricated on a SI-GaAs with mesa of height (t) between the two IDTs. Φ is the mesa sloped angle. Courtesy of [41]. Figure (a) not to scale.

In all the devices, the SAW frequency was 187 MHz. The mesa was 1.6 mm long and 200 μm wide. To simplify the fabrication, all the mesa were defined by etching using same etching solution concentration (H_2SO_4:H_2O_2:H_2O / 1:8:950 in ratio). Thus, the mesa angles for each etch depth did not largely differ. For the 10 μm mesa, the angle was $\Phi \sim 42^0$. The power injected to the IDTs was 0 dBm and the test was conducted at room temperature. Figure 5-7 shows the S11 and S22 measurements for all devices, whereas Figure 5-8 shows the S12 and S21 measurements.

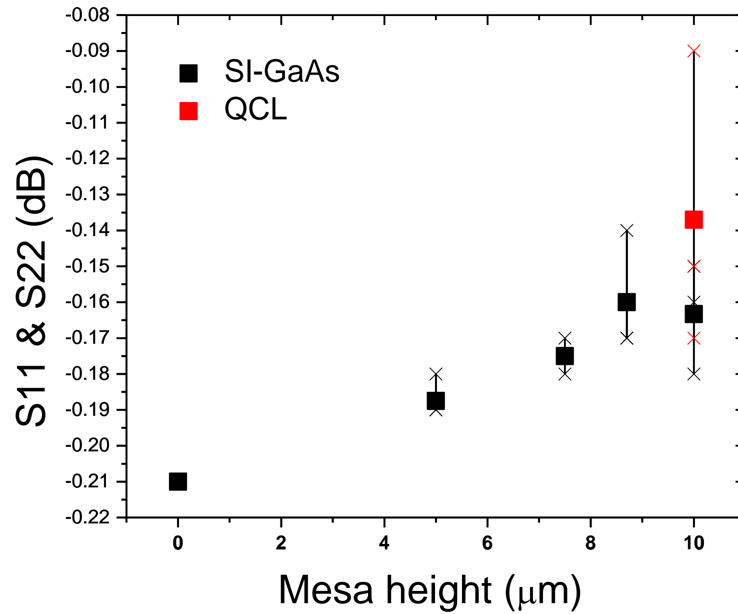

Figure 5-7: Summary of S11 and S22 measurements of the 24 devices tested to study the effect of the mesa height and doping on the performance of SAW transmission.

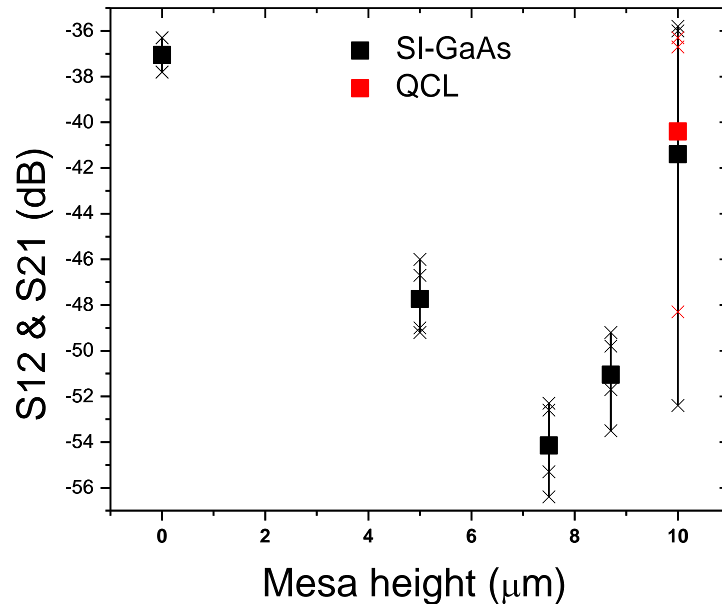

Figure 5-8: Summary of S12 and S21 measurements of 24 devices tested to study the effect of the mesa height and doping on the performance of SAW transmission.

From Figure 5-7, it can be seen that as the mesa height increase, so does the reflected power. This is as expected because there is a great difficulty to the propagating SAWs for increased mesa height. For Figure 5-8, a clear trend can be observed in the relation between mesa height and the SAW propagation along the devices. The minimum in S21 and S12 reflects a transition between coupling regimes. As expected, the study suggests a relatively better SAW transmission across the chip in the absence of mesa between the two IDTs. However, SAW transmission for a 10 μm mesa results in a similar value to those of the samples without mesa in between the two IDTs. One explanation is that the SAW travels underneath the mesa rather than on top of it. Although great care was taken to maintain uniformity during the fabrication, the changes in the transmission values could be attributed to the fact that it is difficult to fabricate IDT with small (~ 3.1 μm) fingers of even width using an optical lithography approach. In addition, the matching for the circuits was not optimised.

5.5 IDTs characterisation on GaAs sputtered with ZnO

Due to the fact that GaAs is a weak piezoelectric material, four SI-GaAs samples (each with two IDTs) were fabricated on thin layers of ZnO to act as a stronger piezoelectric material. In each sample, ~ 200 μm layer of ZnO was sputtered as described in Chapter 2.

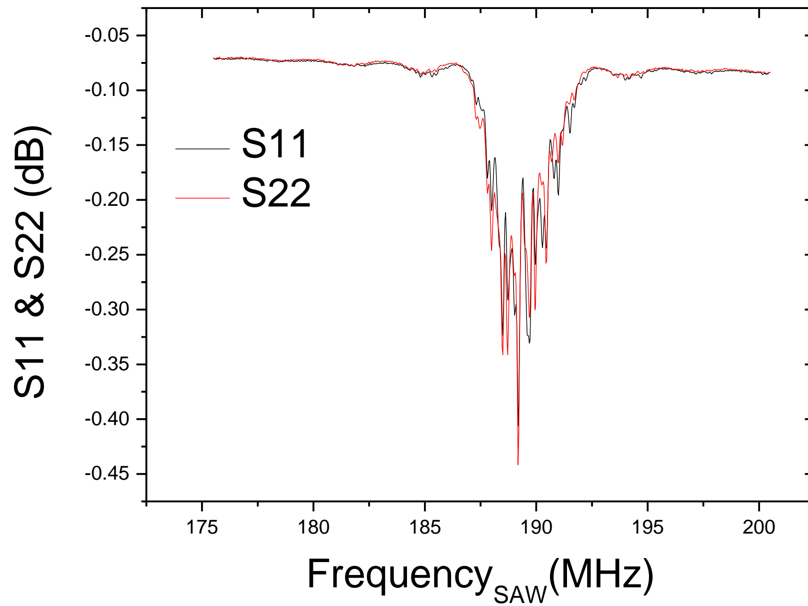

Figure 5-9: S11 and S22 parameters configurations measured by a network analyser of SAW generating at 187 MHz on 200 µm layer of ZnO.

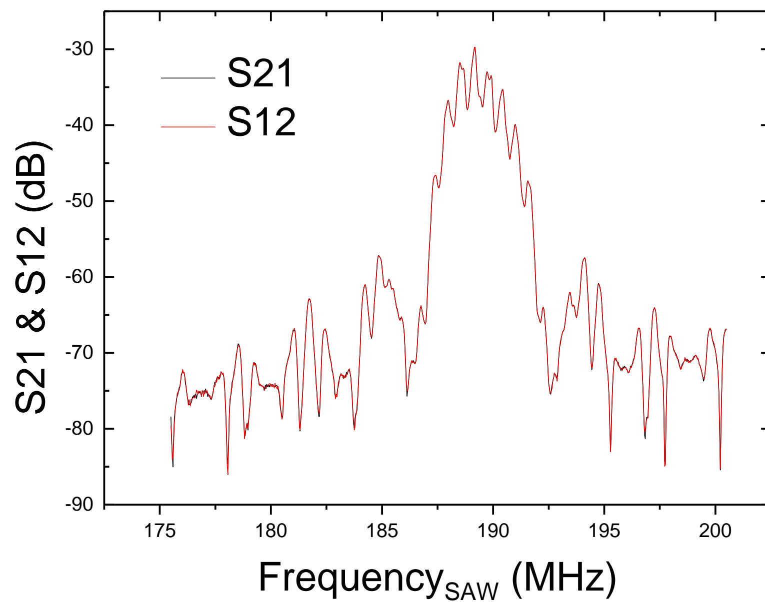

Figure 5-10: S12 and S21 parameters configurations measured by a network analyser of SAW generating at 187 MHz on 200 µm layer of ZnO.

As can be seen from the S-parameters values in Figure 5-9 and Figure 5-10 (~ -45 dB for S11 and S22, and ~ -30 dB for S21 and S12) no notable improvement can be seen due to the addition of ZnO thin layers. Thicker layer and higher quality sputtering may be needed in order to benefit from the ZnO piezoelectricity nature.

5.6 IDTs with THz QCLs

Four wafers were used to fabricate THz QCLs integrated with IDTs. These wafers were L500, L514, L645 and L654. All wafers were based on the RP depopulation active region design [34]. 3.1 THz lasers parameters are shown in Table 5-2. All the laser devices have the same dimensions of 1.6 mm in length, 200 μm in width and 10 μm in thickness active regions. Sloped angles facets of Φ ~42º were used for this work as this angle provides good lasing and also has improved SAW transmission properties [41]. After etch-removing the bottom n^+GaAs layer, IDTs were fabricated on both sides of the facet of the laser (see Figure 5-11), leaving a 0.5 mm gap between the IDT and the facet. All the fabrication steps for both the THz QCL and IDT were detailed in Chapter 2.

Device name	J_{th} (A/cm^2) ±2%	P_{max} (mW) ±10%	T_{max} (K) ±5%
L514-01	825	3	83
L645-01	775	4	72
L654-01	815	0.5	58

Table 5-2: Performance overview for exemplar THz QCLs devices integrated with IDTs.

Ideally, as shown in Figure 5-11, SAWs propagate from one IDT along the QCL ridge and are then received at the other IDT. However, it can be difficult to obtain lasing from the QCLs with both facets etched owing to increased loss. Thus, samples were also cleaved from one side of the laser only, leaving the other sloped facet un-cleaved (see Figure 5-12). This means that the sample will only have one IDT at the front of the sloped etched facet. In this case, it was not possible to measure S-parameters for both IDTs before cleaving the samples from one side. This is owing to the difficulties of dismounting the devices after testing them. Figure 5-13 shows S11 parameter measurements taken after removing the second IDT from a sample by cleaving one facet of the QCL. Lasing was then measured from the cleaved facet. The dimensions of the devices after cleaving were then 1.4 mm instead of 1.6 mm as the 0.2 mm was removed during cleaving.

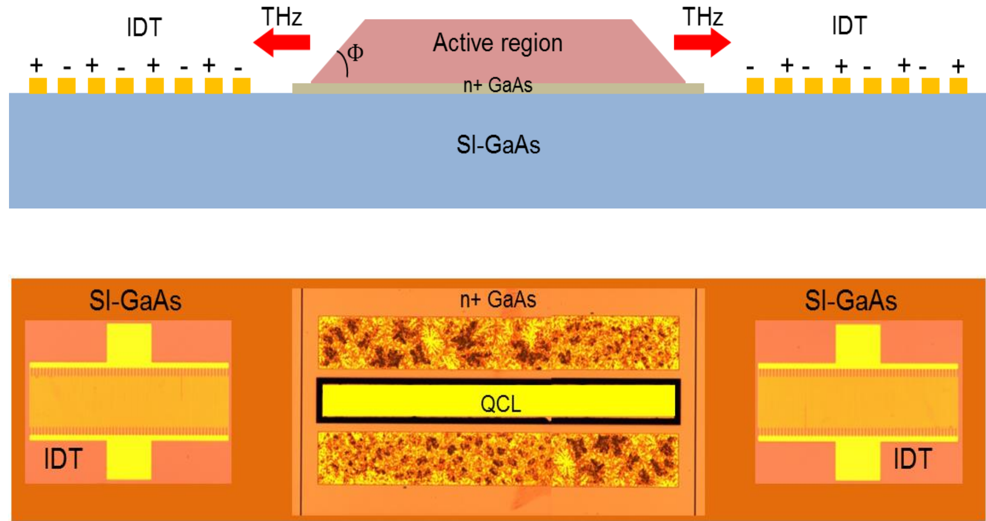

Figure 5-11: Two Schematic diagrams with top microscope images of a THz QCL monolithically integrated with two IDTs. Figure not to scale.

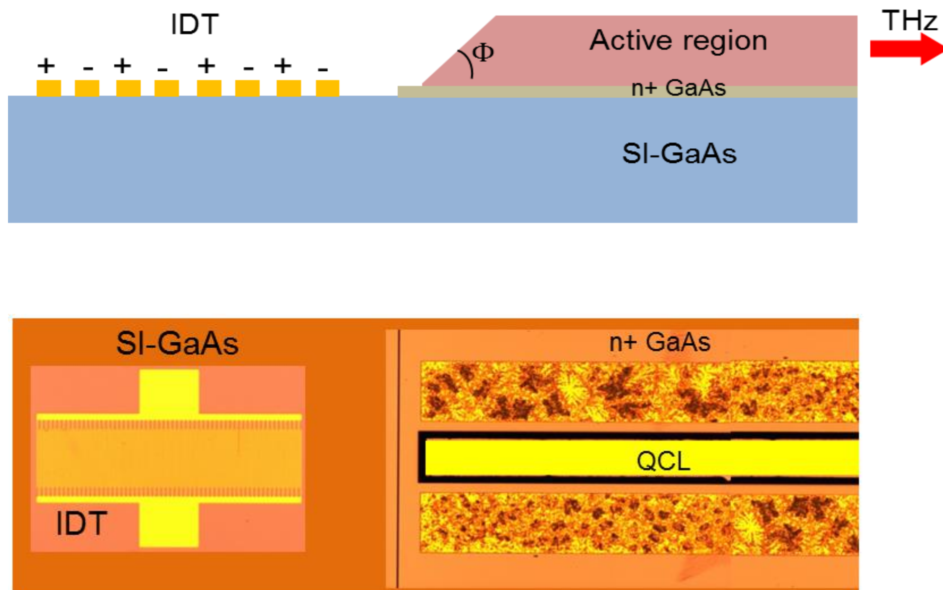

Figure 5-12: Two Schematic diagrams with top microscope images of a THz QCL (with one facet cleaved) monolithically integrated with only one IDT. Figure not to scale.

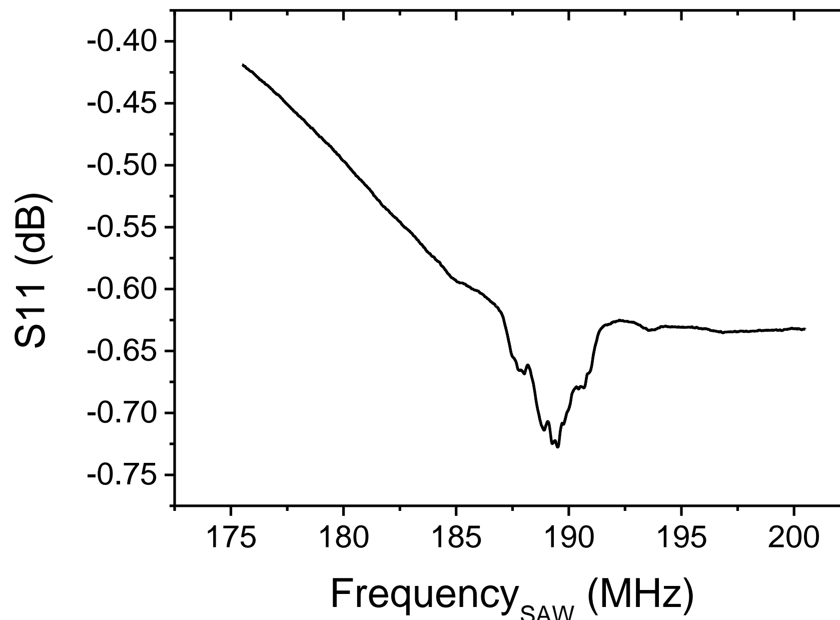

Figure 5-13: S11 parameter measured by a network analyser of a SAW generated at 187 MHz from a single IDT integrated with QCL, the other IDT was removed in order to have cleaved facet for the QCL emission.

In order to investigate the effect of SAWs on the behavior of THz QCLs, a lock-in technique was employed to perform the experiments. In these experiments, both electrical and spectral characteristics were monitored. First, the voltage-current density (V-J), light-current density (L-J) and spectral measurements were acquired for the QCLs with the IDTs being continually switched on for one set of experiments and off for another set of experiments. Then, the electrical and spectral results with the IDT switched on and off were compared. In this work, the IDTs were supplied with a continuous power level of 10 dBm using a network analyser. The samples were cryogenically cooled to 10 K. All QCLs were operated at a 2 % duty cycle.

Comparison of the results of sample L645-01 is displayed in Figure 5-15 and Figure 5-15. The current density behavior (in Figure 5-15) and output power behavior (in Figure 5-15) shows that SAWs with 187 MHz frequency have no detectable impact on the laser electrical performance. Also, as in Figure 5-16 and Figure 5-17, no noticeable change was seen in the spectral characteristics.

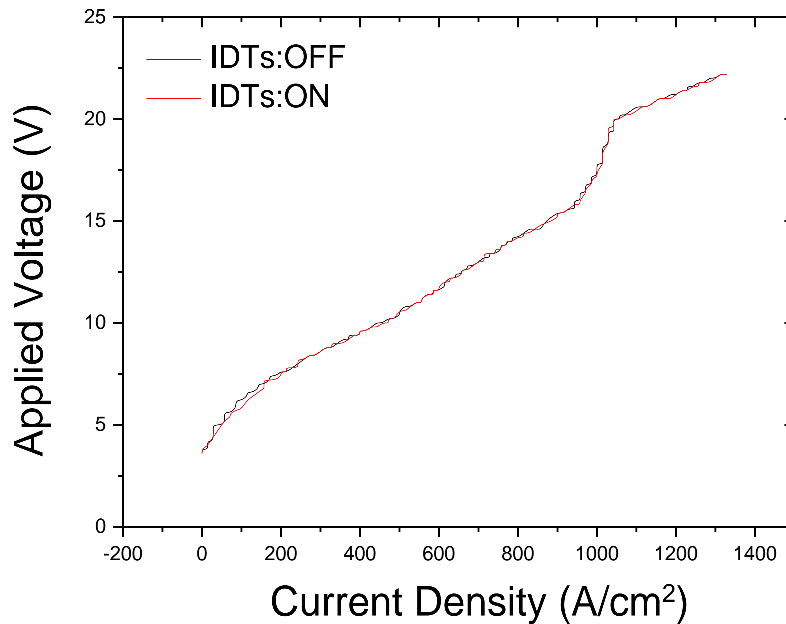

Figure 5-14: Comparison of V-J for sample L645-01 with the IDT being on (black), and off (red).

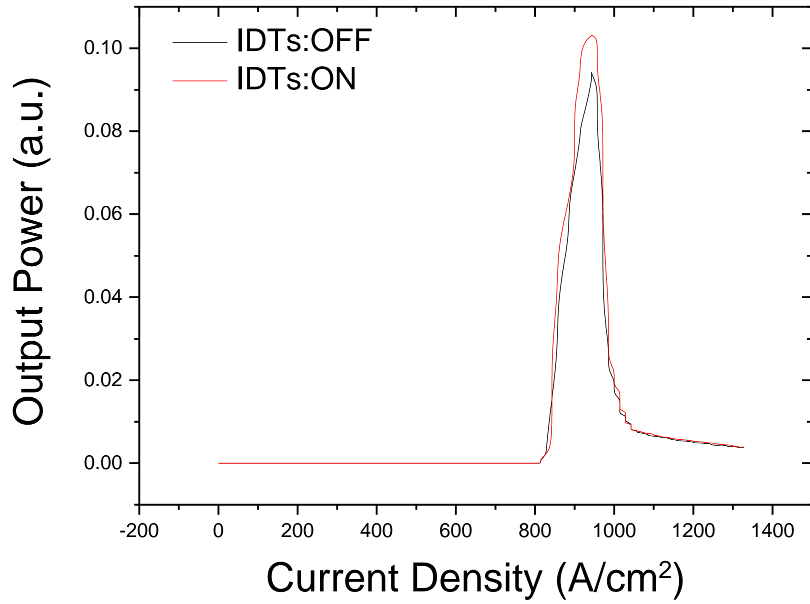

Figure 5-15: Comparison of L-J for sample L645-01 with the IDT being on (black), and off (red).

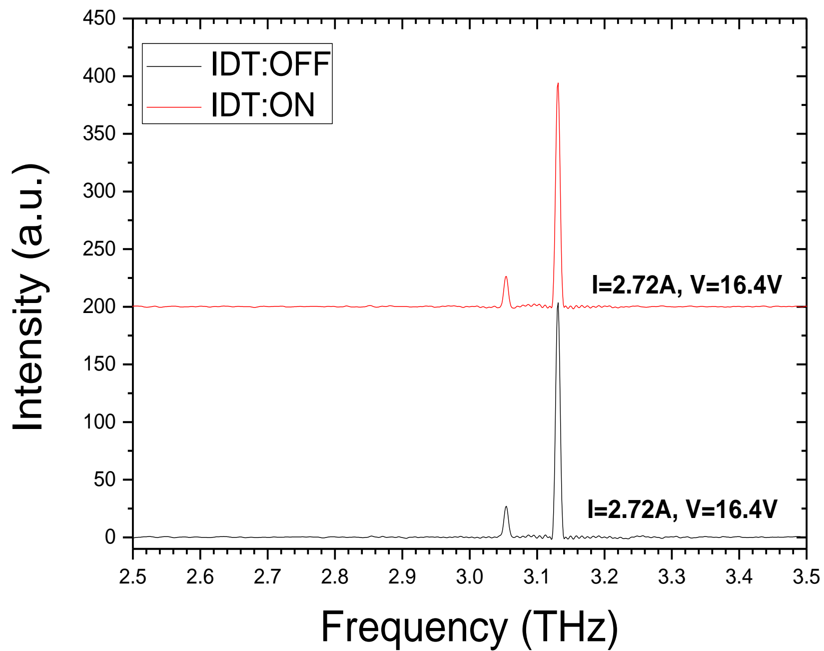

Figure 5-16: Comparison of frequency spectra for sample L645-01 with the IDT being on (black), and off (red). The QCL was drive with 16.4 V.

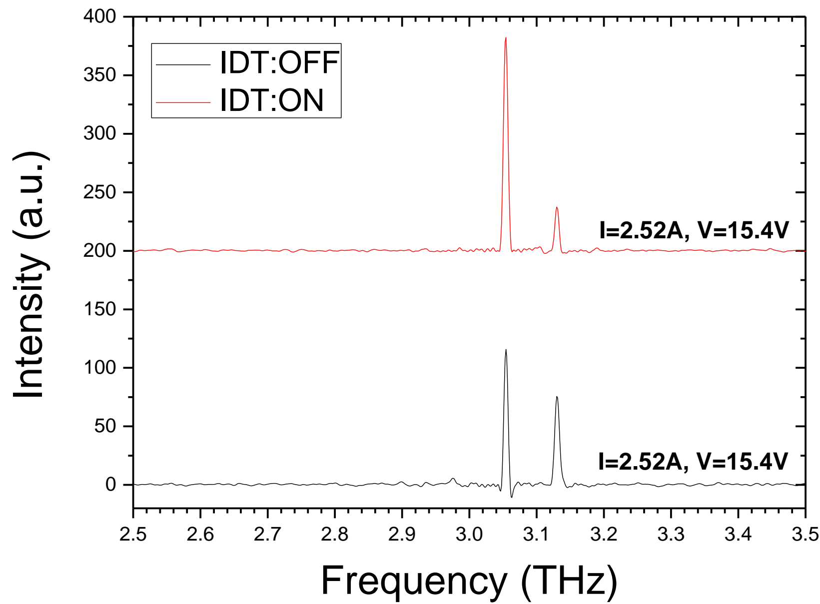

Figure 5-17: Comparison of frequency spectra for sample L645-01 with the IDT being on (black), and off (red). The QCL was drive with 15.4 V.

Similar sets of experiments, but while varying SAW frequency, were undertaken for sample L645-02. First, the electrical and spectral behaviour were taken when the IDTs were not in operation. Then, the same set of tests was run while the frequency of the operating SAW varied. In addition, to the designed frequency of the IDTs (~ 226 MHz), the IDTs were also run at ~ 206 and 246 MHz. Like the last device (L645-01) measurements, the continuous power sent to the IDTs through the network analyser was 10 dBm. The experiments were run at 10 K, and the 3.1 THz QCLs was run at a 2% duty cycle. These experiments were repeated twice. Neither current density (Figure 5-18), output power (Figure 5-19) or frequency spectra (Figure 5-20) changed noticeably

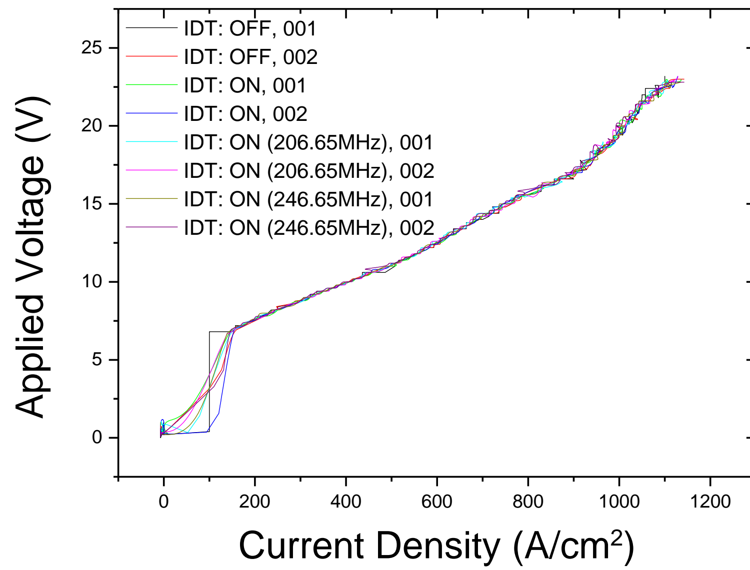

Figure 5-18: Comparison of V-J plot for the sample L645-02 with the IDT being off and on at different SAWs frequency. Each measurement was conducted twice (001 denote to the first measurement and 002 to the second measurement).

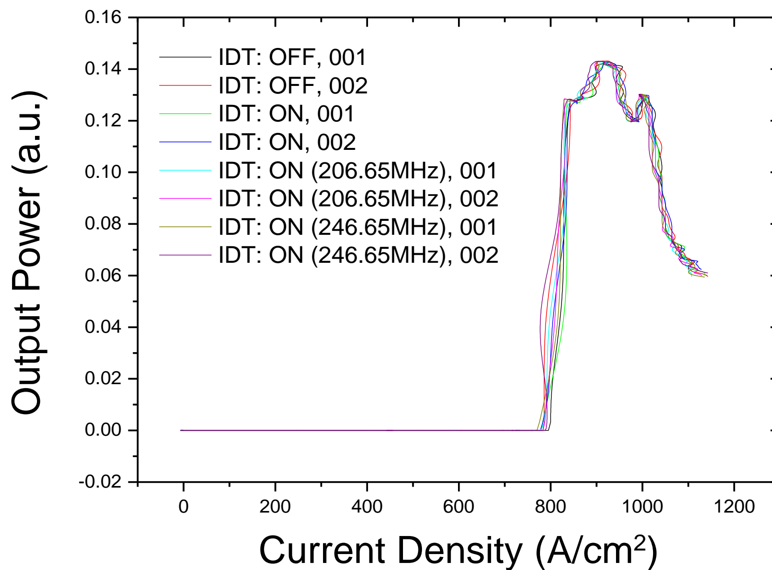

Figure 5-19: Comparison of L-J for the sample L645-02 with the IDT being off and on at different SAWs frequency. Each measurement was conducted twice (001 denote to the first measurement and 002 to the second measurement).

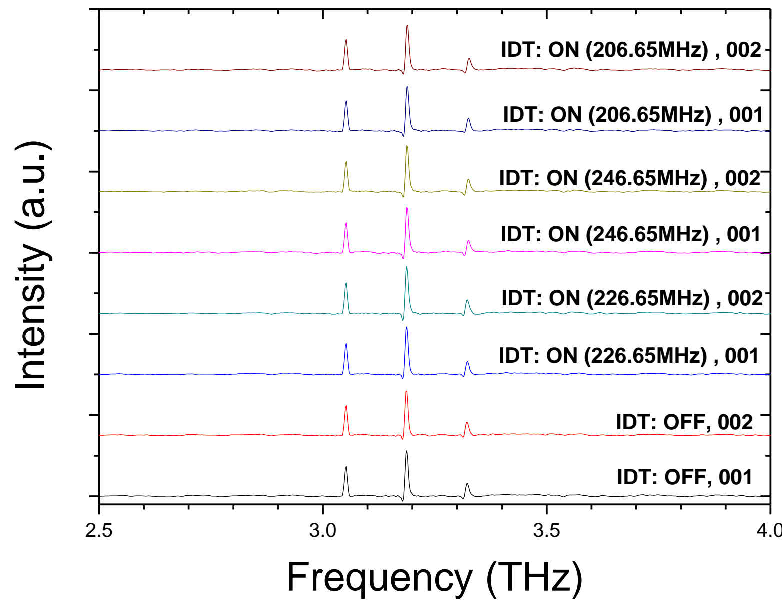

Figure 5-20: Comparison results of frequency spectra for the sample L645-02 with the IDT being off and on at different SAWs frequency. The QCL was run at I_{th} = 2.28 A. Each measurement was conducted twice (001 denote to the first measurement and 002 to the second measurement).

In addition to the above, a more sensitive modulation scheme (lock-in technique) was employed in order to investigate the relationship between the applied SAW and corresponding QCL performance. To achieve this, the network analyser which operates the IDT, was modulated with a pulse generator, which ran the QCLs. The IDT (design frequency ~ 226 MHz) was scanned over the range from 205 MHz to 245 MHz. This approach is expected to provide more accurate measurements as the recorded change in the output power of the laser collected by the bolometer will be solely due to SAWs. As shown in Figure 5-21, a change in the output power was clearly observed around the SAW frequency (~ 226 MHz) when running the QCL at the threshold current and slightly above. Unfortunately, the same

change in the output power was also measured when the laser was switch off, and below the threshold current. This means that the change in the output power was not due to the SAW interacting with QCL. The change can be attributed to background radiation been picked by the bolometer.

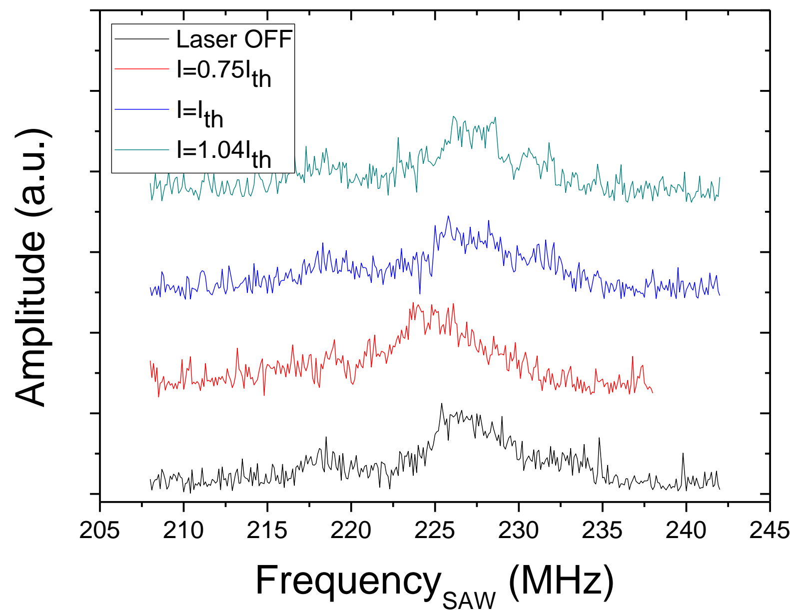

Figure 5-21: Change in output power of a THz QCL (L645-02) as the SAW frequency is changed between 205 MHz to 245 MHz. QCL was run at four different current in each measurements.

In summary, the attempts to obtain a system whereby the QCLs can be modulated when SAWs propagate across the active regions; were unfortunately unsuccessful. The possible reasons behind this failure can be attributed to number of aspects. First, as discussed in Section 5.2.1, the electromechanical coupling constant (K^2) for GaAs material is small. Second, SAWs propagating along GaAs suffer from high loss due to the inconsistencies in the width of the metallic fingers, and the gaps between them, of the IDTs. The uneven widths of the fingers and gaps occur

because of the difficulty of fabrication such small fingers (~ 3.1 μm) using optical lithography. This inexactness gives rise to SAWs reflection, hence increases loss, as the waves propagating from each pair of metallic fingers are not precisely in phase. Third, both QCL and IDT were processed to be 0.5 mm apart, which could minimize the coupling efficiency between the SAWs and QCLs. Another possible reason is that the SAWs are not interacting with the active region at all because they are reflected back from the edge of the etched-facet of the laser, or travel underneath the active region. In fact, if the last scenario was the case, this means that the n^+ GaAs under the active region will lead to even more loss for SAWs propagations. Alternative approaches to enable transmission of SAWs along the QCL and probing the SAWs will be proposed in Chapter 6.

With regards to the difficulty of fabricating the IDTs, it may be opportune to describe the challenge of fabricating such small fingers (~ 3.1 μm). These IDTs were fabricated by optical lithography and the space between the mask and the sample underneath it during processing was ~ 10 μm, which was the height of the QCL mesa. Giving that this was the case, a proximity alignment was implemented as an alternative to the ideal contact photolithography [40]. This, in turn, makes the lift-off of the pattered gold very difficult leading to uneven width of the fingers and gaps of the IDTs. Moreover, because the ridge of the QCL was defined prior to processing the IDTs, the dedicated area for IDTs was not fully flat due to the etching. This issue causes lift-off to be even harder due to the touching of adjacent fingers that can occur.

Nevertheless, in this chapter it has clearly been shown that devices can be fabricated incorporating etched laser facets and operational IDTs. Lasing is achieved and SAW propagation obtained. This proves an excellent starting point for SAW-modulated QCLs.

5.7 Conclusion

This chapter started by discussing the underpinning theory of integrating SAWs with THz QCLs. The fabrication and characterisation of IDTs on SI-GaAs were then described and two different frequencies of SAWs (~ 187 and ~ 224 MHz) were tested. A ~ 2 MHz shift in the frequency of the SAW was seen as the temperature was reduced from room temperature to 10 K. Next, the effect of mesa height on SAW propagation was evaluated. The influence of introducing a thin layer of a strong piezoelectric material (ZnO) on SAW performance was, then, presented. The ~ 200 µm layer of ZnO, unfortunately, showed no effect on SAW propagation. Thicker and/or higher quality layer of ZnO may be needed. Finally, attempts to modulate a THz QCL with SAWs were detailed. To achieve this goal, two IDTs were fabricated on both sides of the etched-facet THz QCL, and the propagation of a SAW across the piezoelectric GaAs crystal was monitored. Different means of observing the interaction between SAWs and QCLs were also investigated. In particular, a sensitive modulation scheme (lock-in technique) was employed to investigate the relation between SAWs and QCLs performance. However, no change in current density, output power or frequency spectra of THz

QCL were detected as SAWs were sent through the active region. This could be due to the weak piezoelectricity of the GaAs-based materials, the technique used to modulate the QCLs or the IDT geometry used. Furthermore, S-parameters (S11 and S22) proved that the loss of SAWs was very high leading to only small amount of acoustic energy being launched up and over the length of QCLs. Thus, attempt to improve S11 and S22 is crucial. In this regards, introducing matching circuits to the system may improve the performance. Recommendations for future work in this regards will be offered in Chapter 6.

Chapter 6

Conclusion and Future work

6.1 Conclusion

This work has presented three integral studies on the development of terahertz quantum cascade lasers (THz QCLs). The effect of thinning the QCL active region by etching was discussed. Then, THz sensing and imaging through self-mixing (SM) techniques in a THz QCL was demonstrated. Lastly, the utilisation of Surface acoustic waves (SAWs) in controlling the spectral behaviour of THz QCL sources was evaluated

Chapter 1 outlined an overview of THz radiation related and QCL related technology, and a summary of THz sources was given. This study has explained the central importance of THz radiation as an attractive solution for many potential applications. The intersubband transitions and the basic theory concepts of QCLs were then presented. Additionally, the difference between conventional semiconductor lasers and QCLs was defined. This chapter has also given a brief listing of the most common active region designs used in THz QCL. These designs are chirped superlattice (CSL), bound-to-continuum (BTC), resonant-phonon (RP) and

hybrid. The growth of THz QCLs using MBE was then presented in brief. To end with, an outline of the two common types of optical confinement for THz QCLs, single metal and double-metal waveguides was given.

Chapter 2 reported the many processes involved in the fabrication of single metal THz QCL. From forming the laser cavities by wet etching to backside metallization, it has been shown that the fabrication of a single metal waveguide is a non-trivial and multipart process. A brief overview of THz QCL cleaving, mounting on the copper block heat-sink, and wire-bonding steps were also shown. Processing guidelines for sloped angled facet, that would facilitate monolithic integration of QCLs into terahertz circuits, were also presented.

Additionally, a detailed description was presented for fabricating interdigitated transducers (IDTs) to generate surface acoustic waves (SAWs) for the purposes of realising devices that would feature tunable single mode THz QCL. Information was also provided about the zinc oxide (ZnO) sputtering in order to enhance QCL and SAWs coupling by introducing a high piezoelectric material layer.

The electrical and spectral characterisation procedures of THz QCL devices as well as SAW measurements, along with experimental apparatus used, has also been described.

The work in Chapter 3 was undertaken to experimentally investigate the influence of varying the active region etch depth and evaluate the QCL performance accordingly. In the present study, a number of samples were fabricated from different active region designs with etch thickness range of

different depth (10, 8.5, 7.5, 6.5, 5 and 4.2 μm). The devices were prepared through partial wet etching of the original 10 μm epilayer grown structure. In this investigation, the aim was to assess the effect of changing the etch depth on the current density, output power and QCL maximum operating temperature.

The results of this investigation show that regardless of the etch depth of the active region, the current density show no significant change over the range of samples suggesting that the current path is independent of the etch depth. However, except for L559 RP active region design with 7.5 μm etch depth, the radiation output power and the maximum operating heat-sink temperature exhibit degradation as the active region etch thickness reduced. The performance characteristics of THz QCLs with thin etched BTC structures have also been shown, demonstrating clearly the performance reduction experienced as the etch depth is increased. Taken together, these results suggest that this can be attributed to the additional losses in the unbiased structure below the bottom contact strip lines. Moreover, the left structure causes absorption and produces no gain. In addition, the poor optical mode confinement, as well as the difficult output coupling compared to the full structure, made the situation even worse, although these structures did offer better heat extraction. Therefore, the 7.5 μm devices work best for L559 and that may be due to having the highest operating bias and better heat extraction.

Chapter 4 has demonstrated THz sensing and imaging through SM interferometry in a QCL, in which a THz QCL is employed not only as the

radiation source but also as an interferometric detector. The SM laser sensing and imaging technique therefore allows a simple, self-aligned and robust system for measuring displacement and high-resolution imaging of visibly-concealed objects. Furthermore, the problem of the reliance of THz QCLs on slow, insensitive and incoherent thermal detectors, which has limited their practical use in THz systems, has been solved. Applications of this technique could include monitoring the motion of visibly concealed objects.

In this system, radiation is reflected from an object back into the QCL cavity, causing changes in the laser properties; depending on the amplitude and phase of the reflection. This allows simple, ‘detector-free’, sensing of displacement and reflectivity, with high-sensitivity owing to its coherent nature.

It has been shown that it is possible to determine the oscillation of a remote object using a “detector-less” sensor system in which the SM signal is monitored through the QCL drive voltage. This work has also verified that these measurements are equivalent to those obtained using a more conventional optical SM technique, thus allowing phase-sensitive THz SM sensing without any external detector.

Owing to the high SM sensitivity, further experiments have demonstrated that high-resolution THz SM imaging may be achieved over an extended distance of 10.5 m between the QCL and an object were no atmospheric purging was employed during the experiments.

Also, Surface-profiling through SM in a THz QCLs was demonstrated, in which, coherent three-dimensional (3D) imaging of a stepped GaAs structure fabricated by wet chemical etching was shown, in which the surface height was extracted from the phase of a set of SM voltage waveforms.

Chapter 5 reported the realisation of tunability of THz QCL induced by SAWs. The underpinning theory was also presented. This project was undertaken to study and evaluate the possible exploitation of SAWs in controlling the spectral behaviour of THz QCL sources.

Several samples of IDTs and bulk GaAs mesa of different heights (10, 8.5, 7.5, 6.5 and 5 μm) were demonstrated and characterised in order to investigate SAWs propagation over these different heights. The findings of this study suggested that mesa with $\Phi \sim 42^0$ sloped angle of 10 μm height would not allow efficient SAW propagation over the top of the device. An implication of this is the possibility that the SAW's power travels below the mesa and/or is reflected back. The added layer (~ 200 nm) of ZnO immediately below the IDTs was to benefit from its high piezoelectric feature compared to the weak piezoelectricity of GaAs. However, the IDTs measurements support the idea that thicker layer of ZnO may be needed.

A number of processed samples successfully demonstrated the SAWs propagation of two frequencies (~ 187 and ~ 224 MHz) over the THz QCL cavity. The results of S-parameters measurements of this study indicate that the interaction between SAWs and THz QCL is very weak on this design, revealing that no change in emission frequency, current density

or output power was observed. In general, therefore, it seems that the SAWs may travel underneath the QCL active region or even reflect back from the laser ridge. Another possible explanation for this is that the bottom n+ GaAs region could have increased loss during SAW propagation. Whilst this study did not confirm SAWs and QCL coupling, it did, however, make several noteworthy contributions towards understanding the nature and behaviour of QCL performance under influence from SAWs.

6.2 Future work

Knowledge of the nature of interactions between SAWs and etched facet THz QCL with thin etched active regions is of great importance to shape the future of functional material integration into novel, tunable elements and high THz power devices. The preliminary work of studying the thin etch active region along with integrating these devices with IDTs through fabricating etched facet QCL showed that a novel and compact tunable THz QCL device could be realised in this way, which could provide additional functionality or device minimisation for portable THz systems. It is hoped that further work can be implemented into the improvement of SAW coupling with QCLs by introducing matched circuits to the system and/or processing the IDTs on the top of the QCL cavity. THz QCLs and IDTs monolithically fabricated with thick layers (> 200 nm) of piezoelectric materials such as ZnO structures should be characterised in order to ascertain whether SAW coupling with QCL active regions can occur.

As the results in Chapter 3 suggested, The THz QCLs with 7.5 μm etch depth have a better performance over the standard (fully etched) 10 μm devices, therefore it is recommended to integrate IDTs with these shallow etched QCLs.

As the work in Chapter 4 shows, SM signal can be monitored through the QCL drive voltage, this verified that the voltage measurements are equivalent to those obtained using a more conventional optical SM technique, and that both methods are capable of determining the THz absorption coefficient of samples in the beam path. This method could readily be applied to the development of compact systems for a broad range of applications including high-resolution gas spectroscopy using a tunable QCL.

In the Long stand-off imaging system used in this work, only a 30% reduction was observed in the imaging quality (defined by the figure-of-merit K), compared with the short-range result. Thus, it is possible that the scanning distance could be extended more than 21 m in air. Furthermore, larger improvements in the imaging distance could be achieved by tuning the laser emission to match an atmospheric transmission window [55].

It is thought that the extension of this single-laser system to an array of QCLs will allow for material characterisation at a number of frequencies, and therefore material identification.

Since the SM scheme is sensitive the phase of the reflected field, the QCL in this work is operated in CW mode in order to achieve good spectral purity [78]. However, the QCL could, in principle, be operated in

pulsed mode, thus removing the need for the mechanical chopper implemented in this work. As the modulation speed of the SM signal is currently limited by the maximum usable mechanical chopper speed, removing this chopper would allow faster modulation.

In addition to the specific work presented in this thesis, there are a few other projects with which I have been associated with during my PhD research. These include:

1. Detection of terahertz frequency radiation via the photothermoelastic response of zincblende crystals. This project led to a paper in Journal of the Optical Society of America B. For this project, I fabricated the devices using wafers L173 and L647.
2. I contributed, by supplying and testing devices of single metal and double metal THz QCLs, to radiation exposure project in collaboration with: Atmospheric, Oceanic and Planetary Physics, Department of Physics, University of Oxford. These devices are from L170, L654 and L656.
3. I supplied devices from L243 to: (Laboratoire Pierre Aigrain and Institut d'Electronique Fondamentale–Paris-Sud) to study electrically-tunable THz QCLs.
4. Studying the effect of background doping on THz QCL performance. In this work I fabricated and characterised a number of devices from the wafers L645, L647, L674 and L676.
5. Studying the performance of the THz QCLs grown by misoriented wafers. Here, my role was the fabrication and characterisation for a number of devices from L690.
6. Comparing the performance of THz QCLs grown by As2 and As4 cells in the MBE system. For this work, I fabricated and tested a number of samples from L565.

7. Evaluating the effect of top n+ GaAs thickness on the THz QCLs performance. For this research I fabricated and measured devices from L674 and L676.
8. Frequency-domain techniques for measuring the magneto-conductivity of two-dimensional electron systems. For this research my role was supplying the THz QCL samples used from the wafers L173, L559 and L674.

List of References

[1] G. Davies and E. Linfield, "Bridging the terahertz gap," *Physics World,* vol. 17, pp. 37-41, 2004.

[2] A. G. Davies, E. H. Linfield, and M. B. Johnston, "The development of terahertz sources and their applications," *Physics in Medicine and Biology,* vol. 47, pp. 3679-3689, 2002.

[3] F. F. John, S. Brian, H. Feng, G. Dale, B. Robert, O. Filipe, and Z. David, "THz imaging and sensing for security applications—explosives, weapons and drugs," *Semiconductor Science and Technology,* vol. 20, p. S266, 2005.

[4] S. M. Kim, F. Hatami, J. S. Harris, A. W. Kurian, J. Ford, D. King, G. Scalari, M. Giovannini, N. Hoyler, J. Faist, and G. Harris, "Biomedical terahertz imaging with a quantum cascade laser," *Applied Physics Letters,* vol. 88, pp. 153903-153903-3, 2006.

[5] P. Dean, M. U. Shaukat, S. P. Khanna, S. Chakraborty, M. Lachab, A. Burnett, G. Davies, and E. H. Linfield, "Absorption-sensitive diffuse reflection imaging of concealed powders using a terahertz quantum cascade laser," *Optics Express,* vol. 16, pp. 5997-6007, 2008/04/28 2008.

[6] D. M. Mittleman, R. H. Jacobsen, and M. C. Nuss, "T-ray imaging," *Selected Topics in Quantum Electronics, IEEE Journal of,* vol. 2, pp. 679-692, 1996.

[7] M. Tonouchi, "Cutting-edge terahertz technology," *Nat Photon,* vol. 1, pp. 97-105, 2007.

[8] B. Ferguson and X.-C. Zhang, "Materials for terahertz science and technology," *Nature Materials,* vol. 1, pp. 26-33, 2002.

[9] K. L. Nguyen, M. L. Johns, L. Gladden, C. H. Worrall, P. Alexander, H. E. Beere, M. Pepper, D. A. Ritchie, J. Alton, S. Barbieri, and E. H. Linfield, "Three-dimensional imaging with a terahertz quantum cascade laser," *Opt. Express,* vol. 14, pp. 2123-2129, 2006.

[10] B. B. Hu and M. C. Nuss, "Imaging with terahertz waves," *Optics Letters,* vol. 20, pp. 1716-18, 1995.

[11] A. G. Davies, A. D. Burnett, F. Wenhui, E. H. Linfield, and J. E. Cunningham, "Terahertz spectroscopy of explosives and drugs," *Materials Today,* vol. 11, pp. 18-26, 2008.

[12] B. S. Williams, "Terahertz quantum-cascade lasers," *Nat Photon,* vol. 1, pp. 517-525, 2007.

[13] B. S. Williams, S. Kumar, Q. Hu, and J. L. Reno, "Operation of terahertz quantum-cascade lasers at 164 K in pulsed mode and at 117 K in continuous-wave mode," *Optics Express,* vol. 13, pp. 3331-3339, 2005.

[14] H.-W. Hübers, S. Pavlov, A. Semenov, R. Köhler, L. Mahler, A. Tredicucci, H. Beere, D. Ritchie, and E. Linfield, "Terahertz quantum cascade laser as local oscillator in a heterodyne receiver," *Opt. Express,* vol. 13, pp. 5890-5896, 2005.

[15] P. H. Siegel, "Terahertz technology," *IEEE Transactions on Microwave Theory and Techniques,* vol. 50, pp. 910-928, 2002.
[16] P. W. Gwyn, "Filling the THz gap-high power sources and applications," *Reports on Progress in Physics,* vol. 69, p. 301, 2006.
[17] E. R. Brown, K. A. McIntosh, K. B. Nichols, and C. L. Dennis, "Photomixing up to 3.8 THz in low• temperature• grown GaAs," *Applied Physics Letters,* vol. 66, pp. 285-287, 1995.
[18] J. Faist, F. Capasso, D. L. Sivco, C. Sirtori, A. L. Hutchinson, and A. Y. Cho, "Quantum cascade laser," *Science,* vol. 264, pp. 553-6, 1994.
[19] R. Kohler, A. Tredicucci, F. Beltram, H. E. Beere, E. H. Linfield, A. G. Davies, D. A. Ritchie, R. C. Iotti, and F. Rossi, "Terahertz semiconductor-heterostructure laser," *Nature,* vol. 417, pp. 156-9, 2002.
[20] S. P. Khanna, "The Growth, Fabrication and Measurement of Terahertz Quantum Cascade Lasers " PhD Thesis, School of Electronic and Electrical Engineering The University of Leeds Leeds, February 2008
[21] G. Bastard and J. A. Brum, "Electronic states in semiconductor heterostructures," *Quantum Electronics, IEEE Journal of,* vol. 22, pp. 1625-1644, 1986.
[22] L. Esaki and R. Tsu, "Superlattice and Negative Differential Conductivity in Semiconductors," *IBM Journal of Research and Development,* vol. 14, pp. 61-65, 1970.
[23] R. F. Kazarinov and R. A. Suris, "Possibility of the amplification of electromagnetic waves in a semiconductor with a superlattice," *Fizika i Tekhnika Poluprovodnikov,* vol. 5, pp. 797–800, April 1971.
[24] G. Scalari, C. Walther, M. Fischer, R. Terazzi, H. Beere, D. Ritchie, and J. Faist, "THz and sub-THz quantum cascade lasers," *Laser Photon. Rev,* vol. 3, pp. 45–66, 2009.
[25] C. Sirtori, J. Faist, F. Capasso, D. L. Sivco, A. L. Hutchinson, and A. Y. Cho, "Mid-infrared (8.5 um) semiconductor lasers operating at room temperature," *Photonics Technology Letters, IEEE,* vol. 9, pp. 294-296, 1997.
[26] C. Gmachl, F. Capasso, D. L. Sivco, and A. Y. Cho, "Recent progress in quantum cascade lasers and applications," *Reports on Progress in Physics,* vol. 64, pp. 1533-601, 2001.
[27] C. A. Evans, "The optical and thermal properties of quantum cascade lasers," PhD Thesis, School of Electronic & Electrical Engineering, The University of Leeds, Leeds, 2008.
[28] N. M. Hinchcliffe, "Fabrication and measurement of double metal terahertz quantum cascade lasers," PhD Thesis, School of Electronic and Electrical Engineering, The University of Leeds, Leeds, 2009.
[29] C. Sirtori, P. Kruck, S. Barbieri, P. Collot, J. Nagle, M. Beck, J. Faist, and U. Oesterle, "GaAs/$Al_xGa_{1-x}As$ quantum cascade lasers," *Applied Physics Letters,* vol. 73, pp. 3486-3488, 1998.
[30] A. Tredicucci, F. Capasso, C. Gmachl, D. L. Sivco, A. L. Hutchinson, and A. Y. Cho, "High performance interminiband quantum cascade

lasers with graded superlattices," *Applied Physics Letters,* vol. 73, pp. 2101-2103, 1998.
[31] M. Rochat, L. Ajili, H. Willenberg, J. Faist, H. Beere, G. Davies, E. Linfield, and D. Ritchie, "Low-threshold terahertz quantum-cascade lasers," *Applied Physics Letters,* vol. 81, pp. 1381-1381, 2002.
[32] J. Faist, M. Beck, T. Aellen, and E. Gini, "Quantum-cascade lasers based on a bound-to-continuum transition," *Applied Physics Letters,* vol. 78, pp. 147-149, 2001.
[33] S. Barbieri, J. Alton, H. E. Beere, J. Fowler, E. H. Linfield, and D. A. Ritchie, "2.9 THz quantum cascade lasers operating up to 70 K in continuous wave," *Applied Physics Letters,* vol. 85, pp. 1674-1676, 2004.
[34] B. S. Williams, H. Callebaut, S. Kumar, Q. Hu, and J. L. Reno, "3.4-THz quantum cascade laser based on longitudinal-optical-phonon scattering for depopulation," *Applied Physics Letters,* vol. 82, pp. 1015-1017, 2003.
[35] A. Tredicucci, R. Kohler, F. Beltram, H. E. Beere, E. H. Linfield, A. G. Davies, and D. A. Ritchie, "Terahertz quantum cascade lasers," Nara, Japan, 2004, pp. 846-851.
[36] R. Colombelli, F. Capasso, C. Gmachl, A. L. Hutchinson, D. L. Sivco, A. Tredicucci, M. C. Wanke, A. M. Sergent, and A. Y. Cho, "Far-infrared surface-plasmon quantum-cascade lasers at 21.5 um and 24 um wavelengths," *Applied Physics Letters,* vol. 78, pp. 2620-2622, 2001.
[37] S. Kohen, B. S. Williams, and H. Qing, "Electromagnetic modeling of terahertz quantum cascade laser waveguides and resonators," *Journal of Applied Physics,* vol. 97, pp. 53106-1, 2005.
[38] B. S. Williams, S. Kumar, H. Callebaut, Q. Hu, and J. L. Reno, "Terahertz quantum-cascade laser at 100 m using metal waveguide for mode confinement," *Applied Physics Letters,* vol. 83, pp. 2124-2126, 2003.
[39] K. Unterrainer, R. Colombelli, C. Gmachl, F. Capasso, H. Y. Hwang, D. L. Sivco, A. Y. Cho, and S. A. Michael, "Quantum cascade lasers with double metal-semiconductor waveguide resonators," *Applied Physics Letters,* vol. 80, pp. 3060-3060, 2002.
[40] R. Williams, *Modern GaAs Processing Methods*: Artech House, 1990.
[41] M. Salih, "Development of terahertz frequency quantum cascade lasers," PhD Thesis, Institute of Microwave and Photonics, The University of Leeds, Leeds, 2010.
[42] M. V. Kisin and S. Luryi, "Piezoacoustic modulation of gain and distributed feedback for quantum cascade lasers with widely tunable emission wavelength," *Applied Physics Letters,* vol. 82, pp. 847-849, 2003.
[43] P. Dean, A. H. Awang, I. Kundu, R. Alhathlool, S. P. Khanna, L. H. Li, A. Burnett, E. H. Linfield, and A. Giles Davies, "Detection of terahertz frequency radiation via the photothermoelastic response of zincblende crystals," *Journal of the Optical Society of America B,* vol. 30, pp. 3151-3160, 2013/12/01 2013.

[44] S. Kumar, "Recent Progress in Terahertz Quantum Cascade Lasers," *Selected Topics in Quantum Electronics, IEEE Journal of,* vol. 17, pp. 38-47, 2011.

[45] Q. J. Wang, C. Pflugl, W. F. Andress, D. Ham, F. Capasso, and M. Yamanishi, "Gigahertz surface acoustic wave generation on ZnO thin films deposited by radio frequency magnetron sputtering on III-V semiconductor substrates," *Journal of Vacuum Science & Technology B: Microelectronics and Nanometer Structures,* vol. 26, pp. 1848-1851, 2008.

[46] Y. Chassagneux, J. Palomo, R. Colombelli, S. Barbieri, S. Dhillon, C. Sirtori, H. Beere, J. Alton, and D. Ritchie, "Low threshold THz QC lasers with thin core regions," *Electronics Letters,* vol. 43, pp. 41-42, 2007.

[47] M. Salih, P. Dean, A. Valavanis, S. P. Khanna, L. H. Li, J. E. Cunningham, A. G. Davies, and E. H. Linfield, "Terahertz quantum cascade lasers with thin resonant-phonon depopulation active regions and surface-plasmon waveguides," *Journal of Applied Physics,* vol. 113, pp. 113110-5, 2013.

[48] E. Strupiechonski, D. Grassani, D. Fowler, F. H. Julien, S. P. Khanna, L. Li, E. H. Linfield, A. G. Davies, A. B. Krysa, and R. Colombelli, "Vertical subwavelength mode confinement in terahertz and mid-infrared quantum cascade lasers," *Applied Physics Letters,* vol. 98, 2011.

[49] S. Kumar, B. S. Williams, Q. Hu, and J. L. Reno, "1.9 THz quantum-cascade lasers with one-well injector," *Applied Physics Letters,* vol. 88, p. 121123, 2006.

[50] M. A. Belkin, J. A. Fan, S. Hormoz, F. Capasso, S. P. Khanna, M. Lachab, A. G. Davies, and E. H. Linfield, "Terahertz quantum cascade lasers with copper metal-metal waveguides operating up to 178 K," *Optics Express,* vol. 16, pp. 3242-3248, 2008.

[51] H. Luo, S. R. Laframboise, Z. R. Wasilewski, G. C. Aers, H. C. Liu, and J. C. Cao, "Terahertz quantum-cascade lasers based on a three-well active module," *Applied Physics Letters,* vol. 90, p. 041112, 2007.

[52] P. H. Siegel, "THz Instruments for Space," *Antennas and Propagation, IEEE Transactions on,* vol. 55, pp. 2957-2965, 2007.

[53] A. Valavanis, P. Dean, L. Yah Leng, R. Alhathlool, M. Nikolic, R. Kliese, S. P. Khanna, D. Indjin, S. J. Wilson, A. D. Rakic, E. H. Linfield, and G. Davies, "Self-Mixing Interferometry With Terahertz Quantum Cascade Lasers," *Sensors Journal, IEEE,* vol. 13, pp. 37-43, 2013.

[54] P. Dean, N. K. Saat, S. P. Khanna, M. Salih, A. Burnett, J. Cunningham, E. H. Linfield, and A. G. Davies, "Dual-frequency imaging using an electrically tunable terahertz quantum cascade laser," Busan, Korea, Republic of, 2009, pp. National IT Industry Promotion Agency; Korea Tourism Organization; BUSAN Convention and Visitors Bureau; Ajou University; Seoul Natl. Univ., BK21 Frontier Physics Research Division.

[55] A. W. M. Lee, Q. Qi, S. Kumar, B. S. Williams, Q. Hu, and J. L. Reno, "Real-time terahertz imaging over a standoff distance 25 meters," *Applied Physics Letters,* vol. 89, pp. 141125-141125-3, 2006.

[56] R. Lang and K. Kobayashi, "External optical feedback effects on semiconductor injection laser properties," *Quantum Electronics, IEEE Journal of,* vol. 16, pp. 347-355, 1980.

[57] Y. L. Lim, P. Dean, M. Nikolic, R. Kliese, S. P. Khanna, M. Lachab, A. Valavanis, D. Indjin, Z. Ikonic, P. Harrison, E. H. Linfield, A. G. Davies, S. J. Wilson, and A. D. Rakic, "Demonstration of a self-mixing displacement sensor based on terahertz quantum cascade lasers," *Applied Physics Letters,* vol. 99, pp. 081108-3, 2011.

[58] P. Dean, Y. Leng Lim, A. Valavanis, R. Kliese, M. Nikoli, S. P. Khanna, M. Lachab, D. Indjin, Z. Ikoni, P. Harrison, A. D. Raki, E. H. Linfield, and A. G. Davies, "Terahertz imaging through self-mixing in a quantum cascade laser," *Opt. Lett.,* vol. 36, pp. 2587-2589, 2011.

[59] G. Guido, N. Michele, D. Silvano, and B. Thierry, "Laser diode self-mixing technique for sensing applications," *Journal of Optics A: Pure and Applied Optics,* vol. 4, p. S283, 2002.

[60] Y. L. Lim, R. Kliese, K. Bertling, K. Tanimizu, P. A. Jacobs, and A. D. Rakic, "Self-mixing flow sensor using a monolithic VCSEL array with parallelreadout," *Optics Express,* vol. 18, pp. 11720-11727, 2010/05/24 2010.

[61] S. Donati, *Photodetectors*: Prentice Hall, 1999.

[62] D. Indjin, P. Harrison, R. W. Kelsall, and Z. Ikonic, "Mechanisms of temperature performance degradation in terahertz quantum-cascade lasers," *Applied Physics Letters,* vol. 82, pp. 1347-1349, 2003.

[63] R. P. Green, J.-H. Xu, L. Mahler, A. Tredicucci, F. Beltram, G. Giuliani, H. E. Beere, and D. A. Ritchie, "Linewidth enhancement factor of terahertz quantum cascade lasers," *Applied Physics Letters,* vol. 92, pp. 071106-3, 2008.

[64] S. Donati, *Electro-Optical Instrumentation, Sensing and Measuring with Lasers*. Upper Saddle River, New Jersey: Prentice-Hall, 2004.

[65] K. Petermann, *Laser Diode Modulation and Noise*. Dordrecht, Holland: Kluwer Academic Publishers, 1988.

[66] J. Hast, "Self-Mixing Interferometry And Its Applications In Noninvasive Pulse Detection," Department of Electrical and Information Engineering, University of Oulu, Oulu, Finland, February 2003.

[67] M. H. Koelink, M. Slot, F. F. M. de Mul, J. Greve, R. Graaff, A. C. M. Dassel, and J. G. Aarnoudse, "Laser Doppler Velocimeter Based On The Self-Mixing Effect In A Fiber-Coupled Semiconductor Laser: Theory," *Applied Optics,* vol. 31, pp. 3401-3408, 1992/06/20 1992.

[68] J. R. Tucker, "A Self-Mixing Imaging System Based on an Array of Vertical-Cavity Surface-Emitting Lasers," PhD Thesis, School of Information Technology and Electrical Engineering, The University of Queensland, 2007.

[69] P. K. Shrestha, "Self-Mixing Diode Laser Interferometry " Master of Engineering Thesis, University of Waikato, Hamilton, New Zealand, Feburary 2010.

[70] Y. Yanguang, G. Giuliani, and S. Donati, "Measurement of the linewidth enhancement factor of semiconductor lasers based on the optical feedback self-mixing effect," *Photonics Technology Letters, IEEE,* vol. 16, pp. 990-992, 2004.

[71] C. H. Henry, "Theory of the linewidth of semiconductor lasers," *Quantum Electronics, IEEE Journal of,* vol. 18, pp. 259-264, 1982.

[72] S. Melnik, G. Huyet, and A. Uskov, "The linewidth enhancement factor a of quantum dot semiconductor lasers," *Optics Express,* vol. 14, pp. 2950-2955, 2006/04/03 2006.

[73] G. P. Agrawal and C. M. Bowden, "Concept of linewidth enhancement factor in semiconductor lasers: its usefulness and limitations," *Photonics Technology Letters, IEEE,* vol. 5, pp. 640-642, 1993.

[74] J. von Staden, T. Gensty, W. Elsäßer, G. Giuliani, and C. Mann, "Measurements of the ? factor of a distributed-feedback quantum cascade laser by an optical feedback self-mixing technique," *Optics Letters,* vol. 31, pp. 2574-2576, 2006/09/01 2006.

[75] G. A. Acket, D. Lenstra, A. Den Boef, and B. Verbeek, "The influence of feedback intensity on longitudinal mode properties and optical noise in index-guided semiconductor lasers," *Quantum Electronics, IEEE Journal of,* vol. 20, pp. 1163-1169, 1984.

[76] W. M. Wang, W. J. O. Boyle, K. T. V. Grattan, and A. W. Palmer, "Self-mixing interference in a diode laser: experimental observations and theoretical analysis," *Applied Optics,* vol. 32, pp. 1551-1558, 1993/03/20 1993.

[77] W. M. Wang, K. T. V. Grattan, A. W. Palmer, and W. J. O. Boyle, "Self-mixing interference inside a single-mode diode laser for optical sensing applications," *Lightwave Technology, Journal of,* vol. 12, pp. 1577-1587, 1994.

[78] J. R. Tucker, A. D. Raki, C. J. O'Brien, and A. V. Zvyagin, "Effect of multiple transverse modes in self-mixing sensors based on vertical-cavity surface-emitting lasers," *Applied Optics,* vol. 46, pp. 611-619, 2007/02/01 2007.

[79] S. Donati, "Responsivity and Noise of Self-Mixing Photodetection Schemes," *Quantum Electronics, IEEE Journal of,* vol. 47, pp. 1428-1433, 2011.

[80] P. Dean, A. Valavanis, J. Keeley, K. Bertling, Y. Leng Lim, R. Alhathlool, S. Chowdhury, T. Taimre, L. H. Li, D. Indjin, S. J. Wilson, A. D. Rakić, E. H. Linfield, and A. Giles Davies, "Coherent three-dimensional terahertz imaging through self-mixing in a quantum cascade laser," *Applied Physics Letters,* vol. 103, 2013.

[81] M. S. Vitiello and A. Tredicucci, "Tunable Emission in THz Quantum Cascade Lasers," *Terahertz Science and Technology, IEEE Transactions on,* vol. 1, pp. 76-84, 2011.

[82] A. W. M. Lee, B. S. Williams, S. Kumar, Q. Hu, and J. L. Reno, "Tunable terahertz quantum cascade lasers with external gratings," *Opt. Lett.,* vol. 35, pp. 910-912, 2010.

[83] S. P. Khanna, M. Salih, P. Dean, A. G. Davies, and E. H. Linfield, "Electrically tunable terahertz quantum-cascade laser with a heterogeneous active region," *Applied Physics Letters,* vol. 95, 2009.

[84] J. Xu, J. M. Hensley, D. B. Fenner, R. P. Green, L. Mahler, A. Tredicucci, M. G. Allen, F. Beltram, H. E. Beere, and D. A. Ritchie, "Tunable terahertz quantum cascade lasers with an external cavity," *Applied Physics Letters,* vol. 91, pp. -, 2007.

[85] L. Rayleigh, "On Waves Propagated along the Plane Surface of an Elastic Solid," *Proceedings of the London Mathematical Society,* vol. s1-17, pp. 4-11, November 1, 1885 1885.

[86] C. K. Campbell, *Surface Acoustic Wave Devices for Mobile and Wireless Communications*: Academic Press, 1998.

[87] D. P. Morgan, *Surface-Wave Device for Signal Processing*. Amsterdam: Elsevier Science Publisher B. V., 1991.

[88] R. L. Miller, C. S. Nothnick, and D. S. Bailey, *Acoustic Charge Transport: Devices Technology and Application*. Bosten-London: Artech House, 1992.

[89] M. Feldmann and J. Hénaff, *Surface Acoustic Wave for Signal Processing*. Beston-London: Artech House, 1989.

[90] G. Valletta, "*Laser a cascataquanticamodulati da ondeacustiche di superficie*," MSc thesis, University of Pisa, Italy, 2008.

[91] S. Datta, *Surface Acoustic Wave Devices*: Prentice-Hall, 1986.

[92] J. M. Shilton, D. R. Mace, V. I. Talyanskii, G. Yu, M. Y. Simmons, M. Pepper, and D. A. Ritchie, "On the acoustoelectric current in a one-dimensional channel," *Journal of Physics: Condensed Matter,* vol. 8, p. L337, 1996.

[93] J. M. Shilton, V. I. Talyanskii, M. Pepper, D. A. Ritchie, J. E. F. Frost, C. J. B. Ford, C. G. Smith, and G. A. C. Jones, "High-frequency single-electron transport in a quasi-one-dimensional GaAs channel induced by surface acoustic waves," *Journal of Physics: Condensed Matter,* vol. 8, p. L531, 1996.

[94] J. Cunningham, V. I. Talyanskii, J. M. Shilton, M. Pepper, M. Y. Simmons, and D. A. Ritchie, "Single-electron acoustic charge transport by two counterpropagating surface acoustic wave beams," *Physical Review B,* vol. 60, pp. 4850-4855, 1999.

[95] J. Cunningham, V. I. Talyanskii, J. M. Shilton, M. Pepper, A. Kristensen, and P. E. Lindelof, "Single-electron acoustic charge transport on shallow-etched channels in a perpendicular magnetic field," *Physical Review B,* vol. 62, pp. 1564-1567, 2000.

[96] J. Cunningham, M. Pepper, V. I. Talyanskii, and D. A. Ritchie, "Acoustoelectric current in submicron-separated quantum wires," *Applied Physics Letters,* vol. 86, pp. 152105 - 152108, 2005.

[97] H. Kogelnik and C. V. Shank, "Coupled-Wave Theory of Distributed Feedback Lasers," *Journal of Applied Physics,* vol. 43, pp. 2327-2335, 1972.

[98] J. H. Ibry and W. D. Hunt, "Calculation of Delta n^2 and kappa for an acoustically induced distributed Bragg reflector (ADBR)," *Quantum Electronics, IEEE Journal of,* vol. 34, pp. 213-224, 1998.

[99] J. Faist, C. Gmachl, F. Capasso, C. Sirtori, D. L. Sivco, J. N. Baillargeon, and A. Y. Cho, "Distributed feedback quantum cascade lasers," *Applied Physics Letters,* vol. 70, pp. 2670-2672, 1997.

[100] S. Chakraborty, T. Chakraborty, S. P. Khanna, E. H. Linfield, A. G. Davies, J. Fowler, C. H. Worrall, H. E. Beere, and D. A. Ritchie, "Spectral engineering of terahertz quantum cascade lasers using focused ion beam etched photonic lattices," *Electronics Letters,* vol. 42, pp. 404-405, 2006.

List of Abbreviations

2D	two-dimensional
2DEG	two-dimensional electron gas
3D	three-dimensional
ADFB	acoustic induced distributed feedback
AlGaAs	Aluminum Gallium Arsenide
AR	active region
Au	Gold
BTC	bound-to-continuum
CSL	chirped superlattice
CW	continuous wave
DFB	distributed feedback
DI	deionised
DM	double-metal waveguide
FEL	free electron laser
FIB	focused ion beam
FTIR	fourier-transform-infra-red
FWHM	full width at half maximum
GHz	Giga Hertz
IDT	Interdigitated transducers
In	Indium
IPA	isopropyl alcohol
I-V	current-voltage
L-I	power–current
$LiNbO_3$	Lithium Niobate

L-J	Power-current density
LO	longitudinal optical
MBE	molecular beam epitaxy
MHz	Mega Hertz
MIR	Mid Infra-Red
MQW	multi quantum well
NDR	Negative differential resistance
PCB	Printed circuit board
PE	Polyethene
PID	Proportional-integral-differential
PNC	phonon induced non-lasing channel
PTFE	polytetrafluoroethylene
QCL	quantum cascade laser
RP	resonant-phonon
RTA	rapid thermal annealer
SAW	surface acoustic waves
SEM	scanning electron micrograph
SI-GaAs	semi-insulating GaAs
SiO_2	Silicon dioxide
SISP	semi insulating surface plasmon waveguide
SM	self-Mixing
S-parameters	Scattering parameters
THz	Tera Hertz
Ti	titanium
UV	Ultraviolet
V-J	Voltage-Current Density
ZnO	Zinc oxide

Appendix A The growth structure

Table below details the growth data for the different active regions used in this thesis. $Al_{0.15}Ga_{0.85}As$ barriers are highlighted in bold and the uniformly doped GaAs layer is underlined. Before the growth of the periods, an injector grading of one collector barrier and injection well was grown (the last two values in the growth sequence). Immediately after the growth of the periods, an injector barrier was grown (the first value in the growth sequence).

Wafer no.	Freq. (THz)	GaAs/Al0.15Ga0.85As layer sequence and thicknesses (Å)	Si doping levels (cm^{-3})	Active region thickness (μm)	Periods
L281	4.0	**47**/99/**15**/73/**40**/55/54/55	5×10^{16}	10	226
L500	3.0	**48**/96/**20**/74/**42**/53/55/53	6.8×10^{16}	10	226
L514	3.0	**48**/96/**20**/74/**42**/53/55/53	5×10^{16}	10	226
L559	3.0	**48**/96/**20**/74/**42**/53/55/53	5×10^{16}	10	226
L645	3.0	**48**/96/**20**/74/**42**/53/55/53	5×10^{16}	10	226
L647	2.6	1.8/12.8/1.5/15.5/0.6/ 9.0/0.6/14.0/3.8/11.6/ 3.5/11.3/2.7/**11.4** /2.0/**12.0**/2.0/12.2	2.4×10^{16}	11.5	90
L654	3.0	**48**/96/**20**/74/**42**/53/55/53	5×10^{16}	10	226